CUKUROVA UNIVERSITY
INSTITUTE OF NATURAL AND APPLIED SCIENCES

PhD THESIS

Derya FARİSOĞULLARI

PRODUCTION AND CHARACTERIZATION OF FeSe-11 SUPERCONDUCTOR CRYSTALS AND WIRES

DEPARTMENT OF PHYSICS

ADANA-2019

CUKUROVA UNIVERSITY
INSTITUTE OF NATURAL AND APPLIED SCIENCES

PRODUCTION AND CHARACTERIZATION OF FeSe-11 SUPERCONDUCTOR CRYSTALS AND WIRES

Derya FARİSOĞULLARI

PhD THESIS

DEPARTMENT OF PHYSICS

We certify that the thesis titled above was reviewed and approved for the award of degree of the Doctor of Philosophy by the board of jury on 30/01/2019.

.....	.....	.....
Doç.Dr. Ahmet EKİCİBİL	Prof.Dr. Faruk KARADAĞ	Prof.Dr. Metin ÖZDEMİR
SUPERVISOR	Co. SUPERVISOR	MEMBER
.....	.....	.....
Asst.Prof.Dr. Ali Osman AYAŞ	Asst.Prof.Dr. Mustafa AKYOL	Asst.Prof.Dr. Doğan KAYA
MEMBER	MEMBER	MEMBER

This PhD Thesis is performed in Department of Physics of Institute of Natural and Applied Sciences of Çukurova University.
Registration Number:

Prof. Dr. Mustafa GÖK
Director
Institute of Basic and Applied Sciences

ABSTRACT

PhD THESIS

PRODUCTION AND CHARACTERIZATION OF FeSe-11 SUPERCONDUCTOR CRYSTALS AND WIRES

Derya FARİSOĞULLARI

CUKUROVA UNIVERSITY
INSTITUTE OF NATURAL AND APPLIED SCIENCES
DEPARTMENT OF PHYSICS

Supervisor : Assoc. Prof. Dr. Ahmet EKİCİBİL
Co. Supervisor : Prof. Dr. Faruk KARADAĞ
Year: 2019, Pages: 111
Jury : Assoc. Prof. Dr. Ahmet EKİCİBİL
: Prof.Dr. Metin ÖZDEMİR
: Asst. Prof. Dr. Ali Osman AYAŞ
: Asst. Prof. Dr. Mustafa AKYOL
: Asst. Prof. Dr. Doğan KAYA

In this thesis, we have studied Fe(Se,Te) single crystal, polycrystal and wire by using different processes in order to improve the structural and the superconducting properties of Fe(Se,Te) and to dope FeSe with Ag making superconducting crystal and wire from it. Synthesis and characterization of $FeSe_{0.5}Te_{0.5}$ single crystals prepared by self-flux technique with two different cooling rates of 1.45 and 5.83 °C/h have been investigated. The crystal structure of both samples unchanged by using different cooling rate. The superconducting transition temperatures of two samples obtained as magnetization measurement are seen to be 14.62 and 14.38 K for rapid and slow cooling samples, respectively. $Fe_{1+d}Se_{0.4}Te_{0.6}$ (d = 0, 5, 10 %) polycrystals have been synthesized by using solid state method, in order to investigate the effect of Sulfur annealing in the various amount of excess iron. The as-grown crystals begin to decrease superconducting transition temperature with increasing the amount of iron. After Sulfur annealed, the diamagnetic signal is strongly enhanced and superconducting transition temperature reach up to 14.5 K with incerasing the amount of excess iron. Synthesis and characterization of Ag doped $FeSe_{0.94}$ polycrystals prepared by melting have been investigated for the as-grown and the annealed samples. The XRD pattern of both samples indicate that it is mainly composed of the tetragonal. Superconductivity appears at temperature ~ 8 and 9.2 K for the as-grown and the annealed samples, respectively. Fe(Te,Se) wires were fabricated by using *in-situ* and *ex-situ* PIT process. For *in-situ* PIT process, in the Fe(Se,Te) wire, zero resistivity is not observed due to the Fe sheath introduces much excess iron and accompany by evaporation of chalcogenides in the Fe(Se,Te) phase, which degrade the superconductivity. We have successfully obtained zero resistivity for $Fe(Te_{0.3}Se_{0.7})_{1.5}$ superconducting wires using *ex-situ* PIT process for two different heating process, 800°C+5h; 800°C+25min. Apart from that, we have successfully obtained zero resistivity for two different heating process, 400°C+100h+furnace cooling; 400°C+100h+quench, in the Ag-doped $FeSe_{0.94}$ superconducting wires which were fabricated by using the *ex-situ* PIT method.

Key Words: Fe-based superconductors, wire, critical temperature, critical current, flux mechanism

ÖZ

DOKTORA TEZİ

FeSe-11 SÜPERİLETKEN KRİSTAL VE TEL ÜRETİMİ VE KARAKTERİZASYONU

Derya FARİSOĞULLARI

ÇUKUROVA ÜNİVERSİTESİ
FEN BİLİMLERİ ENSTİTÜSÜ
FİZİK ANABİLİM DALI

Danışman : Doç. Dr. Ahmet EKİCİBİL
İkinci Danışman : Prof. Dr. Faruk KARADAĞ
Yıl: 2019, Sayfa: 111
Jury : Doç. Dr. Ahmet EKİCİBİL
: Prof. Dr. Metin ÖZDEMİR
: Dr. Öğr. Üyesi Ali Osman AYAŞ
: Dr. Öğr. Üyesi Mustafa AKYOL
: Dr. Öğr. Üyesi Doğan KAYA

Bu tezde, Fe(Se,Te) ve gümüş katkılı FeSe'nin yapısal ve süperiletkenlik özelliklerinin geliştirilmesi amacıyla farklı üretim yöntemleri kullanılarak bunların tek kristal, polikristal ve tel üretimi yapıldı. Tek kristal $FeSe_{0.5}Te_{0.5}$'nin üretimi, self-flux yönteminde iki ayrı soğutma oranı (1.45°C/h ve 5.83°C/h) ile gerçekleştirildi. İki farklı soğutma oranı kristal yapıda herhangi bir değişikliğe sebep olmadığı görüldü. Süperiletkenlik geçiş sıcaklıklarını belirlemek için manyetizasyon ölçümü gerçekleştirilmiş olup, hızlı soğutulan numune için 14.62 K; yavaş soğutulan numune için ise 14.38 K olarak bulundu. Çeşitli oranlarda fazla demir katkılaması elde edilen numunelerde sülfür tavlama etkisini incelemek için katıhal metodu kullanılarak $Fe_{1+d}Se_{0.4}Te_{0.6}$ (d = 0, 5, 10%) polikristalleri üretildi. As-grown polikristallerin artan demir miktarına ters orantılı olarak süperiletkenlik özelliklerini kaybettiği gözlemlendi. Yapılan sülfür-tavlama sonrasında ise süperiletkenlik geçiş sıcaklığının tüm numunelerde 14.5 K'ne ulaştığı görüldü. Melting yöntemi ile as-grown ve tavlama yapılan gümüş katkılı $FeSe_{0.94}$ polikristalerin yapısal ve süperiletkenlik özellikleri incelendi. XRD desenlerinde tetragonal kristal yapısı gözlemlendi. Süperiletkenlik geçiş sıcaklığı 8 K (as-grown) ve 9.2 K (tavlama) olduğu gözlemlendi. Fe(Se,Te) telleri *in-situ* ve *ex-situ* PIT ile üretildi. *In-situ* PIT ile üretelen telde demir tüpten fazla miktarda demir geçişi ve kalkojen buharlaşması sebebi ile sıfır dirence ulaşılamadı. *Ex-situ* PIT yöntemi ile üretilen telde ise uygulanan her iki ısıl işlemde (800°C+5h; 800°C+25min) de sıfır dirence ulaşıldı. Öte yandan *ex-situ* PIT ile üretilen gümüş katkılı FeSe'de de uygulanan ısıl işlemlerde (400°C+100h+fırında soğutma; hızlı soğutma) de sıfır dirence ulaşıldı.

Key Words: Fe-tabanlı superiletken, tel, kritik sıcaklık, kritik akım yoğunluğu, akı mekanizması

GENİŞLETİLMİŞ ÖZET

2008 yılında, Kamihara ve arkadaşlarının demir tabanlı $LaFeAs[O_{1-x}F_x]$ bileşiğinin 26 K'de süperiletkenlik sergilediğini keşfetmesiyle bu alana olan küresel ilgi tekrar canlandı ve süperiletkenliğe yeni pencereler açılmış oldu (Kamahira ve ark., 2008). İlk olarak, süperiletkenlik ile manyetizmanın birlikte var olabilirliği araştırmacıların ilgisini bu noktaya çekerek araştırmacılar için, bu aileye mensup bileşiklerin çok daha geniş bir çeşitliliğe ve çok bantlı elektronik yapıya sahip olması sebebiyle yüksek sıcaklık süperiletken mekanizmasını keşfetmek ve T_c'yi artırmak için bir yol bulma umudu olmuştur. Öte yandan Fe tabanlı süperiletkenler birçok teknolojik uygulama için ümit vaad ediyor.

Dört elementli LaFeAsO(F)-1111 süperiletkenin keşfinden itibaren süperiletkenlikten sorumlu mekanizmaya açıklık getirmenin yanı sıra hem bu serinin T_c sıcaklığını artırmak hem de yeni Fe tabanlı süperiletken bileşik bulmak için bu alandaki çalışmalar ivme kazandı. Kısa bir süre içinde, bir yandan 1111 serisine farklı element katkılanmasıyla kritik sıcaklık 55 K'e (Sm katkılaması ile) ulaşırken öte yandan en az dört tip Fe tabanlı süperiletken daha bulundu (Wang ve ark., 2008; Rotter ve ark., 2008; Yeh ve ark., 2008; Fujioka ve ark.,2013).

Fe tabanlı süperiletkenler arasında FeSe-11 sistemi en basit kristal yapıya sahip olan ve FeAs tipi süperiletken örneklerinin protipi olarak görülmektedir. Üst kritik alanının yüksek ve kristalografik anizotropisinin düşük olmasından dolayı yüksek manyetik alan altındaki uygulamalar için en uygun materyallerden biri olduğu düşünülmektedir. Ayrıca, FeAs tabanlı bileşiklere kıyasla daha az toksik madde içermesi ve çevresel basınçla 8 K'de süperiletkenlik sergilemesine karşın yüksek basınç altında T_c 37 K'e ulaşması dikkat çeken diğer özelliklerinden biridir. Böylece 11 sistemi süperiletken teknolojik uygulamalarda kullanılabilecek en iyi adaylardan biridir (Hsu ve ark., 2008; Medvedev ve ark., 2009).

Bu tez kapsamında, tek kristal, polikristal ve tel formunda Fe(Se,Te) ve gümüş katkılı FeSe'nin yapısal ve süperiletkenlik özelliklerini geliştirmek için farklı üretim metodları kullanılarak sentezlenmiştir.

İlk olarak, self-flux metodu ile üretilen tek kristal $FeSe_{0.5}Te_{0.5}$'nin yapısal ve süperiletkenlik özelliklerini irdelemek ya da karşılaştırmak için 1.45°C/h ve 5.83°C/h olarak iki soğutma oranı uygulanmıştır.

XRD desenlerinde yavaş ve hızlı soğutulan örnekleri için tetragonal *P4/nmm* uzay grubu yapısına sahip olan (001), (002), (003) ve (004) indis değerlerinde dört şiddetli ve dar pik gözlemlenmiştir. İki farklı soğutma oranı kristal yapıda herhangi bir değişikliğe sebep olmazken, yavaş soğutulan tek kristal

$FeSe_{0.5}Te_{0.5}$'nin piklerinin şiddeti artırmıştır. Tek kristallerin örgü parametreleri ise hızlı soğutulan (5.83°C/h) kristal için a = 3.8029 Å, c = 6.0154 Å; yavaş soğutulan (1.45°C/h) kristal için ise a = 4.0151 Å, c = 6.0204 Å olarak hesaplanmıştır. Tek kristallerin yüzey morfolojisi ve elemental kompozisyonlarını araştırmak için SEM ve EDX analizleri yapılmıştır. SEM analizine göre, her iki tek kristalde de teras benzeri yapı oluştuğu gözlemlenmiştir. EDX analizinden kompozisyon oraları; hızlı soğutulan numune için $FeSe_{0.5}Te_{0.5}$ ve yavaş soğutulan numune için ise $Fe_{0.98}Se_{0.56}Te_{0.43}$ olarak hesaplanmıştır. Elemental haritalama analizinde ise, her bir elementin (Fe, Se, Te) yüzeye homojen olarak dağıldığı gözlemlenmiştir. Süperiletkenlik geçiş sıcaklıklarını belirlemek için sıcaklığa bağlı manyetizasyon ölçümleri sıfır alan soğutmalı (ZFC) ve alan soğutmalı (FC) olmak üzere iki koşulda 50 Oe manyetik alan altında 8-50 K sıcaklık aralığında gerçekleştirilmiş olup, hızlı soğutulan numune için 14.62 K; yavaş soğutulan numune için ise 14.38 K olarak bulunmuştur. Akım yoğunluğu, alt kritik manyetik alan, çivile mekanizması gibi süperiletkenlik özelliklerini irdelemek için manyetik alana bağlı manyetizasyon ölçümleri 5, 7, 9, 11 K sıcaklıklarında gerçekleştirilmiştir. Alt kritik alan değerleri 5 K'de hızlı soğutulan numune için 287 Oe, yavaş soğutulan numune için ise 209 Oe olarak bulunmuştur. Akım yoğunluğu 5 ve 7 K'de Bean formülü kullanılarak her bir numune için hesaplanmıştır. Hızlı soğutulan numunenin akım yoğunluğu yavaş soğutulan numuneye kıyasla üç kat daha fazla bulunmuştur. Akı çivileme kuvveti $\mathbf{F_p} = J_c \times \mathbf{H}$ ile hesaplanmıştır. Akı çivileme davranışını incelemek için Dew-Hughes (1974)'in geleneksel süperiletkenler için tanımladığı $f_p = Ah^p(1-h)^q$ formülü yardımıyla akı çivileme yoğunlukları hesaplanmıştır. Hızlı soğutulan numune için 5 ve 7 K sıcaklıklarında A = 2.73, p = 0.81 ve q = 0.69, oranları ise $[p/(p+q)] \sim 0.54$ olarak hesaplanmış olup bu sonuçlar doğrultusunda δT_c-tipi çivileme mekanizmasına sahip olduğu bulunmuştur.

İkici olarak, katıhal metodu ile üretilen polikristal $Fe_{1+d}Se_{0.4}Te_{0.6}$ (d = 0, 5, 10 %)'nin yapısal ve süperiletkenlik özellikleri as-grown ve sülfür tavlama yapılarak incelenmiştir.

As-grown polikristallerin XRD desenlerinde tetragonal kristal yapısının baskın olduğu ancak hegzagonal Fe_7Se_8 yapısına ait bir pik de bulunmuştur. Her bir polikristalin örgü parametreleri fullprof programı kullanılarak rietveld analizi ile hesaplanmıştır. $Fe_{1+d}Se_{0.4}Te_{0.6}$ d = 0 % için a = 3.8017 Å, c = 6.0599 Å; d = 5 % için a = 3.7980 Å, c = 6.0566 Å; d = 10 % için ise a = 3.7934 Å, c = 6.0197 Å olarak bulunmuştur. Süperiletkenlik geçiş sıcaklıklarını belirlemek için sıcaklığa bağlı manyetizasyon ölçümleri sıfır alan soğutmalı (ZFC) ve alan soğutmalı (FC) olmak üzere iki koşulda 10 Oe manyetik alan altında 2-20 K sıcaklık aralığında

gerçekleştirilmiştir. As-grown polikristallerin artan demir miktarına ters orantılı olarak süperiletkenlik özelliklerini kaybettiği gözlemlenmiştir.

Sülfür tavlama sonrasında ise aynı koşullarda ölçülen sıcaklığa bağlı manyetizasyon ölçümleri sonucunda tüm numunelerde bulk süperiletkenlik gözlemlenmesi ile birlikte süperiletkenlik geçiş sıcaklıkları 14.5 K'e ulaştığı görülmüştür. Daha sonra süperiletkenlik özelliklerinin artması ile yapısal özellikleri arasındaki ilişkiyi incelemek için fullprof programı kullanılarak rietveld analizleri yapılmıştır. Bu analizler sonucunda, $Fe_{1+d}Se_{0.4}Te_{0.6}$ d = 0 ve 5 % numunelerinde extra demir ortorombik FeS ikinci faz oluşumu ile dışarı atılırken, d = 10 % numunesinde ise extra demir sayesinde sülfür FeSeTe yapısına katılarak dörtlü (Fe-Se-Te-S) yapı oluşturmasının yanı sıra ortorombik FeS ikinci faz oluşumuna da sebep olduğu bulunmuştur.

Üçüncü olarak, melting yöntemi ile as-grown ve tavlama yapılan gümüş katkılı FeSe polikristalerin yapısal ve süperiletkenlik özellikleri incelenmiştir.

As-grown ve tavlanan polikristallerin XRD desenlerinde tetragonal kristal yapısının yanı sıra $2\theta \approx 31°$ civarında hegzagonal Fe_7Se_8 piki ve $2\theta \approx 38°$'de de saf gümüş piki gözlemlenmiştir. Her iki polikristal için örgü parametreleri fullprof programı ile hesaplanmış olup, as grown polikristali için a = 3.7683 Å, c = 5.5139 Å, tavlanan polikristal için ise a = 3.7673 Å; c = 5.5166 Å olarak bulunmuştur. Süperiletkenlik sıcaklıkları belirlemek için sıcaklığa bağlı manyetizasyon ölçümleri sıfır alan soğutmalı (ZFC) ve alan soğutmalı (FC) olmak üzere iki koşulda 100 Oe manyetik alan altında 2-20 K sıcaklık aralığında ve tavlama yapılan numunenin sıcaklığa bağlı özdirenç ölçümleri 4-300 K aralığında gerçekleştirilmiştir. M(*T*) sonucunda, süperiletkenlik geçiş sıcaklığı as-grown polikristali için 8 K olarak bulunmuştur. Sıcaklığa bağlı özdirenç ölçümü sonucunda tavlanan numune için süperiletkenlik geçiş sıcaklığı 9.2 K olarak bulunmuştur.

Dördüncü olarak, *in-situ* powder-in-tube (PIT) yöntemi ile Fe(Se,Te) teli üretilip, elde edilen tele iki ısıl işlem (850°C+2h; 700°C+2h) uygulanarak yapısal ve süperiletkenlik özellikleri incelenmiştir.

In-situ PIT ile üretelen Fe(Se,Te) tele uygulanan ilk ısıl işlem (850°C+2h) sonucunda, XRD deseninde tetragonal kristal yapısının baskın olduğu ve $2\theta \approx 32°$'de hegzagonal FeTe piki gözlemlenmiştir. Örgü parametreleri ise a = 3.7931 Å ve c = 6.0181 Å olarak hesaplanmıştır. *In-situ* PIT ile üretelen Fe(Se,Te) tele uygulanan her iki ısıl işlem (850°C+2h; 700°C+2h) için SEM ve EDX analizleri yapılmıştır. Yapılan analizine göre, Fe(Se,Te) kompozisyonu oluşumu için demir tüpten demir geçişi olduğu gözlemlenmesi ile birlikte Se : Te = 1 : 1 oranında

kullanıldığı halde kalkojen miktalarında kayde değer azalma olduğu gözlemlenmiştir. Sıcaklığa bağlı özdirenç ölçümleri sonucunda süperiletkenlik geçiş sıcaklığı bulunmasına rağmen sıfır dirence ulaşılamamıştır. Bunun nedeni olarak da demir tüpten demir geçişi gerçekleşmesine rağmen kalkojenlerin buharlaşması sebebiyle uygun kompozisyona ulaşılamamıştır.

Beşinci olarak, *ex-situ* PIT yöntemi ile $Fe(Se_{0.7}Te_{0.3})_{1.5}$ teli üretilip, elde edilen tele iki ısıl işlem (800°C+5h+fırında soğutma; 800°C+25min+hızlı soğutma) uygulanarak yapısal ve süperiletkenlik özellikleri incelenmiştir.

Ex-situ PIT ile üretelen $Fe(Se_{0.7}Te_{0.3})_{1.5}$ tele uygulanan her iki ısıl işlem sonucunda, XRD desenlerinde: ilk ısıl işlem (800°C+5h+fırında soğutma) sonucunda $Fe_{0.97}Se_{0.91}Te_{0.09}$ tetragonal ve $Fe_{1.05}Se_{0.05}Te_{0.95}$ teragonal olmak üzere iki kristal yapıya ayrıştığı gözlemlenmiştir. İkinci ısıl işlemde (800°C+25min+hızlı soğutma) ise tetragonal FeSe ve tetragonal FeTe olmak üzere iki kristal yapısına ayrıştığı gözlemlenmiştir. Sıcaklığa bağlı özdirenç ölçümleri sonucunda ise her iki ısıl işlemde de ~ 7 K'de sıfır dirence ulaşılmıştır. Manyetik alana bağlı özdirenç ölçümlerinden üst kritik alan, $\mu_0 H_{c2}$ (0 K), ve tersinmezlik alanı, $\mu_0 H_{irr}$ (0 K), hesaplanmış olup, birinci tel (800°C+5h+fırında soğutma) için sırasıyla 14.1 ve 7.9 T olarak bulunmuştur. İkinci tel için ise $\mu_0 H_{c2}$ (0 K) 17.4 T ve $\mu_0 H_{irr}$ (0 K) ise 11.3 T olarak bulunmuştur.

Son olarak *ex-situ* PIT yöntemi ile gümüş katkılı FeSe teli üretilip, elde edilen tele iki ısıl işlem (400°C+100h+fırında soğutma; 400°C+100h+hızlı soğutma) uygulanarak yapısal ve süperiletkenlik özellikleri incelenmiştir.

Ex-situ PIT ile üretelen gümüş katkılı FeSe tele uygulanan her iki ısıl işlem sonucunda; XRD desenlerinde tetragonal kristal yapısı ile birlikte $2\theta \approx 31°$'de hegzagonal Fe_7Se_8 piki sergilediği gözlemlenmiştir. Tellerin örgü parametreleri ise birinci tel (400°C+100h+fırında soğutma) için a = 3.7660 Å, c = 5.5103 Å, ikinci tel (400°C+100h+hızlı soğutma) için de a = 3.7685 Å and c = 5.5143 Å olarak bulunmuştur. Sıcaklığa bağlı özdirenç ölçümleri sonucunda her iki ısıl işlemde de sıfır dirence başarılı bir şekilde ulaşılmıştır.

ACKNOWLEDGEMENTS

My work could not be done without much help from many people.

I am grateful to my supervisors, Assoc.Prof.Dr. Ahmet Ekicibil and Prof.Dr. Faruk Karadağ for their valuable guidance during my work.

I am grateful to Yoshihiko Takano who opened the doors of National Institute for Materials Science (NIMS) during one year and Prof.Dr. Bekir Özçelik for his guidance during my work.

I have been grateful to Dr. Michal Babij for his kind assistance with my experiments. He has offered his expertise and help consistently whenever I have met any problems in the laboratory.

I am sincerely grateful for all my dearest friends who have accompanied me through my PhD: I would love to thank Bahar Ulaş, Assoc.Dr. Gülten Kavak Balcı, Dr. Pelin Tozman Karanikolas, Dr. Ahmet Yağmur, PhD student Cem Özbilgin, Dr. Vasilios Karanikolas, Dr. Gülay Altındemir, Dr. Henry Wafula, PhD student İrem Özbilgin, Lawrence Alan Chambers, Anna Deschain especially for their optimism throughout my studies, for constantly encorugating me whenever I met difficulties in research or life.

I am grateful to the Scientific and Technological Research Council of Turkey (TUBİTAK) for their generous funding me to the visiting period in National Institute for Materials Science (NIMS), Tsukuba, Japan.

Last, but not least, words cannot express how grateful I am to my parents who I love very much for always standing by my side regardless of my life-changing decisions, for loving me continuously and unconditionally so that I could be myself and for continually being excited as I have reached my dreams.

The thesis is dedicated to my nephew who is now in heaven:

I love Berat very much…

CONTENTS **PAGE**

LIST OF TABLES **PAGE**

LIST OF FIGURES **PAGE**

ABREVIATONS

Å	: Angstrom
Ar	: Argon
Ag	: Silver
B	: Magnetic induction
BCS	: Bardeen-Cooper-Schrieffer theory
E	: Electric field
e^-	: Electron charge
EDS	: Energy Dispersive X-Ray
ETO	: Electronic Transport Option
eV	: Electron volt
Fe	: Iron
H	: Applied magnetic field
$\mathbf{H_c}$	: Critical magnetic field
$\mathbf{H_{c2}}$	: Upper critical magnetic field
$\mathbf{H_{irr}}$	: Irreversible magnetic field
h	: Planck constant
I	: Current
J	: Current density
J_c	: Critical current density
K	: Kelvin
k_B	: Boltzman constant
M	: Magnetization
NIMS	: National Institute for Materials Science
Oe	: Oersted
ξ	: Coherence distance
λ_L	: London penetration depht
κ	: Gizburg-Landau parameter

ρ	: Resistivity
PPMS	: Physical Property Measurement System
R	: Resistance
Se	: Selenium
S	: Sulfur
SEM	: Scanning Electron Microscopy
T	: Temperature
T_c	: Superconducting transition temperature
T_c^{onset}	: The onset superconducting temperature
T_c^{mid}	: The mid-point superconducting temperature
T_c^{offset}	: The zero-resistivity temperature
Te	: Tellurium
XRD	: X-Ray Diffraction
VSM	: Vibrating Sample Magnetometer

1. INTRODUCTION

1.1. Research Background

After the first report of superconductivity in LaFePO and LaNiOP below 5 K (Kamihara et al., 2006; Watanabe et al., 2007), the science world received another surprise in 2008 when it was discovered that fluorine-doped lantanum oxygen iron arsenide $La(O_{1-x}F_x)FeAs$ (x = 0.08) transitions to superconductivity at an incredible 26 K (Kamahira et al., 2008). This report was unexpected because iron is an archetypal ferromagnetic and a ubiquitous element on Earth. And for this reason is not compatible with superconductivity, as the spin-singlet nature of the Cooper pair quasiparticles in normal superconductors is made up of superconducting condensate. After that discovery, researchers all over the world focused on investigating whether any other ferrous compound exhibits superconductivity at the same or higher obtaining magnitude T_c as that of $La(O_{1-x}F_x)FeAs$. In 2008 alone, this family grew to encompass nearly 100 different ferrous compounds recognized as exhibiting superconductivity. Just three months after the initial discovery, the critical temperature of the same compound increased drastically to 43 K under hydrostatic pressure (Takahashi et al., 2008). This was quickly followed by reports that replacing the La in $La(O_{1-x}F_x)FeAs$ with other rare earth elements Ce (Chen et al., 2008) or Sm (Liu et al., 2008), or the Gd in the compound GdFeAsO with Th (Wang et al., 2008) resulted in critical temperatures of 41, 54, and 56 K, respectively.

Soon afterward, it was found that oxygen vacancies induced superconductivity in $ReFeAsO_{1-\delta}$ under hydrostatic pressure (Ren et al., 2008). The FeAs-based family of superconductors grew rapidly with the discovery that it included alkali-doped compounds $A_{1-x}B_xFe_2As_2$ (A = alkaline earth, B= alkali metal) (Rotter et al., 2008) and the ternary LiFeAs (Wang et al., 2008).

Another ferrous compound found to exhibit superconductivity, β–FeSe — with a simple crystal structure and no charge reservoir plane — has a critical

transition temperature of ~ 8 K (Hsu et al., 2008). Its superconducting transition temperature increases sharply to 15 K when tellerium is substituted for selenium, to 30 K when the iron selenium is intercalated with potassium, and to 37 K when it is prepared under hydrostatic pressure (Yeh et al., 2008; Medvedev et al., 2009; Guo et al., 2010).

So, the parent materials of iron-based superconductors are classified by crystal structure into five main types: 1111, which crystallizes in a tetragonal ZrCuSiAs type with space group *P4/nmm* (MFePnO*, M: lanthanide,* NFeAsF*, N: alkaline earth, Pn: P, As*); 111, which has a CeFeSi crystal structure type with a tetragonal *P4/nmm* space group (M*FePn, M: alkali metal*); 122, which crystallizes in a $ThCr_2Si_2$ type with a tetragonal *I4/mmm* space group (AFe_2Pn_2*, A: alkali, alkaline earth* or *Eu*); 11, which has an anti-PbO type crystal structure with a tetragonal *P4/nmm* space group (*Fe_{1+x}Ch, Ch: Se, Te, S*); and 245, which has a $ThCr_2Si_2$ type crystal structure with *I4/mmm* ($M_{1-x}Fe_{2-y}Se_2$*: M=K, Cs, Rb, Tl*) (Dong et al., 2013; Chang et al., 2014; Hosono et al., 2015).

Immediately after the discovery of iron-based superconductors, researchers focused on the most important questions: namely, how superconductivity occurs in the iron-based family, and what the key role of that family is in superconductivity. All of the iron-based superconductor parents' structure units consist of alternating rare earth element/alkali/alkaline earth (*REO/A*), and *FePn/Ch* layers, rendering charge carriers and conducting planes, respectively. Each parent compound contains a common layered stucture based on a square planar Fe layer tetrahedrally constructed of four *Pn* or *Ch* atoms. This layer is responsible for superconductivity via magnetic fluctuation in iron-based superconductors. Fermiologists agree that the iron plane plays a key role in superconductivity because the Fermi level of each parent compound mainly contributes charge carries by five Fe *3d* orbitals. Also, it is the only element among the transition metals that exhibits superconductivity at 2 K at pressures ranging between 15 and 30 GPa (Shimizu et.al, 2001) (At such high pressures, iron transforms itself from a ferromagnet into a weak antiferromagnet at

this low temperature). Of course, *Pn* and *Ch* atoms also play a role because their *p* orbital hybridizes with the five *3d* orbitals of Fe, which gives rise to the multiband structure of the Fermi surface (Ivanovskii, 2008).

Iron-based superconductors have been found to be promising candidates for large scale applications, especially at low temperatures and high fields, because of their very advantangeous properties. Firstly, the robustness of the critical transition temperature (T_c), *i.e.* its ability to resist change in spite of impurities, is extremely high. Secondly, the upper critical magnetic fields ($\mathbf{H_{c2}}$) and irreversibility fields ($\mathbf{H_{irr}}$) are quite high. $\mathbf{H_{c2}}$ values ranging between 100-200 T for 1111-type, 50-100 T for 122-type and ~ 50 T for 11-type (Johnston, 2010). For this reason, iron-based superconductors have the potential for being used as high magnetic field magnets, a prime example of which being a superconducting magnetic energy storage (SMES), because the magnetic energy stored in an SMES is proportional to the $\mathbf{B_2}$ (Bray, 2009). A third advantage is that the crystallographic anisotropy factors (γ) are small, ranging between 4 and 5 for type 1111, and between 1 and 2 for types 122 and 11 (Johnston, 2010). These first three properties are suitable for the fabrication and application of superconducting wires, tapes, and coated conductors. One final advantage of iron-based superconductors is their higher critical current, J_c, specifically one $> 10^5$ A/cm^2 under the high magnetic fields demonstrated for 11, 122, and 1111 films. These films are especially suitable for thin-film josephson junctions and superconducting quantum interference devices (SQUIDs).

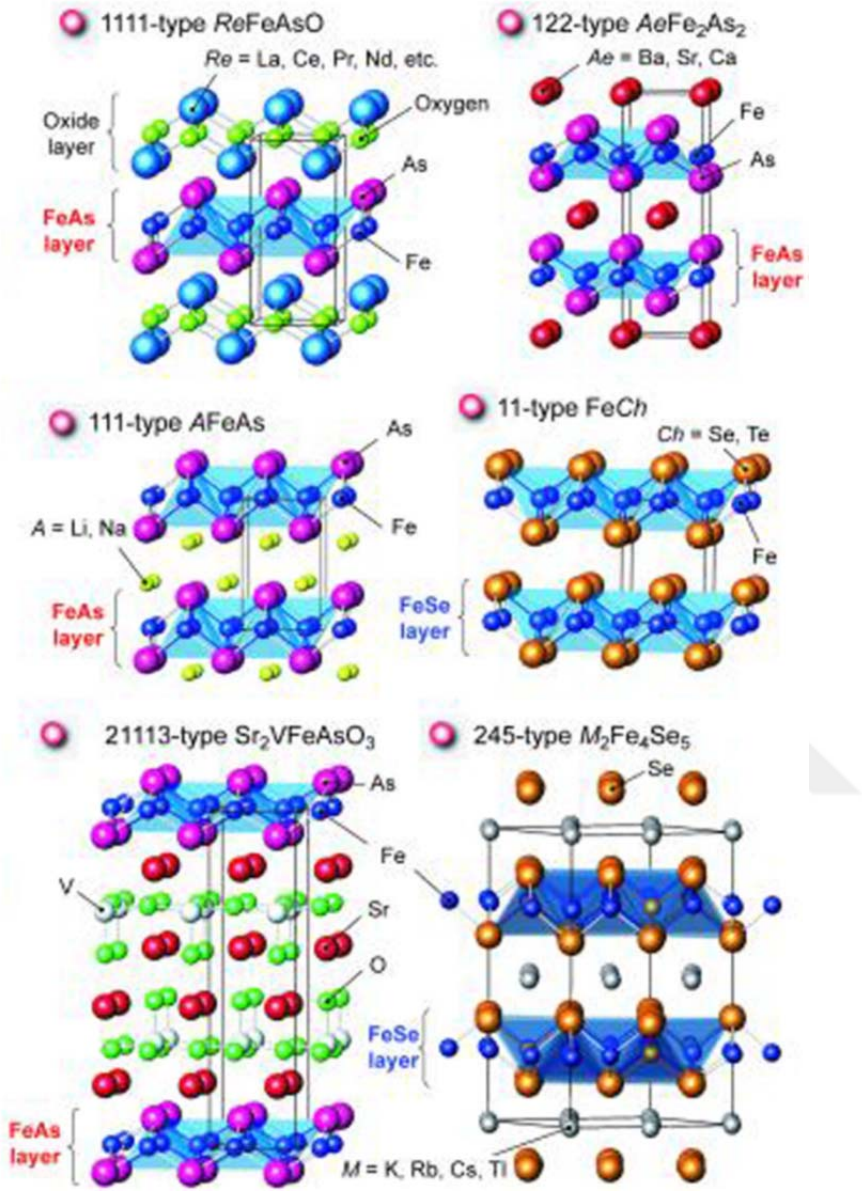

Figure 1.1. Schematic representation the structure of the parent materials of iron-based superconductors (Hosono et al., 2018).

1.2. Subject and Aims of This Thesis

Fe(Se,Te) is a member of the 11-type parent of iron-based superconductors. It has opened a new door in the condensed matter physics

community because β-FeSe crystallizes at room temperature into a tetragonal PbO-type structure and contains an Fe_2Se_2 layer of edge-shared $FeSe_4$ tetrahedra. This gives β-FeSe the simplest structure among the iron-based superconductors. So iron chalcogenide superconductors are an excellent system to elucidate the superconducting mechanism of iron-based superconductors. Morever, this parent has significant potentional for application due to its high $\mathbf{H_{c2}}$, high $\mathbf{H_{irr}}$, large J_c, and low anisotropy. All this shows that the 11 parent is the cornerstone of the high-field superconducting magnets and energy-related applications using wire and/or tape. The $\boldsymbol{T_c}$ range is suitable for use in refrigerators (~ 10 K) and liquid hydrogen (~ 20 K). In order for an Fe(Se,Te) bulk superconductor to carry current under a high magnetic field or self-field, it is necessary to process Fe(Se,Te) materials in the form of large, single grains to prevent the presence of grain boundaries, cracks, and voids.

Prossesing Fe(Se,Te) superconductors is quite complicated because the superconductivity of this parent is extremely sensitive to stoichiometry. Because the phase diagram of FeSe itself is complicated and stems from nonstoichiometricity, and because the differences in both the melting temperatures and the diffusion rates of Fe and chalcogenide are relatively high. Additionally, the formation of grain boundaries, pores, and cracks in the superconducting matrix of Fe(Se,Te) crystal and wire superconductors is detrimental to their mechancial properties.

This thesis is geared toward addressing these challenges by using different processes in order to enable and/or improve the superconducting properties of Fe(Se,Te) and to dope FeSe with Ag prior to making superconducting crystal and wire from it.

2. LITERATURE REVIEW

2.1. Evoluation of Superconductors and Their Application

In the phenomenon of superconductivity, a material suddenly loses all electrical resistance to the flow of direct current (DC) at a certain temperature, called the superconducting transition temperature. The era of superconductivity was heralded by the discovery in 1911 of H. Kamerling Onnes and his assistant Gilles Holts that the resistance of mercury (Hg) disappears below 4.2 K (Marouchkine, 2004). Onnes won a Nobel Prize for this in 1913.

The history of superconductivity as a phenomenon is quite rich, consisting of many discoveries and events. Figure 2.1 displays the historical evolution of the transition temperature ($\boldsymbol{T_c}$) subsequent to the finding of superconductivity. At present, tens of thousands of compounds are known to be superconductors, and all of them can be classified into three main groups according to their crystal stucture and their properties (Marouchkine 2004).

Metals and some of their alloys make up the first of these groups. It includes all conventional superconductors, whose T_c value does not exceed 10 K. Most of them are Type-I superconductors. Over half the chemical elements in the periodic table are such conventional superconductors, as is shown in Table 2.1. Superconductivity occurs either at ambient pressure or under hydrostatic pressure. In 1913, lead (Pb) was found to become a superconductor at 7.2 K (Roberts, 1976). In 1930, superconductivity was discovered in niobium (Nb) at 9.2 K (Meissner et al., 1930). This is the highest critical transition temperature of any of the members of the first group of superconductors.

The next major breakthrough step in understand how matter behaves at extremely cold temperatures occured in 1933. W. Meissner and R. Ochsenfeld found that below the critical temperature ($T < T_c$), if a superconductor is placed in a magnetic field, the magnetic flux is expelled from the interior of the

superconductor. This phenomenon is known today as the *Meissner-Ochsenfeld effect* (Saxena, 2010).

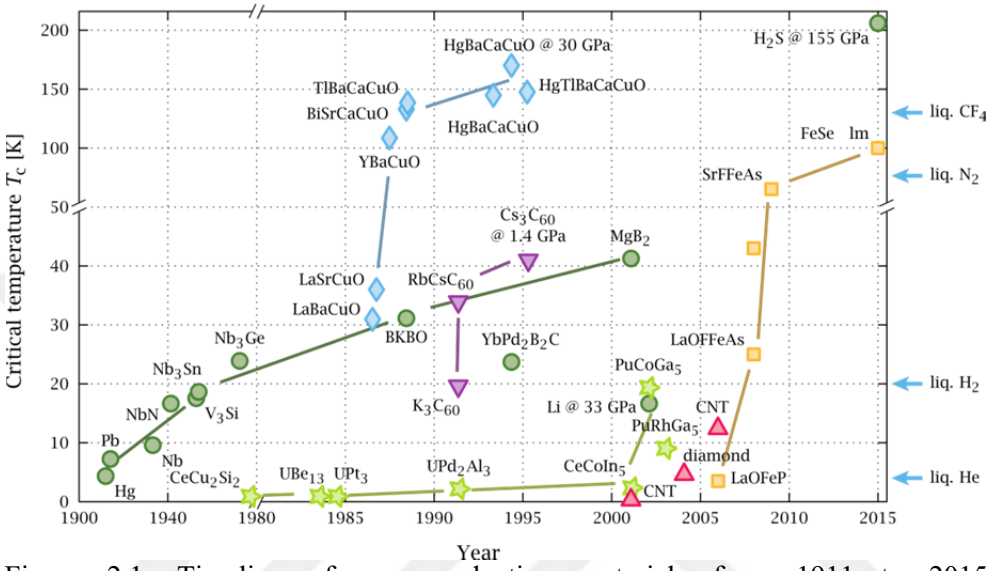

Figure 2.1. Timeline of superconducting materials from 1911 to 2015 (www.commons.wikimedia.org).

Between 1940 and 1980, many more elements and alloys were discovered to be superconductors. In 1941, niobium nitride was to be a superconductor with a transition temperature of 16 K (Editorial, 2015). In 1953, V_3Si was found to become a superconductor at 17.1 K (Hardy et al., 1954), and this type of superconductor is called an A-15 compound. The A-15 type is the same as an M_3N compound, where M is a transition metal of Nb, V, Ta, and Zr, whereas N is one of the nontransition metals such as Sn, Ge, Ga, and Si (Stewart, 2015). Among the A-15 compounds, Nb_3Ge exhibits the highest critical transition temperature at 23.2 K (Saxena 2010). This type of superconductors is used for high field magnetic energy applications due to their high T_c and high upper magnetic field ($\mathbf{H_{c2}}$). In 1975, the metal oxide $BaPb_{1-x}Bi_xO$ (x=0.25) was found to superconduct at 13.7 K (Sleight et al., 1975). This discovery astonished the science world, because it was

the first oxide superconductor. The critical transition temperature of BKBO rose to 30 K in 1988 (Asomba et al., 2015).

Table 2.1. The chart of elemental superconductors (www.es.slideshare.net).

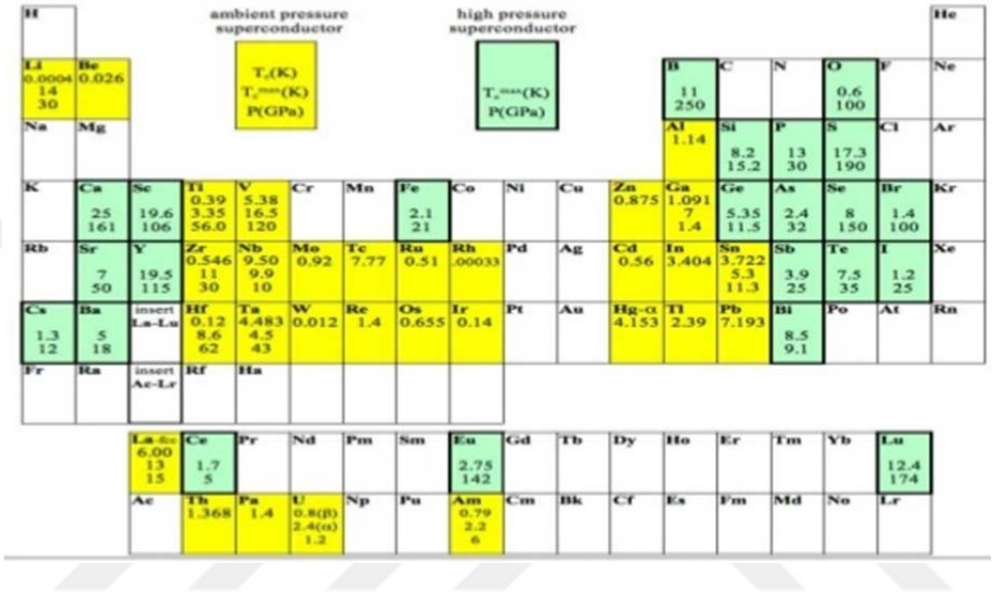

In January 2001, magnesium diboride MgB_2 was found to superconduct at 39 K (Nagamatsu et al., 2001). From the standpoint of industrial applications, Mg_2B is very good due to its slight anisotropy and high $\mathbf{H_{c2}}$, and it is inexpensive to produce because magnesium and boron are plentiful in nature. Laboratory testing has shown that MgB_2 outperforms NbTi and Nb_3Sn wires in high magnetic field applications such as magnetic resonance imaging and nuclear magnetic resonance. There are only a few superconductors in the second group, called *low-dimensional* and *non-magnetic* superconductors. The group is named for the two superconducting subsystems present in each member of the group. One subsystem is low-dimensional and displays genuine superconductivity of an unconventional type, whereas the second is three-dimensional, and its superconductivity is induced by the first one and is of the BCS type. The group's T_c value does not exceed 40

K, and its upper critical magnetic field exceeds 10 T, so all of these are Type-II superconductors (Marouchkine et al., 2002).

The first generally accepted theory of superconductivity was formulated by J. Barden, L. Cooper, and R. Schrieffer in 1957, and is thus known as the BCS theory, for which they won a Nobel Prize in 1972. According to this theory, a weak electron-phonon interaction leads to the occurrence of an attractive potential between two electrons, and they compose Cooper pairs. However, this theory explained superconductivity only at temperatures close to absolute zero for elements and simple alloys.

In 1962, the first commercial superconducting wire was developed at Westinghouse by using an alloy of niobium and titanium (NbTi). In 1960, scientists at the Rutherford-Appleton Laboratory producted copper-clad NbTi for particle accelerator electromagnets, which were first employed in a superconducting accelerator at the Fermilab Tevatron in the US in 1987.

In 1962, another great milestone was passed when a theory of superconductivity was propounded by B.D Josephson, who theoretically predicted that electrical current would flow between two superconducting materials — even when they are separated by an insulator. His predictions were confirmed within a year. He won a Nobel Prize in 1973. This tunneling phenomenon is now known the *Josephson effect* and comprises the heart of electronic equipment like the superconducting quantum interference device.

In 1986, the era of high-temperature superconductivity began when Bednorz and Muller discovered that La-Ba-Cu-O ceramics (LaBCO) superconduct with a transition temperature of 30 K. The importance of this discovery in the science of superconductors cannot be overemphasized, because ceramics are normally insulators and do not conduct electricity well at all. Also, the BSC theory was not adequate to fully explain how superconductivity occurs at such a high T_c. The discovery of this first of the superconducting copper-oxides (cuprates) won the two men a Nobel Prize the following year. In 1987, the critical temperature

increased incredibly to 92 K by substituting yttrium (Y) for lantanium (La) in LaBCO. This significant increase was a turning point in materials science because liquid nitrogen (boiling point = 77 K) could be employed as a coolant due to its availability. This provoked the development of hybrid microelectronic technology (semiconductor-superconductor devices). Within one year, the T_c had risen to 110 K for $Bi_2Sr_2CaCu_3O_{10}$ (Bi-2223), and then to 125 K for $Tl_2Ba_2Ca_2Cu_3O_{10}$ (Tl-2223) (Tinkham, 1996). In 1993, the mercury copper-oxides were discovered, and their critical temperatures increased to a maximum of 135 K with fabricated ambient pressure or 165 K under high pressure (Saxena, 2010). This family belongs to the third group of superconductors, which is *low-dimensional* and *magnetic*. All members of this group are unconventional superconductors, so all of them are Type-II superconductors and the materials have stong magnetic correlations. Unfortunately, to date there is no exact theory explaining unconventional superconductors, so a general description of the mechanism of this type of superconductiviy is mainly based on experimental results of the cuprates.

This last family of superconductors now includes iron-based superconductors. Their discovery has produced a frenzy of reseach in the solid state community. Although numerous iron-based superconductors have been reported, the exact mechanism of their superconductivity is still a mystery. However, many compounds exhibit superconductivity and the highest T_c found so far among iron-based superconductors is 109 K in a single-layer of FeSe. That temperature is above the boiling point of liquid N_2. It has other properties as well that lend this family to many useful purposes. Table 2.2 lists the forms of superconducting materials that are used commonly and are available commercially.

Table 2.2. The most commonly applied superconducting materials.

Materials	Forms	Application
NbTi	wire	MRI, particle accelerator
Nb_3Sn	wire	NMR, fusion accelerators
BSCCO	wire	FCL, SMES
$GdBa_2C_3O_{7-\delta}$	bulk	Maglev
YBCO	wire	Power application. FCL, SMES
Nb or a Pb alloy with 10% Au or In	wire	SQUID

2.2. Fundamental Physics Properties of Superconductivity

2.2.1. The Meissner-Ochsenfeld Effect

When superconductors were found to have zero resistance, it was widely believed, until the discovery of the *Meissner-Ochsenfeld effect* (perfect diamagnetism), that this was the only fundamental property of superconductors. Indeed, the *Meissner-Ochsenfeld effect* is of equal or even greater importance and plays the central role in the magnetic phenomenon associated with superconductivity. This phenomenon is the expulsion of magnetix flux from the interior of a sample that is cooled below its critical temperature in a weak magnetic field (Meissner et al., 1933).

In the superconducting state, the following simple relationship exists between the applied magnetic field **H**, the magnetization **M,** and the magnetic induction **B**:

$$B = \mu_0 (H + M) = 0 \quad (2.1)$$

It means that *inside* the superconductor, the magnetization is found as

$$M = -H \quad (2.2)$$

Thereby, the susceptibility takes on the ideal value for a perfect diamagnet;

$$\chi = \frac{dM}{dH} = -1 \tag{2.3}$$

These two ways of expressing the *Meissner-Ochsenfeld effect* are of course equivalent, yet the diamagnetic statement is physically more expressive and attractive (Fossheim et al., 2004).

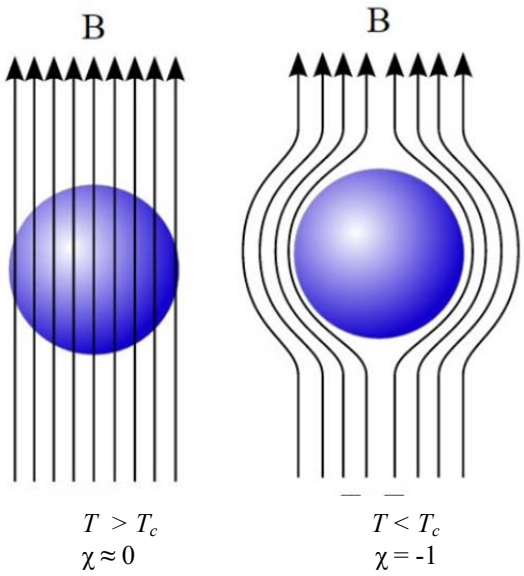

Figure 2.2. The *Meissner-Ochsenfeld effect* in a superconductor (http://ceeielche.emprenemjunts.es).

The most important question is: What happens when a shielding current appears spontaneously on the surface of a material that becomes a superconductor in the presence of a magnetic field? These currents give rise to the complete expulsion of the magnetic field applied inside the superconductor, so the total magnetic field thus becomes equal to zero, and the superconductor is protected, while the shielding currents delevop on the surface. The superconductor expels the

magnetic field due to the surface supercurrents. These currents can exist forever without consuming any energy because of no resistivity in the superconductor.

The *Meissner-Ochsenfeld effect* is related thermodynamically to the *free-enegy* difference between the normal and the superconducting states in a zero field, the so-called condensation energy of a superconducting state:

$$F_n(T) - F_s(T) = \frac{H_C^2(T)}{8\pi} \tag{2.4}$$

where F_n and F_s are the Helmholtz free energies of a normal and superconducting state, respectively, and $\mathbf{H_c}$ is a critical magnetic field. The superconducting state is a more ordered state than the normal state. As a result, the superconducting state is preferable to the normal state from the viewpoint of free energy, yet the superconducting state can be destroyed by the critical magnetic field (Saxena, 2010).

In 1935, F. London and H. London demonstrated that the magnetic flux lines are not completely expelled from a superconductor; rather, they remain confined in a thin surface layer so called the penetration depth (λ):

$$\lambda^2 = \frac{m^* c^2}{4\pi n_s e^2} \tag{2.5}$$

where m^* is the effective mass of a charge carrier, e is the electron charge, and c is the speed of light in vacuum. The magnitude of the penetration depth depends on the material and the temperature, and decreases exponentially toward the core of a superconductor, as shown in Figure 2.3 (Marouchkine, 2002).

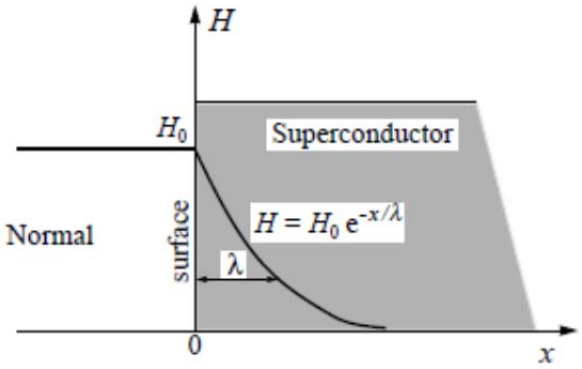

Figure 2.3. Penetration of magnetic field into a superconducting material (Marouchkine, 2004).

2.2.2. The Ginsburg-Landau Theory

In 1950, Ginsburg and Landau proposed a comprehensive theorical picture of superconductivity. Indeed, the GL theory is a limited form of the microscopic BCS theory — although it was proposed seven years before and proven by Gorkov two years after the BCS theory was announced — because the BCS theory concentrates on the energy gap and the excitation spectrum, which play a key role in a constant space. The theory is based on a complex pseudowave-function $\psi(\mathbf{r})$ as an order parameter within Landau's general theory of second-phase transition (the transition into a superconducting state at the critical temperature T_c is of the second order in the absence of a magnetic field) in which $\psi(\mathbf{r})$ is describe as superconducting electrons, and the local density of superconducting electrons was given as

$$n_s = |\psi(\boldsymbol{r})|^2 \tag{2.6}$$

Then, the theory was developed as an expansion of free energy in powers of $|\psi(\boldsymbol{r})|^2$ and $|\Delta\psi(\boldsymbol{r})|^2$. Minimization of the free energy with respect to the order parameter leads then to a differential equation for $\psi(\mathbf{r})$ which is analogous to a

Schrodinger equation for a free particle, but with a nonlinear term. Another major result of this theory is its explanation of the intermediate-state phenomena, in which superconducting and normal domains coexist in the presence of a magnetic field **H** near the critical field $\mathbf{H_c}$ (Tinkham, 1996). The interface between two such domains is shown in Figure 2.4.

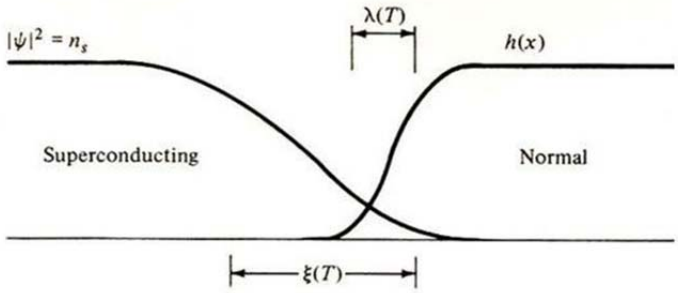

Figure 2.4. Interface between superconducting and normal domains in the intermadiate state (Tinkham, 1996).

Another aspect of the GL theory is that it introduces a characteristic length, today known as the *GL coherence length*,

$$\xi_{GL}\,(T) = \frac{\hbar}{|2m^{*}\alpha(T)|^{1/2}} \tag{2.7}$$

which characterizes the distance over which $\psi(\mathbf{r})$ can vary without undue energy increase (Tinkham, 1996).

2.2.3. Type-I and Type-II Superconductors

In 1957, Abrikosov published a masterstroke paper, overlooked at that time mainly because he used the *Ginzburg-Landau* theory. The theory introduces two fundamental characteristic lengths, penetration depth λ and coherence length ξ_{GL}, that describe the distances over which the magnetic field and the order parameter

can vary, respectively (Cyrot, 1973). The proportion of them define the GL parameter can be given as,

$$\kappa = \frac{\lambda}{\xi_{GL}} \tag{2.8}$$

This dimensionless ratio is independent of temperature. It is an important parameter that characterizes the material of the superconductor. In a pure superconductor $\lambda < \xi_{GL}$ and this leads to a *positive* surface energy associated with a normal superconducting boundary. That is, $\xi H_c^2/8\pi$ energy is lost per unit area for the variation of ψ, from its superconducting value to zero, $\lambda H_c^2/8\pi$ energy is gained per unit area in reducing the magnetic energy, therefore σ_n is equal to (Sexana, 2009);

$$\sigma_n \cong (\xi - \lambda)\frac{H_c^2}{8\pi} \tag{2.9}$$

Hence, a type-I superconductor has a *positive* suface energy and exhibits the complete *Meissner effect*. All superconducting elements are type-I superconductors except for Nb and V.

Abrikosov focused on another question: What would happen in GL theory if κ were larger, namely, $\xi_{GL} < \lambda$. In that case, it would lead to a *negative* surface energy, in which subdivision into domains would continue until it was limited by the microscopic length ξ, below which the gradient energy term would become excessive. He called these type-II superconductors and demonstrated that the exact critical value for negative surface energy is $\kappa = 1/\sqrt{2}$. For materials with $\kappa > 1/\sqrt{2}$, he found that there is a continuous increase in flux penetration, starting at a first critical field $\mathbf{H_{c1}}$ and reaching $\mathbf{H} = \mathbf{H_{c2}}$ at a second critical field, where the

superconductor material becomes normal. Today, $\mathbf{H_{c1}}$ and $\mathbf{H_{c2}}$ are known as the lower and the upper magnetic fields, as given in Figure 2.5

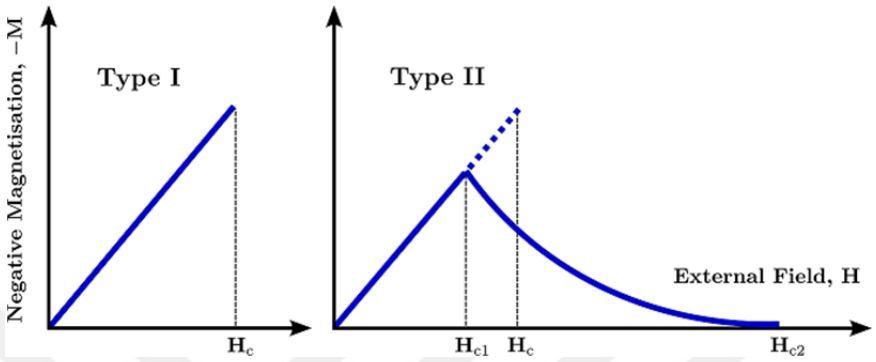

Figure 2.5. Magnetization aganist applied magnetic field for type-I and type-II superconductors.

Because of this partial flux penetration, the diamagnetic energy cost of holding the field out is less and $\mathbf{H_{c2}}$ is greater than $\mathbf{H_c}$ (Tinkham, 1996),

$$H_{c2} = \kappa H_c \sqrt{2} \tag{2.10}$$

After Abrikosov introduced the lower and the upper magnetic fields, he focused on another question: What happens in the state between $\mathbf{H_{c1}}$ and $\mathbf{H_{c2}}$? In 1937, in fact, Shubnikov discovered through expirement *vortices* in the external magnetic fields of some superconductors. Later, Abrikosov theoretically found vortices in 1957 by using the GL theory, and then explained Shubnikov's experiments, suggesting that Shubnikov's phase is a state with vortices. Now the state between $\mathbf{H_{c1}}$ and $\mathbf{H_{c2}}$ is referred to as the *mixed* or *vortex* state, or the Shubnikov phase (Marouchkine, 2002), as shown in Figure 2.6:

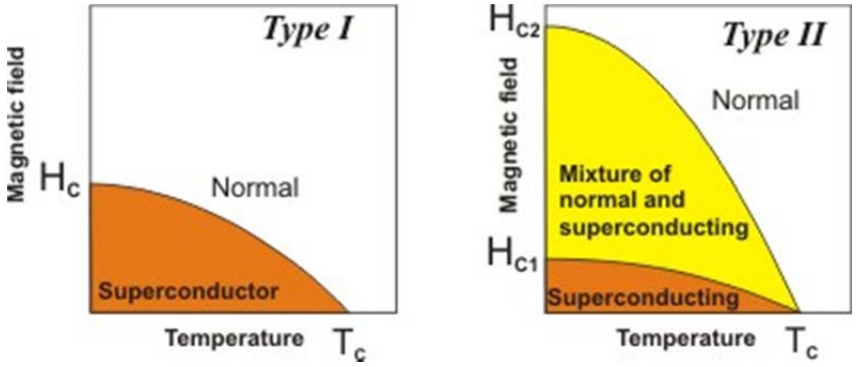

Figure 2.6. Critical magnetic field versus temperature for type-I and type-II superconductors (www.nptel.ac.in).

In this state the material has zero electrical resistance but is not a perfect diamagnet because the flux enters at $\mathbf{H} > \mathbf{H_{c1}}$. A vortex consists of a non-superconducting core that is surrounded by circulating superconducting currents. The core diameter is approximately equal to the coherence length, $2\,\xi_{GL}$, and the circulating supercurrents extend out to the magnetic penetration depth, λ. An isolated vortex in a superconductor carries a magnetic flux equal to the flux quantum $\Phi_0 = hc/2e = 2.07 \times 10^{-7}$ Weber (Kwok et al., 2016).

In equilibrium, the mutual vortices create a regular vortex lattice with minimum free energy. So, energetically, the most favorable regular vortex lattice is triangular.

An external electrical current density J creates a Lorentz force acting on the vortex line perpendicular to both the current direction and the unit vector along the line $\mathbf{n}$, $\mathbf{F}_L = (\Phi_0/c)\mathbf{J}\times\mathbf{n}$, (see figure 2.7). The vortices start to move because the Lorentz force causes a finite electrical field proportional to the velocity, $\mathbf{E} = \mathbf{B}\times\mathbf{v}/c$, in which it is perpendicular to the velocity and parallel to the electrical current leading to the dissipation of energy and to a finite flux-flow resistivity. In order to have current without loss, the vortices must be held stationary, or "pinned". Imperfections in the superconductor act as pinning centers and retard the motion of the vortices with a volume flux pinning force $\mathbf{F}_P$. The condition $\mathbf{F}_L = \mathbf{F}_P$ defines

where the vortices become depinned and move across the sample, generating a voltage, which in turn leads to an energy loss. Thus, the first voltage encountered in a J_c measurement is that of the fluxon motion and not that of the superconductor changing to the normal, resistive state. The field at which $\mathbf{F}_P = 0$ is $\mathbf{H}_{irr}$ (the irreversibility field), and no bulk supercurrent can flow above this field. The condition $\mathbf{F}_P = 0$ thus defines the technologically relevant maximum magnetic field. (Alexandrov, 2003; Kwok et al., 2016; Thinkham, 1996).

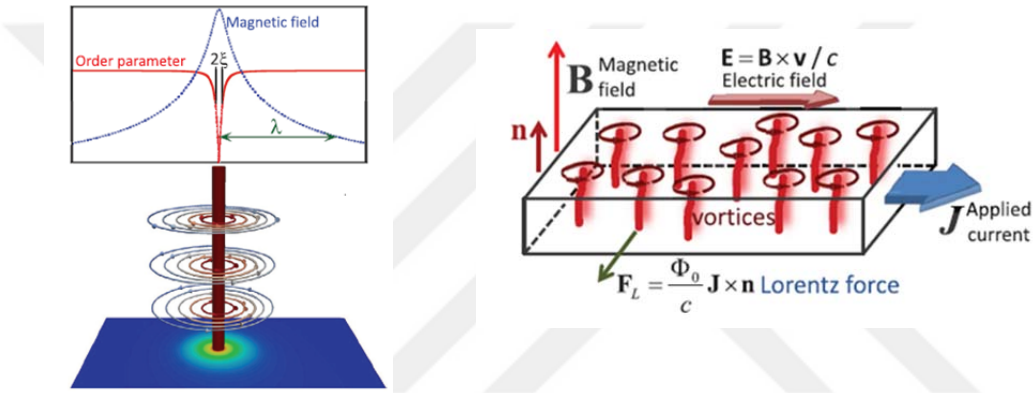

Figure 2.7. Structure of an vortex, and diagram of the dissipation caused by moving vortices in uniform superconductors (Kwok et al., 2016).

2.2.4. Critical Current

Apart from the two limiting parameters T_c and $\mathbf{H}_{c2}$, which are instinct characteristics of a superconducting material, a superconducting state can be destroyed if a material carries a direct current higher than a critical value I_c. Thus, any superconductor is characterized by a critical current density J_c (a current in the cross-sectional area through which it flows), which is the maximum current that can protect a superconductor. The three critical parameters are interdependent: $T_c(\mathbf{H}, J)$, $\mathbf{H}_c(T, J)$, and $J_c(T, \mathbf{H})$, as shown in Figure 2.8. Superconductivity only exists in the space under the dome (*3D* surface) in the figure. The value of J_c can be obtained in one of two ways, either as a proportion of voltage to current (*V-I*) or as

a proportion of magnetization to field (**M**–**H**) (Dew-Hughes, 2001; Chaddah, 2003).

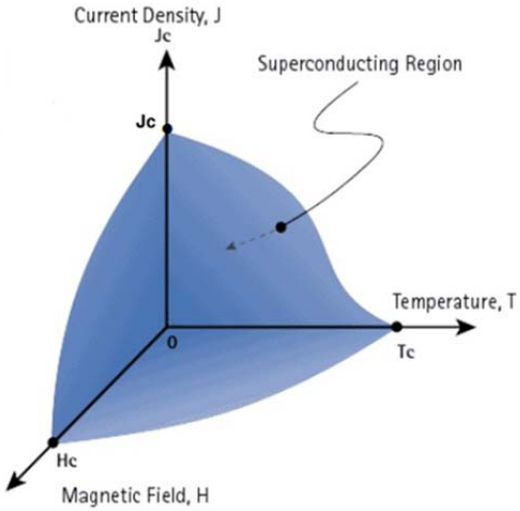

Figure 2.8. Interdependent critical parameters of a superconductor (www.slideshare.net).

2.3. Development of Fe(Se,Te) Superconducting Crystal and Wire

McQueen et al. (2009) reported the production of *β*-FeSe polycrystal to investigate the effect of excess iron on the superconducting properties. The authors prepared the FeSe by using solid state method with various the annealed temperatures. They found that the superconductivity properties of $Fe_{1+x}Se$ are degrade with increasing of excess iron. As a shown in Figure 2.9, the T_c value decrease from 8.5 to 0.6 K for δ = 0.01 and 0.03, respectively, although the crystal structure does not change for the samples. The result confirmed that the superconductivity in FeSe is absolutely sensitive to composition and preparation conditions.

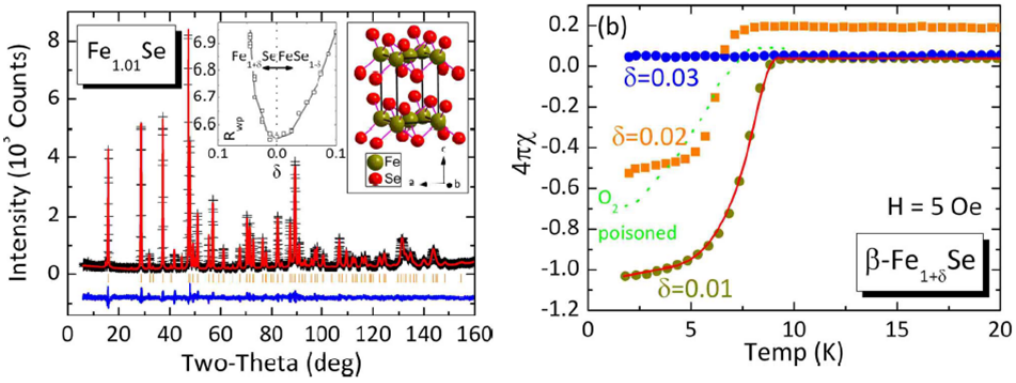

Figure 2.9. Rietveld refinement NPD of the $Fe_{1.01}Se$ at room temperature; Magnetization versus temperature (McQueen et al., 2009).

Zargar et al. (2014) synthesized FeTe and $FeSe_{0.5}Te_{0.5}$ polycrystals by using the solid state method to explore the structural, electrical and magnetic properties. According to the XRD, the reflection peaks are well indexed tetragonal stucture for both samples. The critical temperature, T_c^{onset} and T_c^{offset} of the $FeSe_{0.5}Te_{0.5}$ sample is shifted to 13 and 11 K at 0 T, respectively. However, the FeTe is nonsuperconductor and an anormaly is observed at 78 K, which correspond to a structural transition from tetragonal to orthorhombic.

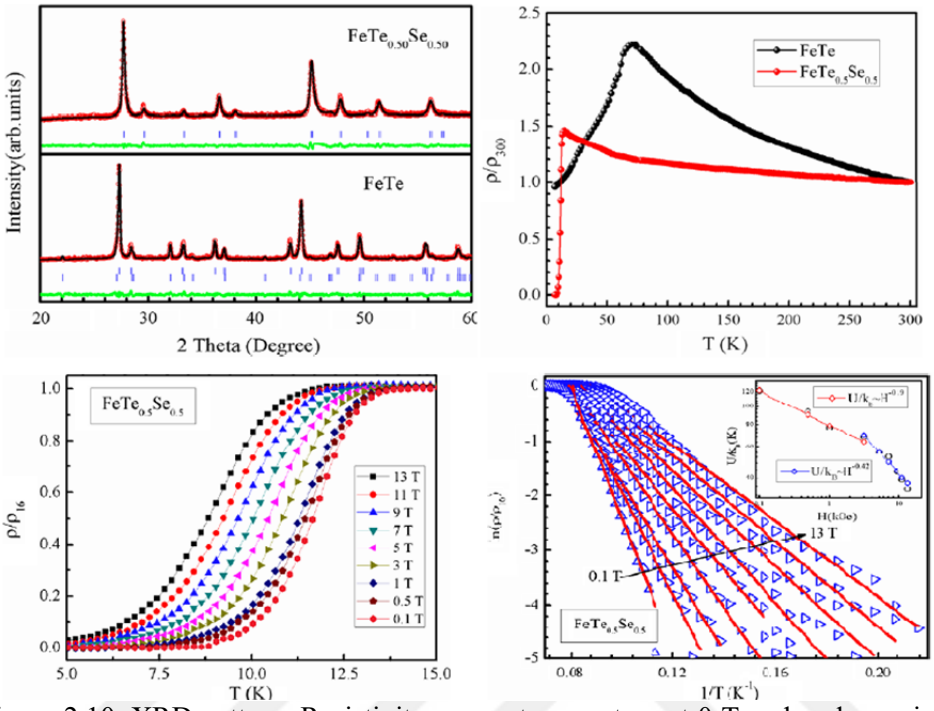

Figure 2.10. XRD pattern; Resistivity versus temperature at 0 T and under various magnetic fields, $\ln(\rho/\rho_0)$ versus $1/T$ inset: U_0/k_B versus magnetic fields, respectively (Zargar et al., 2014).

According to the temperature dependences of magnetoresistance (MR), the transition drops to lower temperatures accompanied by a increase in the transition width with increasing magnetic field. To investigate flux dynamic of $FeSe_{0.5}Te_{0.5}$ sample, the TAFF theory was used and $\ln(\rho/\rho_0)$ versus $1/T$ graph obtained for calculating of U_0/k_B (in Figure 2.10). The authors argued that the U_0/k_B decreased with increasing magnetic fields by reason of weaker inter granular coupling and vortices motions.

Yadav et al. (2009) worked on $FeSe_{0.4}Te_{0.6}$ single crystal to investigate physical properties. The XRD figure showed that the reflection peaks are well indexed tetragonal stucture as confirmed by the TEM analysis. The superconducting onset temperature found at 15.3 K at 0 T. The authors estimated that the $\mathbf{H_{c2}}$ (0 K) for T_c^{onset}, T_c^{mid} and T_c^{offset} were 184, 88 and 69 T from the linear

extrapolations. By using the Werthamer–Helfand–Hohenberg (WHH) theory, the value of $\mathbf{H_{c2}}$ at T = 0 K were 126, 65 and 51 T for three superconducting temperature, respectively. They found that the single crystal had highly anisotropy from the $\mathbf{H_{c1}}$ which was calculated in the ab and c directions of the crystals.

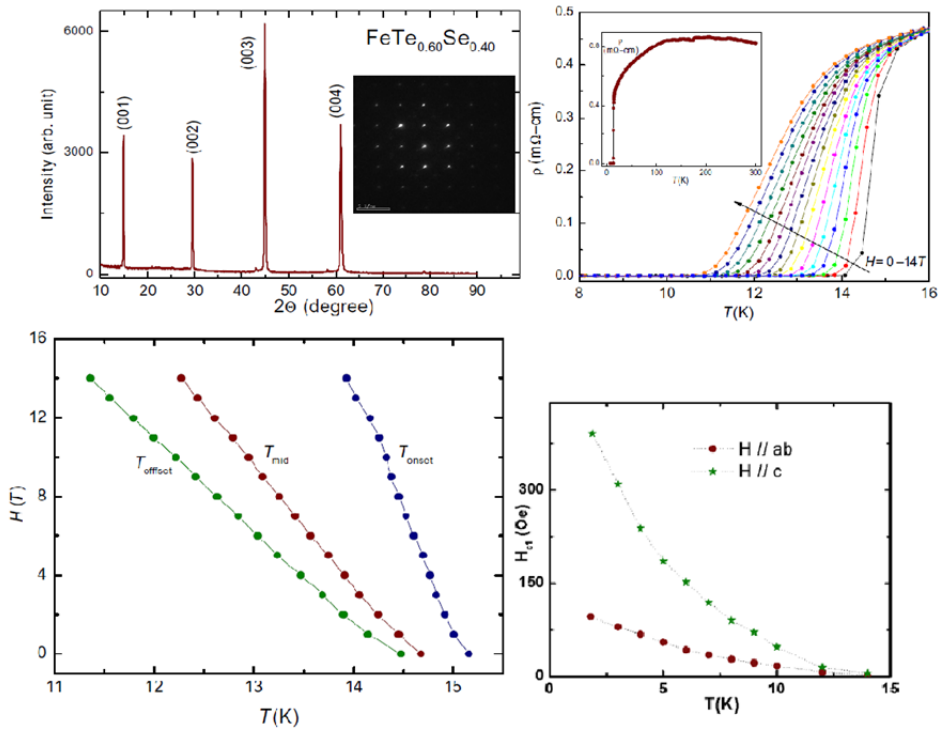

Figure 2.11. XRD pattern, inset: TEM image; resistivity versus temperature; phase diagram of the $\mathbf{\mu_0 H_{c2}}$; the $\mathbf{H_{c1}}$ for **H** ∥ ab and **H** ∥ c, respectively (Yadav et al., 2009).

Sun et al. (2014) investigated the annealing effect on the $Fe_{1+x}Se_{0.4}Te_{0.6}$ single crystal. The authors found that the O_2–, S–, Se– and Te–annealed samples showed a definitive trace of superconductivity, whereas the as-grown sample exhibited no bulk superconductivity. After that, J_c had been calculated — from the **M–H** measurement under self–field — to be 2–4x10^{-5} Acm^{-2} for all samples.

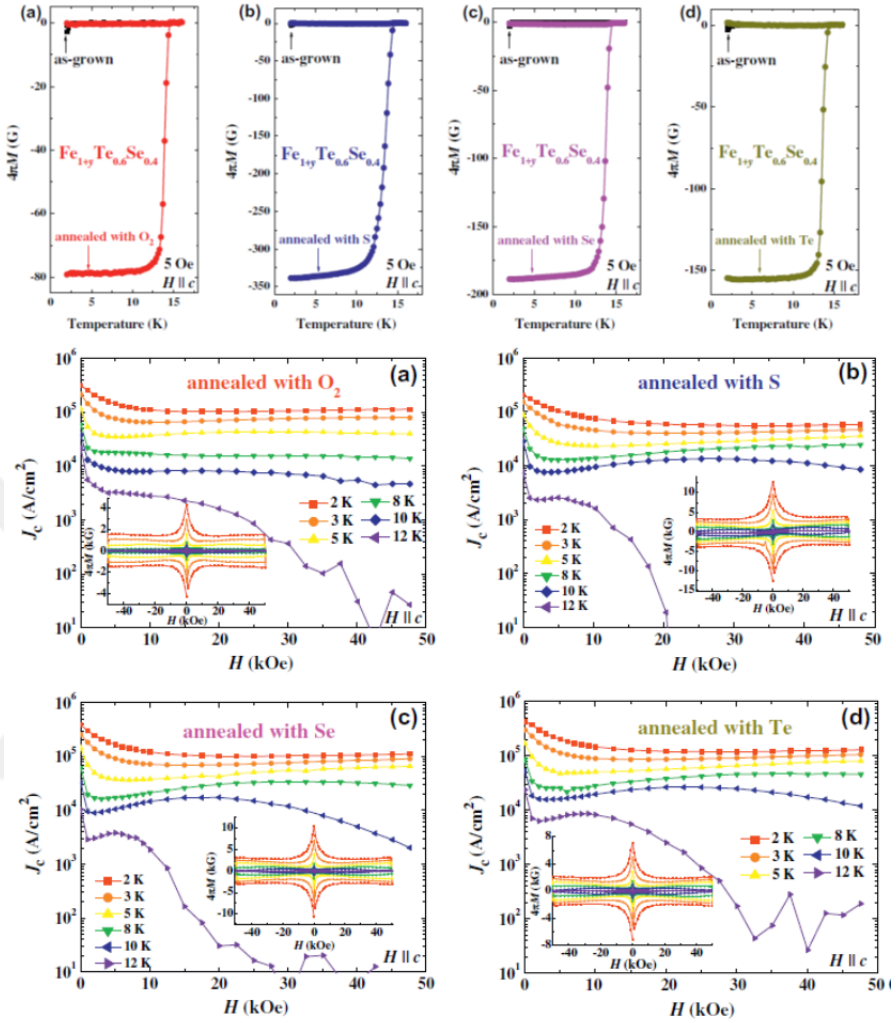

Figure 2.12. Magnetization versus temperature, and **M–H** loops for the as-grown and the annealed samples (Sun et al., 2014).

In 2009, Mizuguchi et al. reported the production of the first 11 type compound wire. They synthesized Fe(Se,Te) wire by using *in-situ* PIT with a pure iron tube. *in-situ* PIT process, a metal tube is filled with raw material and the reaction takes place within the wire and/or tape. If the tube employed is made of Fe, it serves as both sheath and raw metarial for the production of FeSe-11 superconductor wire or tape. In order to fabricate Fe(Se,Te) wire, firstly, SeTe

precursor was synthesized. Then an iron tube was filled with the precursor for obtaining a wire and/or tape. After that, the flat tape — whose thickness and width were 0.55 mm and 4.3 mm, respectively — was annealed quickly by heating to 500°C for 2 h. According to the elemental mapping images (in figure 2.13), the tube supplied iron homogeneously to the superconducting phases.

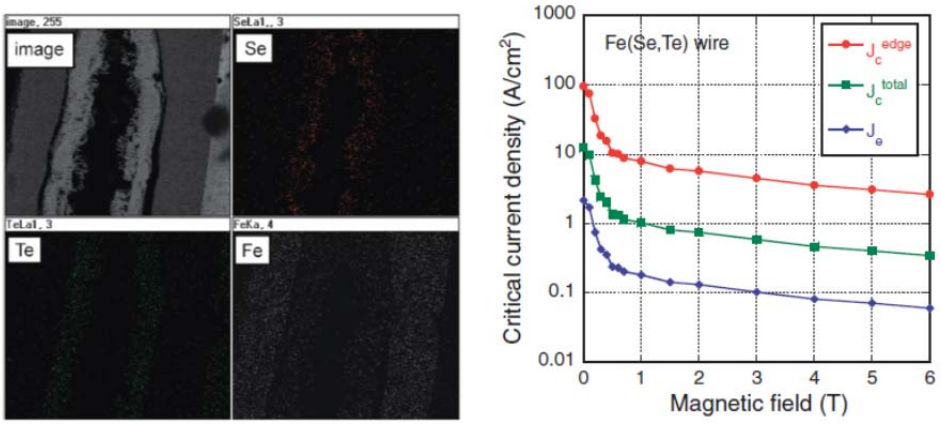

Figure 2.13. SEM image and EDX map images of the wire; Magnetic field dependencies of critical current density of wire (Mizuguchi et al., 2009).

However, the pores appeared both at the center of the cross section and at the boundary. The authors explained that these pores came from the evaporation of chalcogen from inside the wire during the heating process. The J_e (entire area of the cross section of the wire), J_{ctotal} (the total area of the superconducting phases), and J_{cedge} (the edge area where the sheath and the superconducting phases are well connected) had been estimated — from the *I–V* measurement at 4.2 K — to be 2.2, 12.4, and 94.6 A/cm^2 under self-field, respectively. The J_c value also decreased rapidly in direct proportion to the increase of the magnetic field.

Ozaki et al. (2011) fabricated $FeTe_{0.5}Se_{0.5}$ wire by using *ex-situ* PIT method with a pure iron tube. In this process, the metal tube is filled with synthesized material, then the wire/tape is rolled and drawn. Firstly, the authors

prepared a polycrystalline form of $FeTe_{0.5}Se_{0.5}$ as a precursor, and then it packed into a pure iron tube. Then, round wires, approximately 1.1 mm in diameter, were obtained and were heated at 150–500° for 2 h. In this case, the wire showed uniform deformation of composition, as a shown in Figure 2.14. After the different heating processes, the highest T_c^{offset} and ΔT were obtained as 9.1 K and 1.7 K, respectively, at 200°C for 2h.

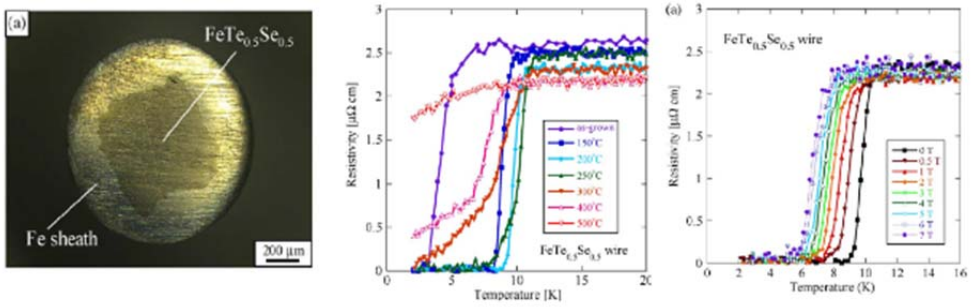

Figure 2.14. **(a)** The cross section of wire after heat treatment; **(b)** Temperature versus resistivity for superconducting wires for different annealing temperatures; **(c)** Temperature versus resistivity for wires annealed at 200^0C for 2 h under different magnetic field (Ozaki et al., 2011).

The transport J_c value of this wire was calculated to be 64.1 A/cm^2 at 4.2 K. However, with an increased annealing temperature of Fe(Se,Te) above 250°C, the superconducting phase of the wires decreased until 400°C was reached, at which point it disappeared.

Palombo et al. (2015) fabricated Fe(Se,Te) wire using the *ex-situ* PIT method. In this paper, firstly the authors investigated which metalic sheath was suitable for producing Fe(Se,Te) superconducting wires. For the first step, the $FeSe_{0.5}Te_{0.5}$ precursor was poured into 8 different sheaths (Cu, Ag, Nb, Ta, Ni, Fe, cupronickel 90–10, and brass). After obtaining the wires, they carried out the heat treatment at temperatures ranging from 700°C to 850°C, then reported the effects induced on the superconducting phase by the sheath. As shown in Figure 2.15 (a) and (b), both Ag and Cu diffused up to the middle of the wire, causing compounds

with Fe, Se, and Te, and damaging large amounts of precursor. For a Ni-sheathed tape, the nickel subtracted iron from the Fe(Se,Te) phase, so the Fe-Ni spots were easily recognizable, as shown in Fig. 2.15 (c). After heat treatment of a Nb-sheathed wire, the niobium consisted of two interface reaction layers between the sheath and the compound; the first was a Fe-rich niobium alloy nearest to sheath, while the second was a Se-rich layer which also included both tellurium and iron, as shown in Figure 2.15 (d). After heat process of a cupronickel 90–10-sheathed wire with tantalum barrier, tantalum was used for an interface layer between sheath and precursor polluting it. However, cupronickel diffused up to the middle of wire, had large degrading effect on the compound; similar to nickel, as shown in Figure 2.15 (e). Finally for a brass-sheathed wire, compound appeared as wholly copper polluted. In conclusion, the tested metal sheaths which are commonly used in superconducting wire fabrication, the Fe(Se,Te) compound reacted all of the metal sheath. So an iron is the only suitable tube for production of 11-type superconducting wires because compound include an iron element, as well.

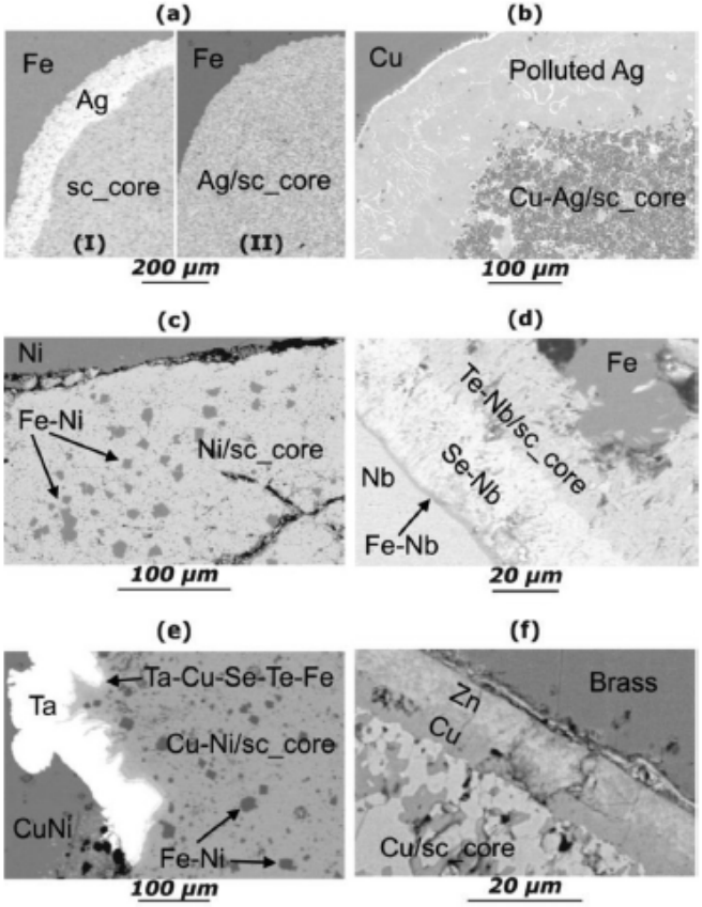

Figure 2.15. SEM image of wires: **(a)** Fe sheathed wire with Ag barrier before (I) and after (II) the heat procedure **(b)** Cu-sheathed wire with Ag barrier; **(c)** Ni-sheathed tape; **(d)** Nb-sheathed wire; **(e)** cupronickel 90-10-sheathed wire with Ta barrier; **(f)** brass-sheathed wire (Palombo et al., 2015).

After determining the iron sheath to be best, they used it to produced Fe(Se,Te) superconducting wires. Palombo, et al. were geared towards the fabrication of the $Fe_{1-y}Se_xTe_{1-x}$ percursor with different starting compositions. The produced compounds were $FeSe_{0.5}Te_{0.5}$, $Fe_{0.95}Se_{0.60}Te_{0.40}$, $Fe_{0.95}Se_{0.65}Te_{0.35}$, $Fe_{0.90}Se_{0.65}Te_{0.35}$ which labelled as A, B, C, D, respectively. Then a pure iron tube was filled with it for wires. Afterward, the wires sealed into an evacuated quartz

tube, and annealed both at 800°C and at 850°C, respectively for each wires. All of the wires showed almost the same transition temperature at ~ 8–9 K. However, zero resistivity was found for B, C, and D wires, both heating process. The best results were observed for the C melted wire, for which the T_c^{onset} and T_c^{offset} are at 9.3 and 8 K, respectively. The critical current had been evaluated in all the melted wires from *I-V* measurement. They calculated J_c value as 12 A/cm^2, 50 A/cm^2, 100 A/cm^2 and 80 A/cm^2 for A, B, C, and D, for all the melted wires, respectively.

Mizuguchi et al. (2011) prepared single- and three-core wire of $FeSe_{1+d}$ by using a chemical-transformation PIT method. This process defined as an intermediate method between *in-situ* and *ex-situ* which is tranformation of inside of wire from hexagonal to tetragonal by heating and a tube which is made of Fe, it serves as raw metarial for the fabrication of $FeSe_{1+d}$ superconductor wire and/or tape. It involved two heating process. Firstly a hexagonal phase of precursor was prepared, and then a Fe tube was filled with it for wires. Secondly, the wires were heated for hexagonal phase transformation into tetragonal phase to increase packing density, decrease excess iron and improve connection between sheath and superconducting core. After the wire obtained, the single- and three-core wires annealed at 1000°C for 5 h. According to XRD, the $FeSe_{1.2}$ precursor has a hexagonal structure. However, after the annealing of wire, the crystal structure changed into the tetragonal structure, expect for some peaks of pure Fe, as given Figure 2.16. The T_c^{offset} and $\mathbf{H_{c2}}$ were obtained to be ∼10 K and 19.3 T, respectively. The J_c value calculated as 218 A/cm^2 for single-core wire, 588 A/cm^2 for three-core wire at 4.2 K and at 0 T. The J_c of the three-core wire was larger than single-core wire, it indicated that multi-core production was effective to obtain a high J_c 11-type wire.

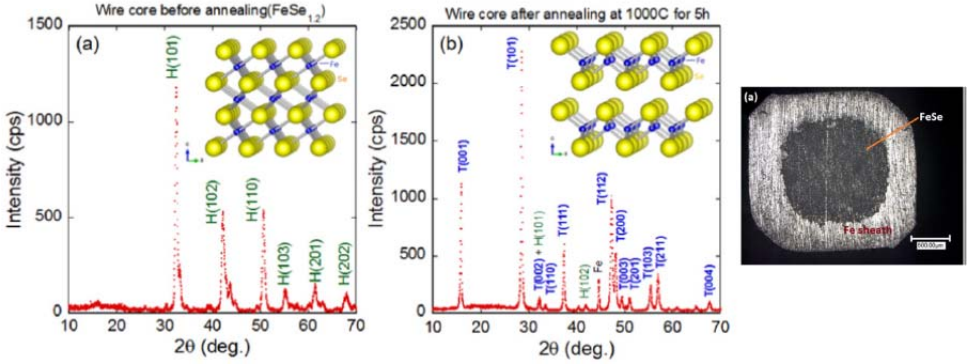

Figure 2.16. **(a)** X-ray diffraction for the precursor; **(b)** X-ray diffraction after annealing for the single-core wire; **(c)** The cross- section for the single-core wire (Mizuguchi et al., 2011).

Izawa et al. (2014) produced $FeTe_{0.4}Se_{0.6}$ tape by using the chemical-transformation PIT method. At first, precursor of $Fe(Te_{0.4}Se_{0.6})_{1.4}$ was synthesized and then a Fe tube was filled with it for wires. Afterward, the tapes annealed at 400–600°C for 1–3 h and at 200°C for 2–5 h, respectively. As a seen in Figure 2.17, the hexagonal crystal structure of precursor changed into the tetragonal structure by applying heating process of tapes via a provide of iron from the iron tube into the precursor, depending on annealing temperature and/or time. From **M**-*T* measurement under the ZFC and FC mode (Figure 2.17), the superconducting transition temperature of tapes were observed at 7 K for 400°C, 11 K for 500°C, 12.5 K for 550°C and 13.5 K 550°C. Although the tape which was annealed at 600°C exhibited only tetragonal phase, superconductivity did not occurred bulk superconductivity because of the much excess Fe in the superconducting phase. Morever, the authors studied different annealing temperature at 525°C 3 h, 525°C 3 h + 200°C 2 h and 525°C 3 h + 200°C 5 h, as well. The transition temperature at 13, 13.5 and 13 K were observed, respectively. Then, authors decided to investigate the tape which was annealed at 525°C 3 h + 200°C 2 h which had high T_c. They obtained the magnetic J_c as 3.10^3 Acm^{-2} at 4.2 K and 0 T. And the $\mu_0\mathbf{H}_{irr}$ at 4.2 was estimated to be 7 T.

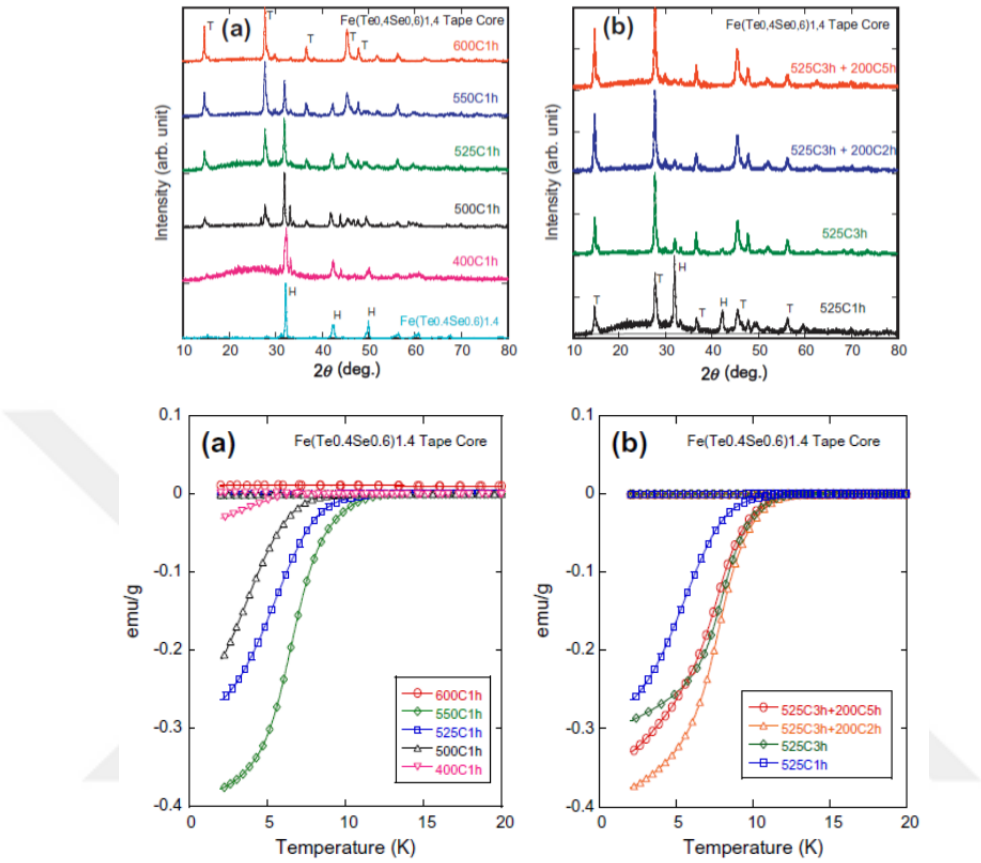

Figure 2.17. XRD patterns for the precursor and annealed tape at variation annealing temperature Below; magnetization against temperature for the tapes at variation annealing temperature (Izawa et al., 2014).

Guo et al., fabricated FeSe superconducting wire by using a gas diffusion prosedure which was widely used for fabrication of superconducting wires such as Nb_3Sn (Dew-Hughes, 1975), MgB_2 (Canfield et al., 2001), and so on. In their study, Se powder and pure iron wires and/or tapes were employed as a precursor, respectively. And then it sealed into a iron tube for heating process which ranging between 400 and 800°C. To investigate of supercondunducting properties of FeSe layer separated from the iron tapes. From XRD, polycrystalline FeSe obtained the tetragonal structure with a trace of impurity phase, given in Figure 2.18. From *V-I*

measurement, the J_c vaule calculated approximately 137 A/cm^2 at 4 K with self-field for FeSe superconducting wire. Using the gas diffusion procedure, the value of J_c is much higher than the previous reports by Mizuguchi et al., (2009) and Ozaki et al., (2011). The results propose that the diffusion procedure is improving the quality of FeSe wires.

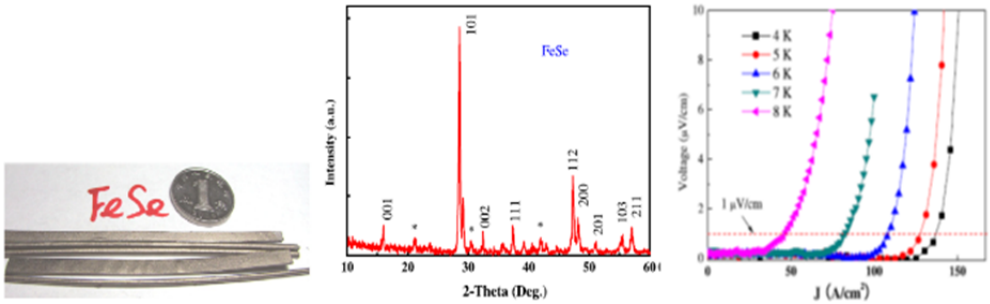

Figure 2.18. **(a)** FeSe wires and tapes; **(b)** XRD pattern of the tape; **(c)** *I–V* characteristics at indicated temperatures for the FeSe tape (Guo et al., 2011).

Ozaki et al. (2011) produced single- and seven-core wires of $FeSe_xTe_{1-x}$ using *in-situ* PIT method with an iron tube. In order to enhance J_c value of the $FeSe_xTe_{1-x}$ superconducting wires were annealed the higher temperature which is commonly employed for the fabrication of polycrystalline bulk samples of $FeSe_xTe_{1-x}$. SEM image and the EDX map image showed that the reacted layer was composed of two layers (in Figure 2.19). The first layer was FeSe where Se was distributed close to the Fe sheath, and the second layer was FeTe where Te became richly near the center of the iron sheath for the single-core wire. The J_c values calculated approximately 226.2 A/cm^2 for mono- and 100.3 A/cm^2 seven-core wire at 4.2 K. Also, they estimated $\mu_0 H_{c2}$ and $\mu_0 H_{irr}$ as ~ 27 T and ~ 22 T, respectively.

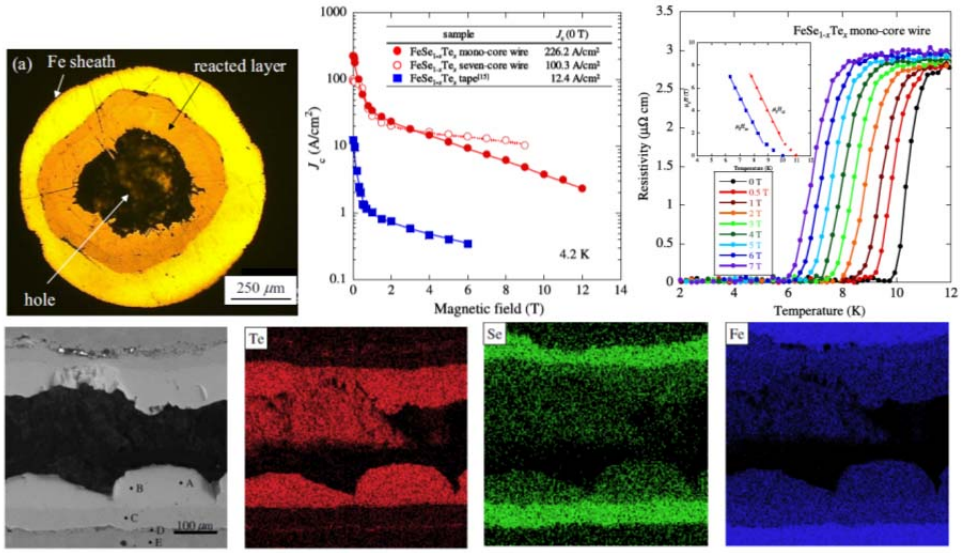

Figure 2.19. **(a)** Optical micrographs for single-core wire; **(b)** Magnetic field versus the transport J_c for both wires; **(c)** Temperature versus resistivity for single-core wire under different magnetic fields up, inset: $\mu_0 H_{c2}$ and $\mu_0 H_{irr}$ diagram; **(d)** SEM image and EDX map images for the single-core wire (Ozaki et al., 2011).

Ding et al., (2012) fabricated FeSe tapes by using the diffusion method. In order to enhance the performance of FeSe tapes, they focused on the optimizing parameters: the reaction temperature and the thickness. The proper amount of Se and Fe tape were sealed in an quartz tupe, heated between 600 and 800°C and held for 12 h at each temperature. The diffraction peaks were well indexed with the tetragonal structure for the annealed at 800°C with a thickness 50 μm and 25μm, shown in Figure 2.20a. From the optical image, the thin tape (25 μm) indicated that the surface had a wavy structure which degraded the performances of the tape. However, the surface of thick tape is much smoother than the thinner one, so that was selected for investigating superconducting properties. The J_c calculated as 600 A/cm^2 at 4.2 K without magnetic field. This value is larger than the previous reported by Muziguchi et al. (2009) and Ozaki et al. (2011). The $\mathbf{H_{c2}}$ was calculated as 243 kOe from the WHH formula.

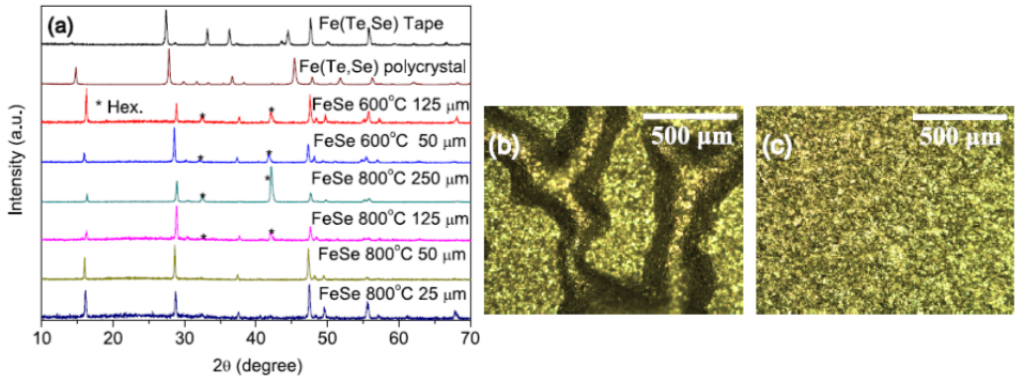

Figure 2.20. **(a)** XRD pattern of tapes; **(b)** Images of FeSe tapes with thicknesses 25μm; **(c)** for 50 μm (Ding et al., 2012).

Ozaki et al. (2011) fabrication of single- and seven-core FeSe wires by using *in-situ* PIT method. In order to fabricate wire, Se was put into an iron tube for obtaining a wire. After that, the wire — whose diameter 1.1 mm — was annealed. As seen in Figure 2.21., the elemental mapping analysis confirmed that the distribution of Fe and Se was almost homogeneous in the reacted layer. According to the XRD figure, the reflection peaks were very sharp and had the tetragonal structure with a trace of impurtiy peaks, which were recognized as iron-oxide and hexagonal phase. The transport J_c was obtained as ~350 A/cm^2 for single- and ~1027 A/cm^2 for seven-core wire at 4.2 K. Also, the $\mu_0\mathbf{H_{c2}}$ and $\boldsymbol{\mu_0 H_{irr}}$ value were estimated approximately 32 T and 23 T by linear extrapolation, respectively.

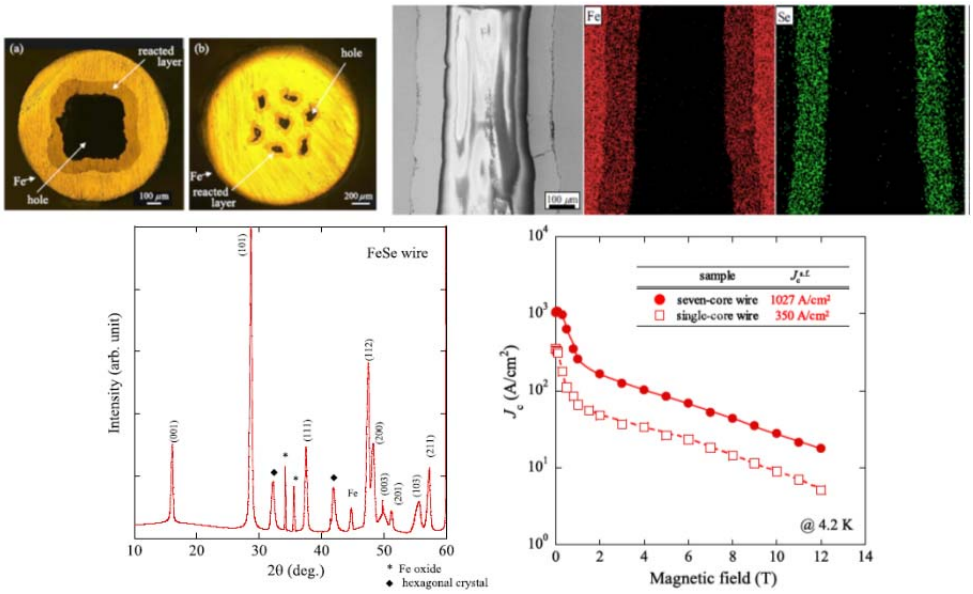

Figure 2.21. **(a)** The cross section of single- and seven-core wires; **(b)** SEM image and EDX map images for the single-core wire **(c)** XRD pattern for wire; **(d)** Magnetic field versus J_c for single- and seven-core wires (Ozaki et al., 2011).

3. EXPERIMENTAL PROCEDURES

3.1. Synthesis

3.1.1. The Production of the $FeSe_{0.5}Te_{0.5}$ Single Crystals

Single crystals of $FeSe_{0.5}Te_{0.5}$ were syhthesized by using self-flux method. The granular of Fe(99.99%) and the shot of Se (99.999%) and Te (99.999%) were put into a quartz tube with molar ratio of $FeTe_{0.5}Se_{0.5}$ (Fe:Te:Se = 1:0.5:0.5) and sealed under high vacuum. The quartz tube was placed a second quartz tube to avoid the cracking of tube during the heating process. First, two samples were heated to 1050°C and held for 24 h at that temperature. Then, they were cooled to 700°C at two different rates, one sample at 1.45°C/h and the other at 5.83°C/h.

3.1.2. The Production of the $Fe_{1+d}Se_{0.4}Te_{0.6}$ Polycrystal

Polycrystal of $Fe_{1+d}Se_{0.4}Te_{0.6}$ (d=0%, 5%, 10%) were fabricated by using solid state method in order to investigate the effect of Sulfur annealing in the various amount of excess iron. The nominal composition of $Fe_{1+d}Se_{0.4}Te_{0.6}$ (d=0%, 5%, 10%) packed into a quartz tube. Then, they sealed under high vacuum for heating procedure. Firstly, they were heated to 680°C and held for 10h at that temperature. After that period, the obtained mixture was ground and pelletized into separate pellets with a weight of 0.1 g each. The pellets were sealed under high vacuum. The heating was performed at 700°C for 10 h. For sulfur annealing, the pellets were placed the quartz tube with 1.015 g sulfur grains. Following the sealing, they were annealed at 300°C for 3 h.

3.1.3. The Production of the Ag Doped $FeSe_{0.94}$ Polycrystals

Polycrstal $FeSe_{0.94}$ with 4 wt % Ag were prepared by melting process. The powder of Fe (99.99%), the grain of Se (99.999%) and the powder Ag (99.999%) with molar ratio of $FeSe_{0.94}$ and 4 wt % Ag (Fe : Se : Ag = 1 : 0.94 : 0.001) was mixed, ground and pelletized in a glove box with Ar atmosphere. The pellets were

put into a quartz tube and sealed under the high vacuum. First, the quartz tube was heated to 700°C for 20 h. After it was furnace cooled down to room temperature and the mixture was reground and repelletized. The pellets were sealed into evacuated the quartz tube. Before the second heating process, the quartz tube was put into a second quartz tube to prevent the cracking during the second heating process. The double quartz tube was heated up to 1050°C and kept at that temperature for 20 h. For annealing, the mixture was regound, repelletized in the glove box. The pellet sealed and put into the furnace at 400°C for 100 h. Then it was furnace cooled down to room temperature.

3.1.4. Powder-In-Tube Method

The Powder-in-tube (PIT) method is an most popular tecnique for manufacturing many superconductors, including Nb_3Sn, MgB_2, the copper-based superconductors, and the iron-based superconductors wires. The PIT process is very beneficial because of low costs and relatively simple formation techniques. Moreover, it is the only way of producing multi filamentary wires and tapes. PIT wires are made by filling a powder into a tube, drawing the tube through a set of dies into a wire, and then applying a heat treatment to transforming the powder into a superconductor. The advantage of heat treatment of PIT; enhances fill factor by densification and lead to oxidation in the superconducting core which later acts as pinning centers (Ma, 2012; Seidel, 2015).

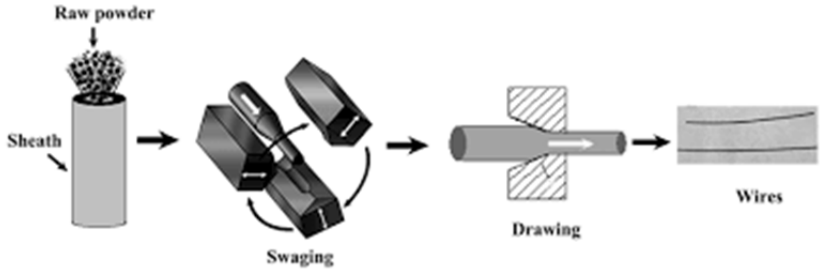

Figure 3.1. Schematic representation of Powder In Tube Method (Ma et al., 2009).

The basic PIT technique is classifed into two different processes: *in–situ*, in which a metal tube is filled with raw material and the reaction is performed within the wire and/or tape, and *ex–situ*, in which the metal tube is filled with synthesized material then the wire/tape is rolled and drawn, as shown in Figure 3.2.

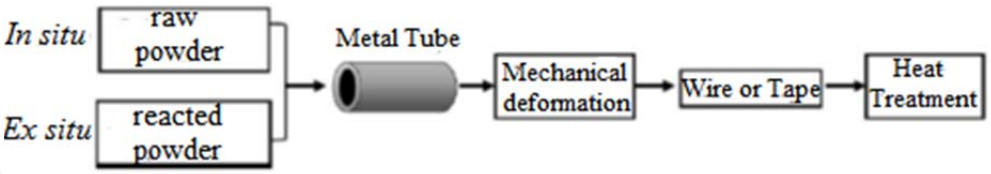

Figure 3.2. Powder-in-tube (PIT) process: used for fabricating wire. *in–situ* and *ex–situ* processing (Ma, 2012).

3.1.4.1. The Production of the Fe(Te,Se) Wire

Fe(Te,Se) wire was fabricated using the *in–situ* PIT with an iron tube. In the *in-situ*, the tube employed was made of Fe, it served as both sheath and raw metarial for the production of Fe(Se,Te) superconductor wire. So, the powder Se and Te with nominal composition of 1:1 was packed into a pure Fe tube whose outer and inner diameters were 6 mm and 3.2 mm, respectively (Fig. 3.4). Firstly, the tube was rolled into a round rod of 2 mm in diameter using groove rolling, and then, drawing into a wire of 1 mm in diameter using wire drawing die. For heating procedure, the wire was cut into pieces of 4 cm in length and sealed into evacuated a quartz tube for heating process, as given in Table 3.1.

Table 3.1. The heating condition of the Fe(Se,Te) wire.

Sample name	Temperature (°C)	Time (hour)	Taken out style from furnace
1	850	2	Furnace cooling
2	700	2	Furnace cooling

3.1.4.2. The Production of the $Fe(Se_{0.7}Te_{0.3})_{1.5}$ Wire

$Fe(Se_{0.7}Te_{0.3})_{1.5}$ wire was fabricated using the *ex–situ* PIT method with an iron tube, in which the metal tube is filled with synthesized material then the wire is rolled and drawn. The nominal composition $Fe(Se_{0.7}Te_{0.3})_{1.5}$ was synthesized by the solid-state reaction. They were mixed, grounded and pressed into pellets in a glove box with Ar atmosphere. The pellets were put into a quartz tube and sealed under the high vacuum for heating process. First, the quartz tube was heated to 650°C for 10 h, and then, cooling down to room temperature. After that, the obtained mixture was reground and repelletized. The pellets were put into the quartz tube for sealing under high vacuum, then, heating at the same condition of the first step (at 650°C for 10 h). After a new grinding, it was packed into an pure iron tube — whose outer and inner diameters were 6 mm and 3.2 mm, respectively — in the glove box with Ar atmosphere. After that, the wire was rolled and drawn, and then, cutting into pieces of 4 cm in length. The wires were put into a quartz tube and sealed under the high vacuum for heating process which is given in Table 3.2.

Table 3.2. The heating condition of the $Fe(Se_{0.7}Te_{0.3})_{1.5}$ wire.

Sample name	Temperature (°C)	Time (hour)	Taken out style from furnace
1	800	5	Furnace cooling
2	800	5/12	Quench

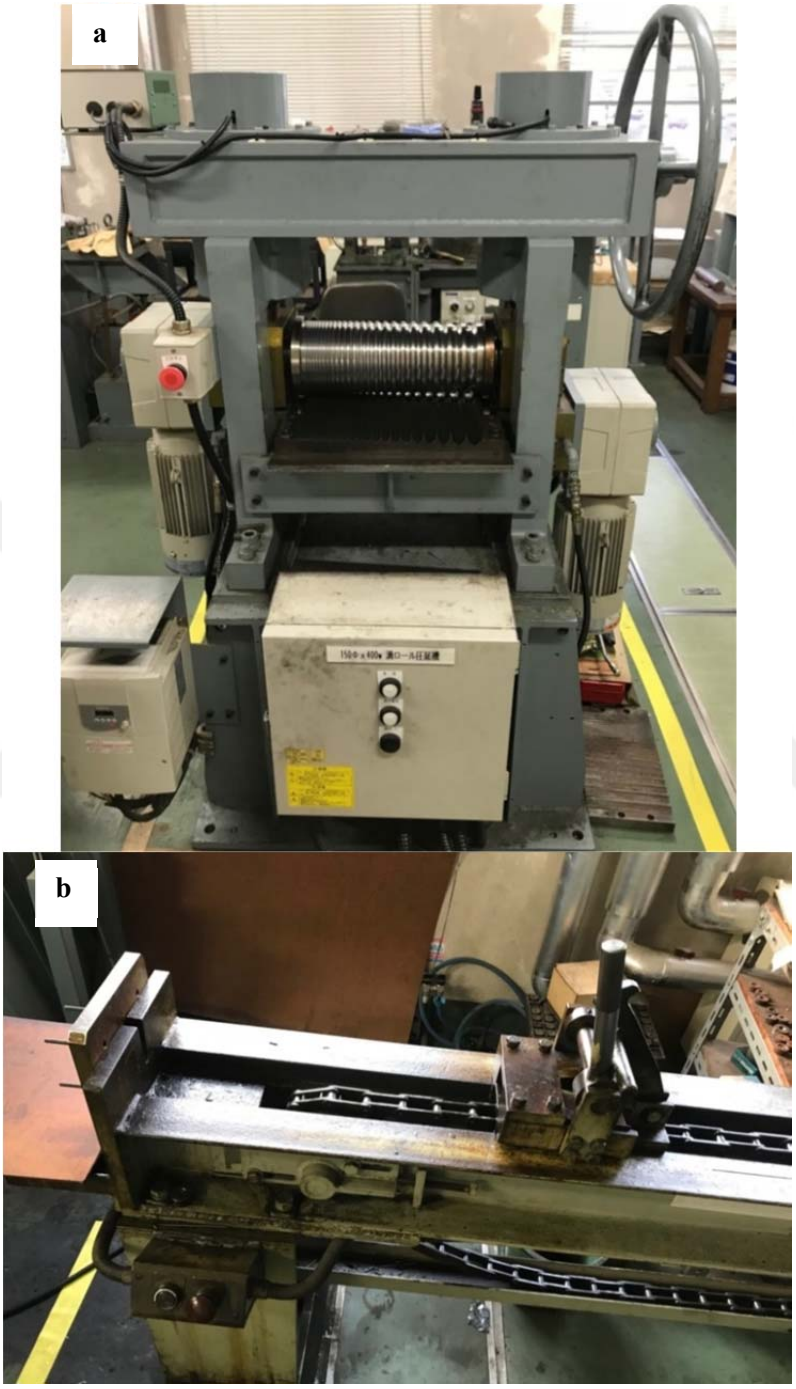

Figure 3.3. **(a)** The picture of rolling machine; **(b)** drawing machine (NIMS, Japan).

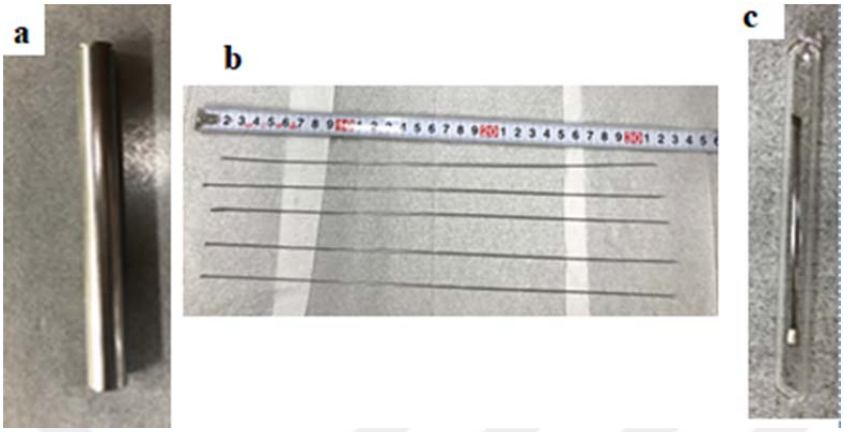

Figure 3.4. **(a)** The iron tube filled with precursor, afterwards it was sealed with pure iron caps; **(b)** The obtained Fe(Se,Te) wires after being rolled and drawn; **(c)** a pieces of wire put into an quartz tube, then sealed under high vacuum for heating process.

3.1.4.3. The Production of the Ag Doped $FeSe_{0.94}$ Wire

The Ag doped $FeSe_{0.94}$ wire was produced using the *ex–situ* PIT method with an iron tube. The precursor $FeSe_{0.94}$ with 4 wt % Ag were prepared by melting process. The powder of Fe (99.99%), the grain of Se (99.999%) and the powder Ag (99.999%) with molar ratio of $FeSe_{0.94}$ and 4 wt % Ag (Fe : Se : Ag = 1 : 0.94 : 0.001) was mixed, grounded and pressed into pellets in a glove box with Ar atmosphere. The pellets were put into and sealed into evacuated a quartz tube for two heating process. Firstly, the heating was performed to 700°C for 20 h. After the first heating step, the mixture was reground, repelletized and the pellets were sealed into evacuated the quartz tube. After that, it was placed in a second quartz tube, and then, heated to 1050°C and held for 20 h at that temperature. After it was a new grinding, a pure Fe tube tube — whose outer and inner diameters were 6 mm and 3.2 mm, respectively — was filled with synthesized material in the glove box with Ar atmosphere. Then, the wire was rolled and drawn to obtain round wires of 1 mm in diameter. The wire were put into a quartz tube and sealed under the high vacuum for heating process, as given in Table 3.3.

Table 3.3. The heating condition of the Ag doped $FeSe_{0.94}$ wire.

Sample name	Temperature (°C)	Time (hour)	Taken out style from furnace
1	400	100	Furnace cooling
2	400	100	Quench

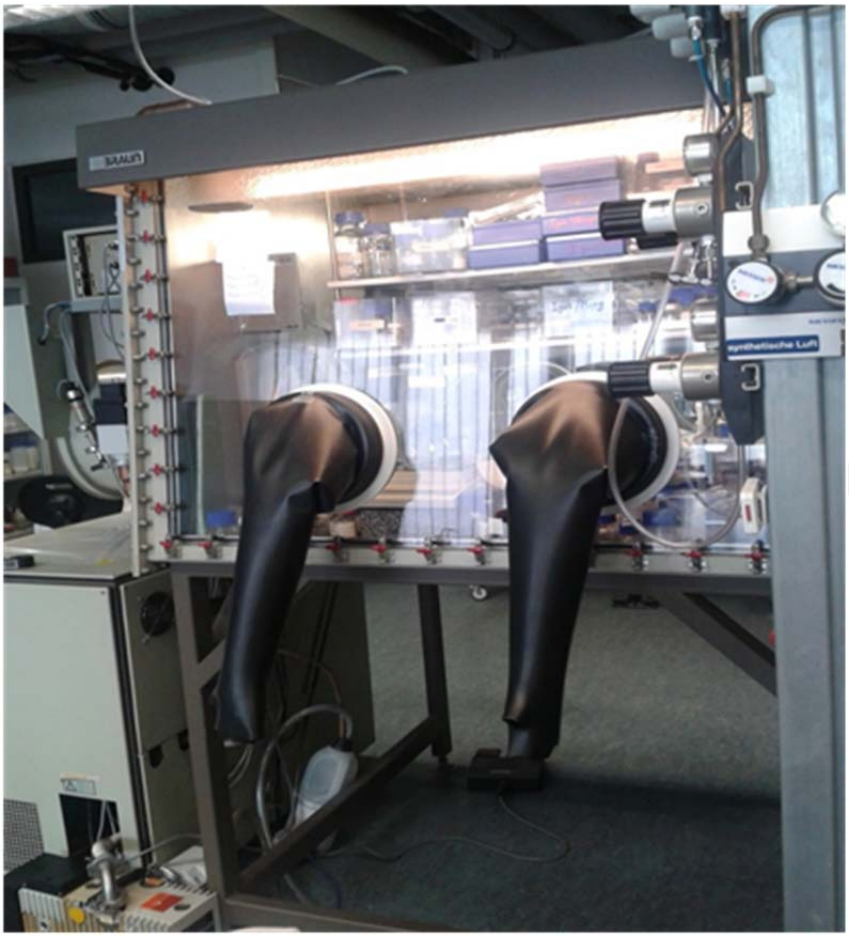

Figure 3.5. The picture of glove-box (NIMS, Japan).

3.2. Measurement Techniques

3.2.1. X-Ray Diffraction

Since then, the discovery of X-rays by Wilhelm Conrad Roentgen in 1895 enabled paramount innovations in scientific research. X-ray Techniques are experimental methods employed in materials science and engineering, it is compose of three main categories: The first one is the X-ray fluorescence spectroscopy which is commonly employed to identify qualitative and quantitative analysis. The second one is the X-ray radiography which is an imaging technique. It is built on the record of the intensity passing through an matter by employing detectors. This gives information about the domestic structure noticeable because of the local alteration of the absorption. The last one is the X-ray diffraction method is formed on the capability of crystals to diffract X-rays in a characteristic manner which gives information the structure of crystalline phases.

The working principle of the method is built on the diffraction of X-rays by periodic atomic planes and the angle or energy-resolved detection of the diffracted signal. When a monochtomatic X-ray beam is incident on the surface of a crystal, it is reflected. However, the reflection occur when at particular angles of incidence which satisfy Bragg's law;

$$2d_{hkl} \sin\theta = n\lambda \qquad (3.1)$$

where λ is the X-ray wavelength, d_{hkl} is the atomic layer separation of Bragg planes. n is the diffraction order and θ is the incident angle. The data is represented as intensity distribution of the 2θ angle, so it gives us the position of atoms located in a unit cell. The peak width can be usually recognized by the full width at half maximum (FWHM). It rely upon lattice strain, crystallite size and imperfections like stacking faults in powders. Thanks to this method, we can learn the information about crystal structure suc as lattice parameters, space group, chemical

composition, qualitative phase analysis *etc* (Omar, 1993; Solyom, 2007; Tozman, 2016; Epp, 2016).

In this study, X-ray analysis were done on powders extracted from the wires, after their fabricating and the following heat treatments. The obtained powders were crushed in an agate mortar to obtain very small particle size for XRD measurement. Structural characterization was carried out by powder X-ray diffraction (XRD) with a Rigaku MiniFlex 600 with Cu-Kα radiation and a constant scan rate (0.002 or 0.001) between 2θ = 10 – 70° (Figure 3.6). Phase characterization was carried out with the FullProf program, using the ICDD Database.

Figure 3.6. The picture of Rigaku MiniFlex 600 (www.rigaku.com).

3.2.2. Scanning Electron Microscopy

A scanning electron microscope (SEM) generates images of a specimen by scanning the surface with a high-energy beam of electrons. As the electrons interact with atoms in the specimen, generating various signals that reveal information about the surface morphology, grain size, grain shape, volume fractions and distribution of various phases, defects such as cracks and voids, composition of the sample. The SEM, since its invention in 1937 by Von Ardenne,

begun to be used commercially in 1965 (Choudhary et al., 2017). The scanning electron microscope utilizes the signals to generate an image stem from interactions of the electron beam with atoms at different depths inside the specimen which depend on the accelerating voltage and the density of the sample. Various types of signals are accumulated by one or more detectors to obtain images, and are composed of secondary electrons (SE), back-scattered electrons (BSE), characteristic X-rays and Auger electrons, as shown in Figure 3.7.

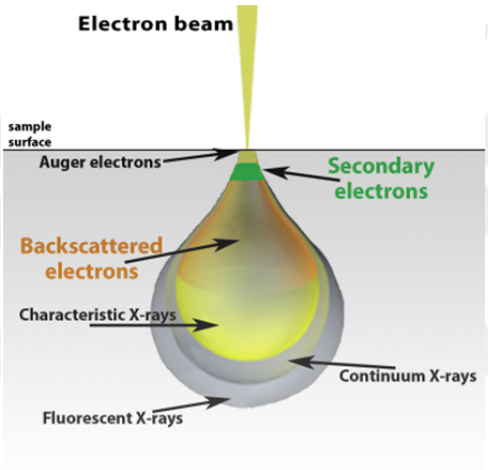

Figure 3.7. Principle of SEM from figure by JOEL Ltd.

Secondary electrons (SE) are produced in the whole volume of the specimen. Since the energy of SEs are very low (less than 50 eV), those created at a deep region are rapidly absorbed by the specimen. However, only those generated at a small volume (a few nm) close to the surface of specimen are emitted outside of the specimen. In addition to the amount of secondary electron emission increases when the electron beam penetrates obliquely compared to the incidence beam penetrates perpendicularly to the specimen. So, the image of secondary electrons shows different brightness because of the incidence angle of the electron beam. Hence, secondary electrons are very beneficial for the inspection of the topography of the sample's surface. Backscattered electrons have higher energy

(approximately the incidence electron beam) than secondary electron, thus they manage to penetrate a deeper region (300 nm). The BCEs are very sensitive to the composition of the specimen. Morever, if the electron beam penetrates a crystalline specimen with a monotony composition, the backscattered electron intensity alters depending on the crystal orientation. Characteristic X-rays with high energy range are excited by the interaction of electrons with the specimen over 1000 nm depth. A high-energy beam of charged particles is focused onto the sample and it excites the electrons from lower to higher energy shells. The difference between these energy shells may be released in the form of a characteristic X-ray. They can be detected by a Si (Li) detector and they give qualitative and quantitative information about the sample. (Collett, 1970; Echlin, 2013; Tozman, 2016).

In this thesis, the analysis of the microstructure and composition of all wires was carried using a JOEL JSM−6010 LA with secondary electron, backscattered electron and EDX, detectors, as shown in Figure 3.8. The wire is embedded in epoxy which is extracted from a plastic holder in order to obtain a shiney and smooth surface. An accelerating voltage of 15 and 20 kV is used to get elemental information from the material. Working distance is kept between 8- 11 mm.

Figure 3.8. The picture of JEOL JSM-6010 LA (www.zmb.uzh.ch).

3.2.3. Physical Property Measurements in a Cryogen-Free System (PPMS DynaCool)

The PPMS DynaCool is a redefined device that supports all the abilities of the PPMS without the need for any liquid cryogen. The system is a unique measuremet system used in the laboratory due to its fully automated low temperature and magnet system to investigate the physical properties of materials. For measurement, a temperature range of 1.85 - 400 K and magnetic fields up to ∓ 9 T can be executed.

This device uses a two-stage pulse tube cryo-cooler for both the superconducting magnet and the temperature control system, providing lower maintenance costs and also a low-vibration environment for spicemen measurements. Sample chamber's temperature is controlled by a minimum amount (~ 150 cc) of liquid helium produced by the cryocooler (PPMS User's Manual).

It consist of two cooling flow modes: main and low temperature flow. In the main mode helium gas in the pail runs up the counter flow heat exchanger (CFE), arrives at the mass flow controller, and then, back off the CFE into the cooling annulus. This mode temperatures of 10K are possible to attain. However, for below 10 K, the low temperature mode is activeted instead of the main mode. In this case, the liquid 4.2 K from the pail is enlarged through the capillary run impedance. Because the pressure difference at the inlet of and the outlet the impedance is 1 atm and 10 Torr, respectively. So, some of the helium evaporates resulting in a mixture of liquid and gas at ~ 1.7 K that runs to the bottom of the cooling annulus (PPMS User's Manual).

The base unit of the PPMS is compose of there main system (in Figure 3.9). The first one is cryostat control system which is liable for maintaining the cryostat components at the true temperatures. The cryostat control system is composed of subsystem to do this such as pulse tube cryocooler, thermal isolation, monitoring and control and startup operation. The second one is chamber temperature control system which is mainly responsible of how the chamber

temperature is regulated and measured. This provides a thermally uniform region for the sample environment by using a high-conductivity copper to minimize temperature gradient. The third one is magnetic field control system which checks the magnetic field at the sample location. It is made of the superconducting magnet and leads, the magnet controller, software, and the magnet shield. The magnet system is a TiNb 9T superconducting coil conducting-cooled one (by the second stage at the cryocooler), whose current is controlled with precision by a hybrid digital/analog magnet controller (PPMS User's manuel).

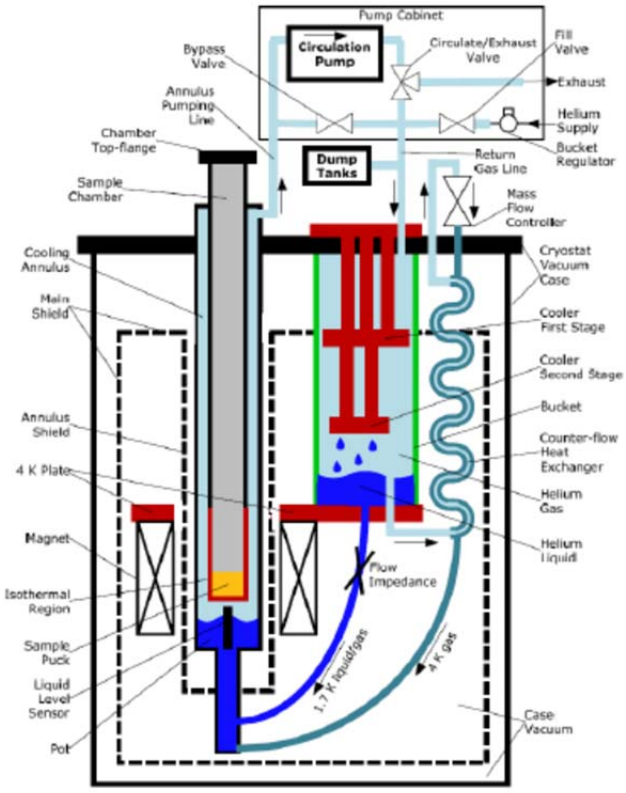

Figure 3.9. The DynaCool Cryostat showing the components of the Cryostat Control System, Chamber Temperature Control System, and Magnetic Field Control System (PPMS User's Manual).

In this work, a 9T PPMS DynaCool, from Quantum Design was used (see Fig. 3.10) with two different options Electronic Transport Option (ETO) and the Vibrating Sample Magnetometer (VSM).

In the ETO option a sample pack has three channels with gold-plated pads ($I+$,$V+$,$V-$ and $I-$) which are used to operate in one of two modes : the two-point probe is suitable for high impedance ranging between 2 MW and 5 GW and the four-point probe (used in this work) is suitable for low impedance ranging between 1μW and 10 MW (PPMS, ETO User's Manual). In the standart four-probe measurement, two leads pass a current through the sample and two separate leads measure the potential drop across a section of the sample. The four probe measurement eliminated the contact and lead resistance which make a contribution onto the measurement result. Therefore this technique is preferably applied to low resistive measurements. According to Ohm's law, R = V/I, can then be used to calculate the resistance of the sample for the region between the two voltage leads.
The magnetometry measurements were performed by using VSM option of the DynaCool PPMS. We measured temperature dependence of magnetization to determine the critical temperature and the hysteresis loop to calculate the current density.

Figure 3.10. PPMS DynaCool magnetometer (www.qd-latam.com).

4. RESULTS AND DISCUSSION

4.1. Results of the $FeSe_{0.5}Te_{0.5}$ Single Crystal

The XRD pattern of both single crystal $FeSe_{0.5}Te_{0.5}$ are demonstrated in Fig. 4.1. The crystals were obtained to be very shiny, grown along the ab-plane, which were easy to split along that plane. The single crystal $FeSe_{0.5}Te_{0.5}$ samples indicate four narrow and sharp peaks at about $2\theta \approx 14.69°$, 29.63°, 45.11°, 61.52°, which correspond to the reflected intensity (001), (002), (003), (004) planes of the tetragonal crystal structure with space group of *P4/nmm*, in agreement with earlier reports (Yadav et al., 2009; Koshika et al., 2013). According to the results, the two different cooling rates do not lead to any difference in the crystal structure, but the lattice parameter of slow cooling sample is slightly smaller than rapid cooling sample where a = 3.8029 Å, c = 6.0154 Å and a = 4.0151 Å, c = 6.0204 Å, respectively.

Figure 4.2 displays SEM images and EDX map images for both crystals. According to SEM images, both samples are demonstrated a terrace-like formation. EDX map analysis and point spectrum (Figure 4.2c, d) confirms that the distrubution of Fe, Se and Te is homogenous for both samples. The composition of rapid cooling sample is as $FeSe_{0.5}Te_{0.5}$ and for slow cooling sample is as $Fe_{0.98}Se_{0.56}Te_{0.43}$. This obviously demonstrates that the two different cooling rates have not affected the distribution of elements in the crystal.

To investigate the temperature dependence of magnetization, M(*T*), magnetic measurements were performed under an applied magnetic field of 50 Oe and in the range of 8–50 K temperatures for the rapid cooling and the slow cooling samples in zero field cooled (ZFC) process. The superconducting transition is observed at about 14.62 for rapid cooling sample and 14.38 K for slow cooling sample (Figure 4.3). This result is in good agreement with earlier report (Taen et al., 2009).

Figure 4.4a, b display that the magnetic hysteresis behavior of samples under applied fields between ± 7 T at 5, 7, 9, 11 K. It is seen that the width of hysteresis of the rapidly cooled sample are larger than that of the slow cooled sample at 5 K, however the the width of hysteresis decrease sharply with increasing tempearture for both samples. It is argued that the pinning effect becomes weaker resulting in a decrease in the width of hysteresis loops by increasing temperature value. According to data taken at 5 K, the lower critical magnetic fields, $\mathbf{H_{c1}}$, of rapid cooling sample and slow cooling sample are estimated as 287 and 209 Oe, respectively.

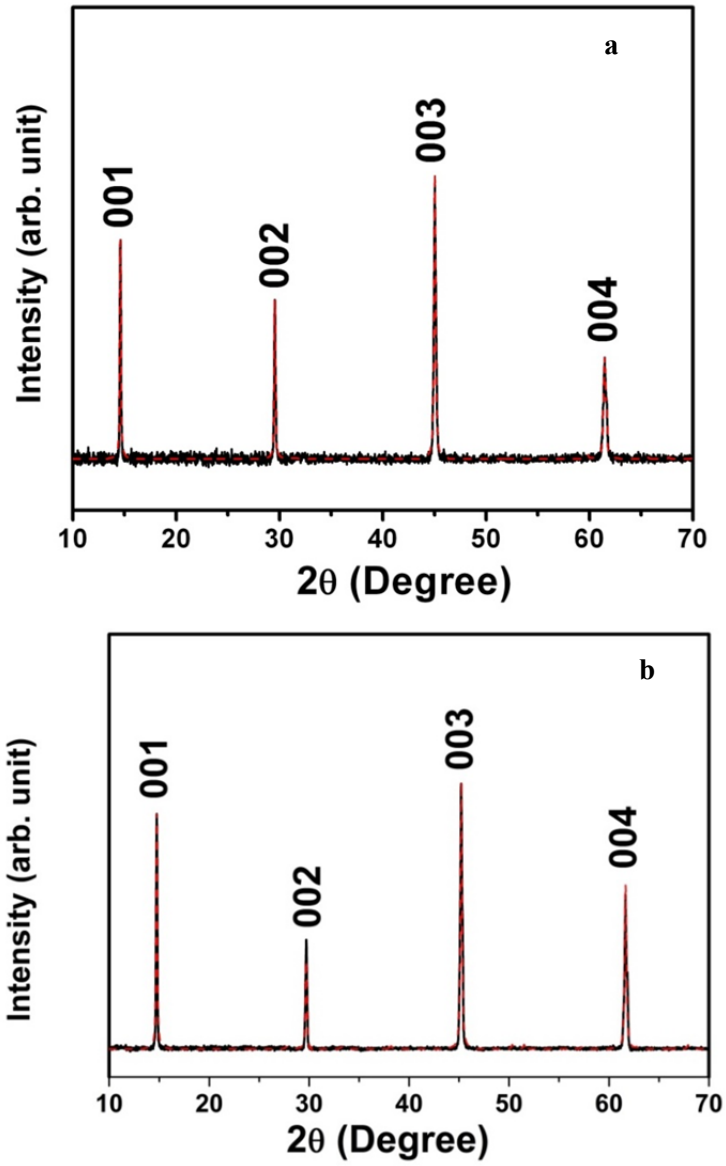

Figure 4.1. XRD patterns **(a)** for the rapid cooling sample; **(b)** for the slow cooling sample.

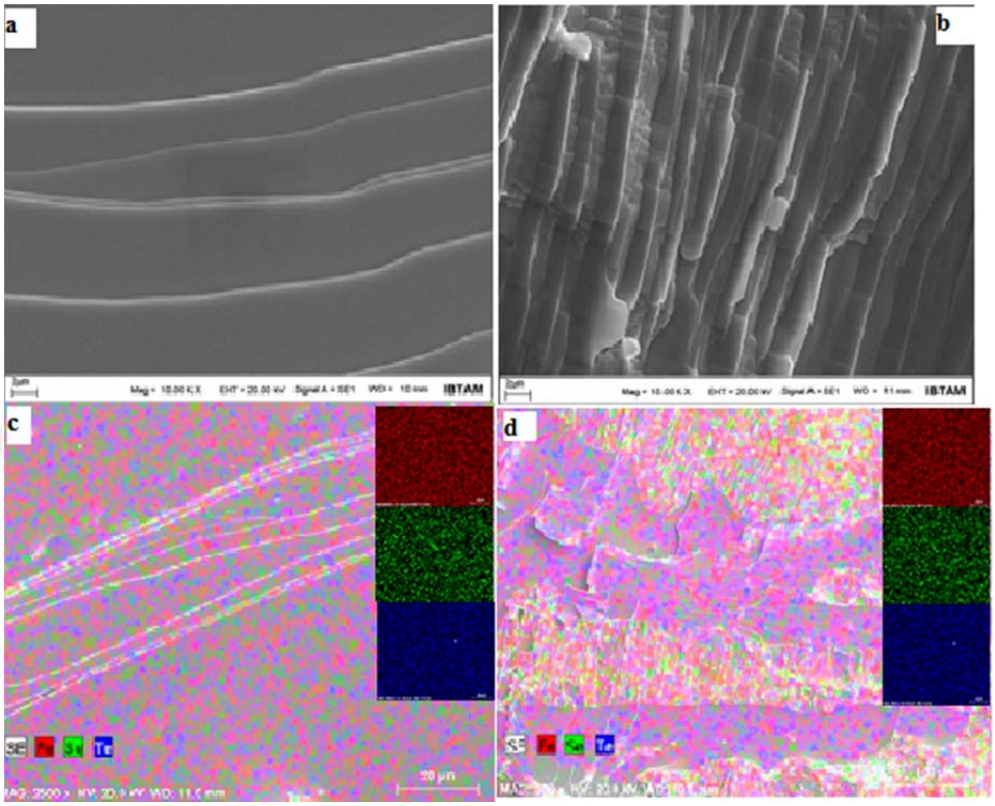

Figure 4.2. SEM images and EDX map images of samples **(a)** and **(c)** for the rapid cooling sample; **(b)** and **(d)** for the slow cooling sample

Figure 4.5 shows critical current densities, J_c, for both samples at 5 and 7 K. The critical current density was calculated by using Bean formula given by,

$$J_c = 20\frac{\Delta M}{a\left(1-\frac{a}{3b}\right)} \quad (4.1)$$

where a and b (a < b) are the sample dimensions perpendicular to applied field, and ΔM is the difference between the magnetizations for the decreasing and the increasing field case. As can seen that the J_c is dashingly decrease up to 1 T, and then, unchanged with increasing magnetic field. The value of J_c for the rapid

cooling sample is enhanced about 3 times compared to the slow cooling sample. These differences between the samples can be attributed to the increasing cooling rate which increases the superconducting properties.

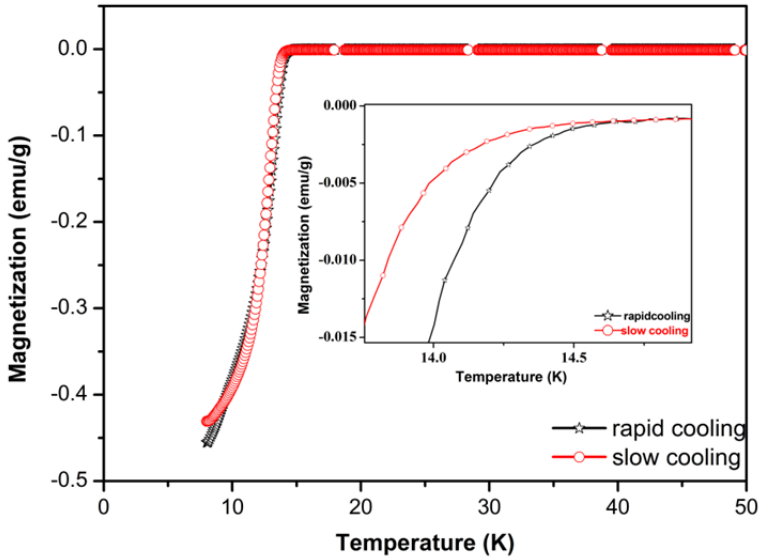

Figure 4.3. Magnetization aganist temperature for the rapid and the slow cooling samples.

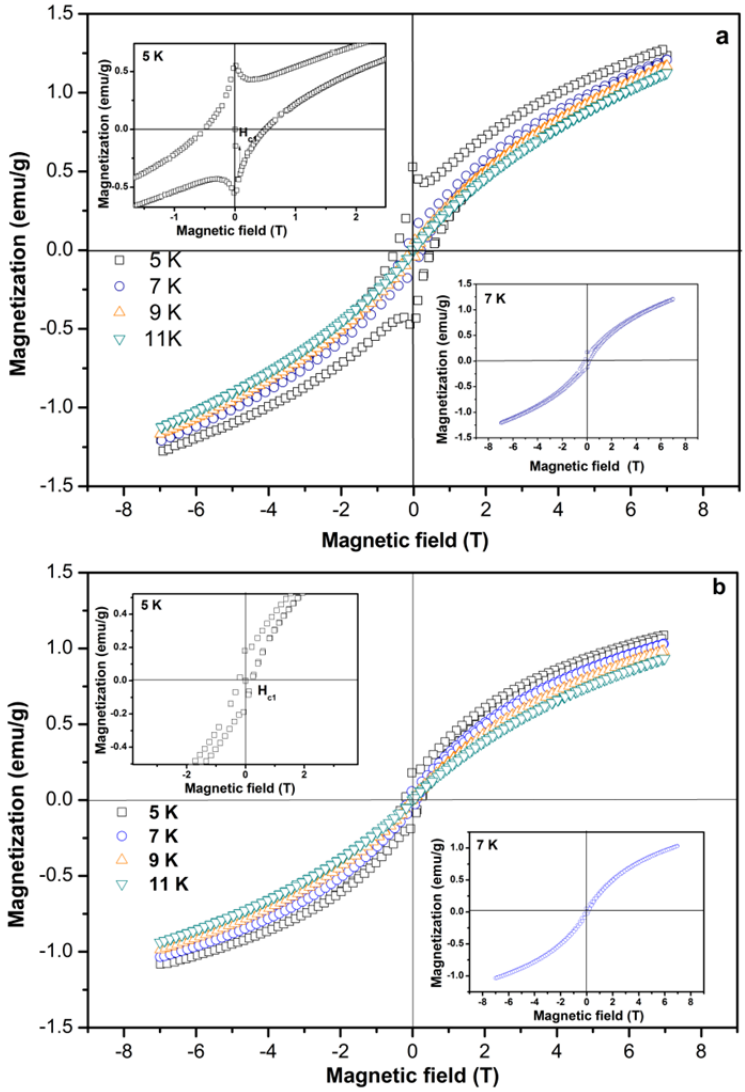

Figure 4.4. Magnetization versus magnetic field curves **(a)** for the rapid cooling sample; **(b)** for the slow cooling sample.

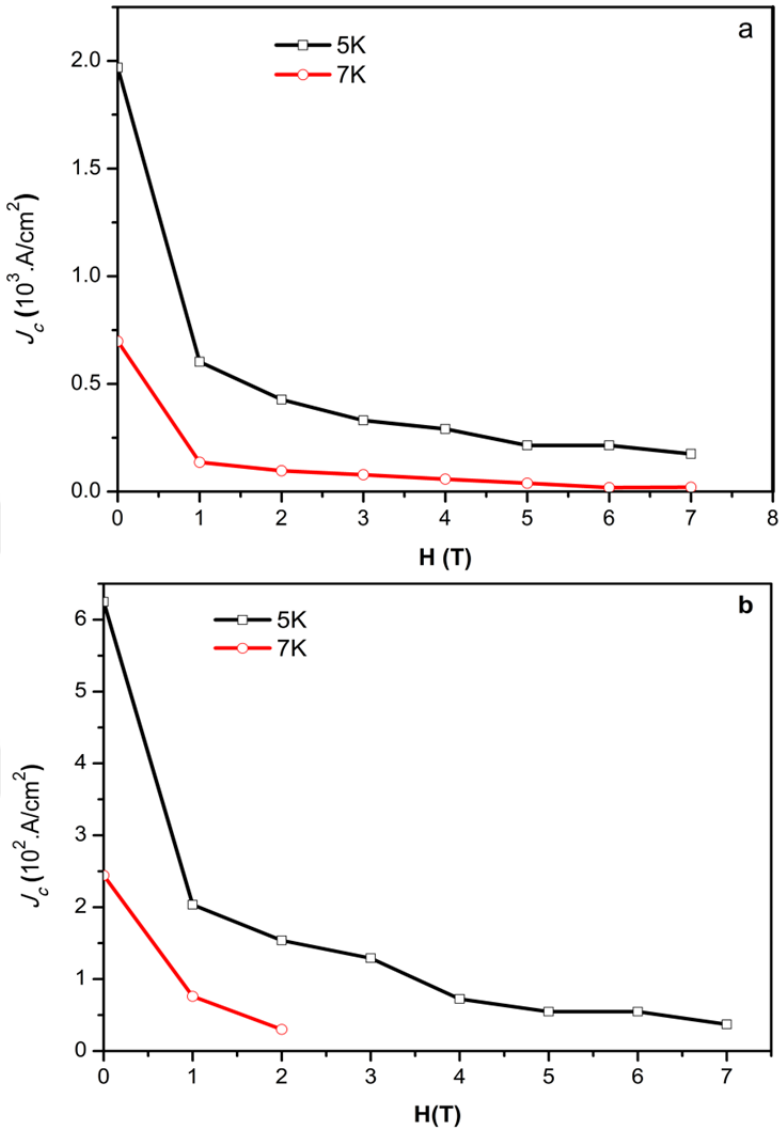

Figure 4.5. Criticial current densities versus magnetic fields **(a)** for the rapid cooling sample; **(b)** for the slow cooling sample.

To investigate the flux pinning mechanism, the flux pinning force was calculated, $\mathbf{F_p} = J_c \times \mathbf{H}$, by using critical current densities, J_c. The flux pinning behavior was defined by Dew-Hughes (1974) and Kramer (1973) for conventional superconductors. Based on the Dew-Hughes model, the pinning force density f_p should be scaled to applied magnetic field and the scaling law is given by $f_p = Ah^p(1-h)^q$ where A is a proportionality costant, p and q parameters that determine the origin of the pinning mechanism, f_p is the normalized pinning force - $\mathbf{F_P} / \mathbf{F_{Pmax}}$ and h is the reduced magnetic field $\mathbf{H} / \mathbf{H_{irr}}$. According to the the Dew-Hughes model, there exist six point pins namely; at h = 0.33 (p = 1, q = 2) for normal point pins ($\delta\ell$), at h = 0.2 (p =0.5, q = 2) for normal surface pins ($\delta\ell$), at h = 0.67 (p = 2, q = 1) for δT_c pins, at h = 0.6 (p = 1.5, q = 1) for δT_c surface pins, and at h = 0.5 (p = 1, q = 1) for δT_c volume pins.

In Figure 4.6, the normalized pinning force f ($\mathbf{F_p}/\mathbf{F_{pmax}}$) was plotted versus the reduced magnetic field h ($\mathbf{H}/\mathbf{H_{irr}}$) for the rapid cooling sample at 5 and 7 K. It displays that the curves overlap very well with the peak position located at about h = 0.54. It is also observed that our data fit to Dew-Hughes model, and the fitting parameters are found as A = 2.73, p = 0.81 and q = 0.69, the ratio $[p/(p+q)] \sim 0.54$. This result indicates that the pinning contribution arising from δT_c–type pins in which the theoretical values are p = 1, q = 1 and h = 0.5 for δT_c volume pinning mechanism given by Dew-Hughes and the maximum is expected to occur at h > 0.5. Our result shows that h is 0.54, which indicates a strong contribution is coming from the δT_c–type.

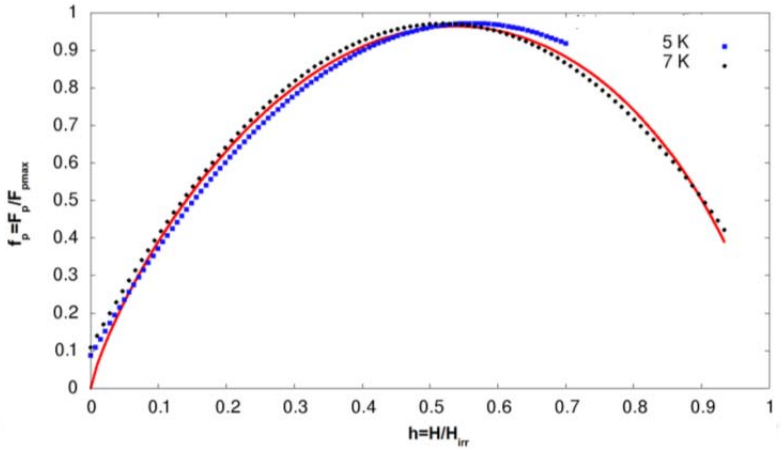

Figure 4.6. The scaled density of the pinning force f ($\mathbf{F_P/F_{Pmax}}$) as a function of the reduced field, h = $\mathbf{H/H_{irr}}$ for 5 and 7 K for rapid cooling sample. Red line represents the fitted curve

4.2. Results of the $Fe_{1+d}Se_{0.4}Te_{0.6}$ Polycrystals (d = 0 %, 5%, 10%)

The XRD pattern of the as-grown $Fe_{1+d}Se_{0.4}Te_{0.6}$ (d = 0 %, 5 %, 10 %) polycrystals are demonstrated in figure 4.7. The XRD pattern of the as-grown samples indicate that it is mainly composed of the tetragonal PbO type (*P4/nmm*) phase with a minor hexagonal (*P31*) secondary phase. Table 4.1 displays the lattice parameters which were deduced by Rietveld analysis. From the data, one can infer that the lattice parameter, a and c decrease with increasing the amount of iron for the as-grown samples.

Table 4.1. Lattice parameters which were determined by reitveld of the as-grown $Fe_{1+d}Se_{0.4}Te_{0.6}$ sample (d = 0 %, 5 %, 10 %).

Sample	a (Å)	c (Å)
d = 0 %	3.8017	6.0599
d = 5 %	3.7980	6.0566
d = 10 %	3.7934	6.0197

SEM-BSE images for the as-grown $Fe_{1+d}Se_{0.4}Te_{0.6}$ d = 0, 5 10 % samples are displayed in fig. 4.8. the SEM-BSE images demonstrate that there are some cracks and voids in the whole scanning region. According to the EDX point spectrum for three as-grown samples, the average compositions of samples are calculated as $Fe_{1.05}Se_{0.39}Te_{0.61}$ for d = 0 %, $Fe_{1.12}Se_{0.38}Te_{0.61}$ for d = 5 % and $Fe_{1.17}Se_{0.42}Te_{0.58}$ for d = 10 %. It confirms that all samples are distributed homogenously.

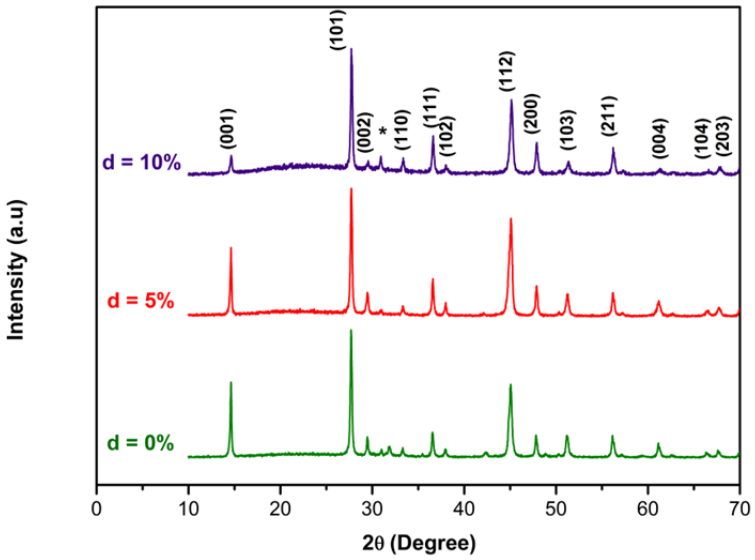

Figure 4.7. XRD patterns for the as-grown $Fe_{1+d}Te_{0.6}Se_{0.4}$ samples d = 0% (green), d = 5% (red) and d = 10% (purple).

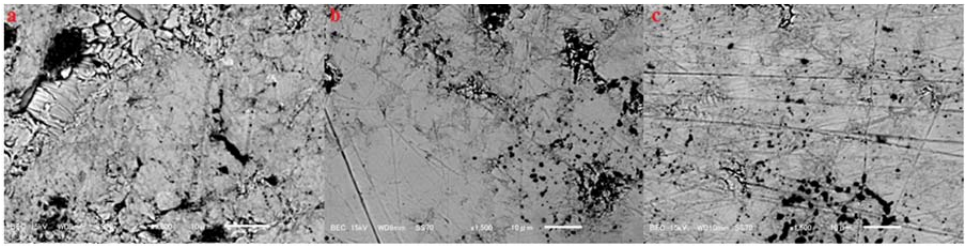

Figure 4.8. SEM images for **(a)** d = 0 %; **(b)** d = 5 %; **(c)** d = 10 % the as-grown $Fe_{1+d}Te_{0.6}Se_{0.4}$ samples.

According to magnetization dependence of temperature (Figure 4.9), the d= 0% as-grown sample shows bulk superconductivity at 13.02 K. In the case of the d = 5% excess iron sample does not exhibit bulk superconductivity and transition temperature is observed at 6.19 K for the 5% excess iron sample. The superconductivity observed for that sample may be filamentary. The M(*T*) data from the d = 10 % crystal shows no evidence of superconductivity. Furthermore, the positive background in the M(*T*) is observed in all samples which is attributed to the existence of the excess iron. The superconducting transition temperature of the as-grown crystals began to decrease and are accompained by superconducting volume fraction by increasing the amount of iron, in agreement with the literature (Fang et al., 2008; Mizuguchi et al., 2010; Ohno et al., 2014). In the literature, there are lots of papers which focused on the nonstoichiometric iron in the FeSeTe compounds. As we know that each compound contain a common layered structure based on a square planar Fe layer tetrahedrally constructed of chalcogen atoms, it exhibits an attractive aspect: in the interstitial sites of the chalcogen layers permit partial occupation of iron, causing nonstoichiometric composition Fe_{1+d}(Se,Te), where d is excess iron at interstitial sites. These excess iron give rise to suppressed superconductivity in the compounds.

The XRD pattern of the S-annealed $Fe_{1+d}Se_{0.4}Te_{0.6}$ samples show that it crystallizes mainly in the tetragonal structure with a minor of the orthorhombic FeS (*Pnma*) secondary phase also visible (Figure 4.10). Fe atoms occupy in the Wyckoff positions of 2a (0.75, 0.25, 0), the Se/Te atoms 2c (0.25, 0.25, 0.2702) for the d = 0 % sample; Fe atoms 2a (0.75, 0.25, 0), the Se/Te atoms 2c (0.25, 0.25, 0.26734) for the d = 5 % sample; Fe atoms 2a (0.75, 0.25, 0), the Se/Te/S atoms 2c (0.25, 0.25, 0.26938) for d = 10 % sample by reitveld analysis. These results confirm that the de-intercalation of excess iron is composed of the second phase as the orthorhombic FeS for d = 0 and 5 % samples, however in the d = 10 % excess iron, Sulfur enters in the main phase as well as the deintercalation of the excess iron. The lattice parameters a and c of the main phase shows in Table 4.2, which

were deduced by Rietveld analysis. Increasing the amount of excess iron up to d = 5 %, the lattice parameter a slightly increases and the lattice parameter c decreases, however, both lattice parameters incease for the d = 10 % sample, comparing the as-grown sample. The expansion of the lattice confirms that the main phase contains Sulfur.

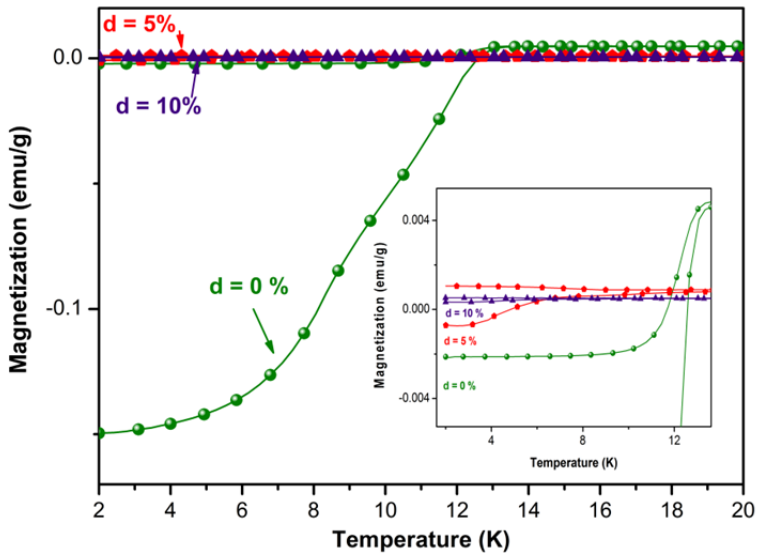

Figure 4.9. FC-ZFC magnetization versus temperature at 10 Oe for the as-grown $Fe_{1+d}Te_{0.6}Se_{0.4}$ samples d = 0% (green); d = 5% (red) and d = 10% (purple).

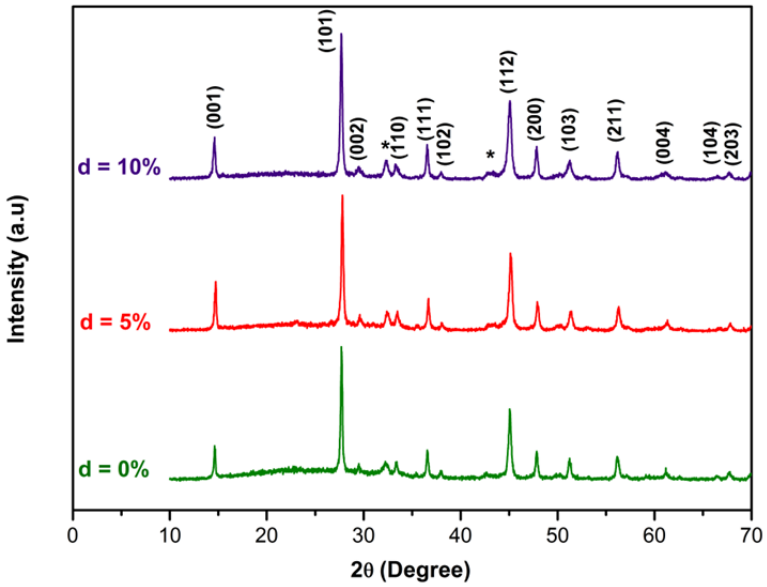

Figure 4.10. XRD pattern for the S-annealed $Fe_{1+d}Te_{0.6}Se_{0.4}$ samples d = 0% (green); d = 5% (red) and d = 10% (purple).

Table 4.2. Lattice parameter, volume and density which were determined by Rietveld of the S-annealed $Fe_{1+d}Se_{0.4}Te_{0.6}$ sample (d = 0 %, 5 %, 10 %).

Sample	a (Å)	c (Å)	Volume (A^3)	Density(g/cm^3)
d = 0 %	3.8032	6.0571	87.613	6.120
d = 5 %	3.7999	6.0498	87.360	6.234
d = 10 %	3.7985	6.0488	87.278	6.155

SEM-BSE images for all samples and EDX map images for the d = 10 % the S-annealed $Fe_{1+d}Se_{0.4}Te_{0.6}$ samples are displayed in Figure 4.11. It demonstrate that there are some cracks and voids in the whole scanning region. According to point and line spectrum; dark gray area belong to all elements (Fe, Se, Te, S), the bright part belongs to Te-rich Fe-Se-Te-S. From the elemental mapping image, we found that there are some sulfur-rich regions in the d = 10 % sample. In these regions, the elemental content of Se is significantly changed. It confirms that sulfur is substituted for selenium in some region.

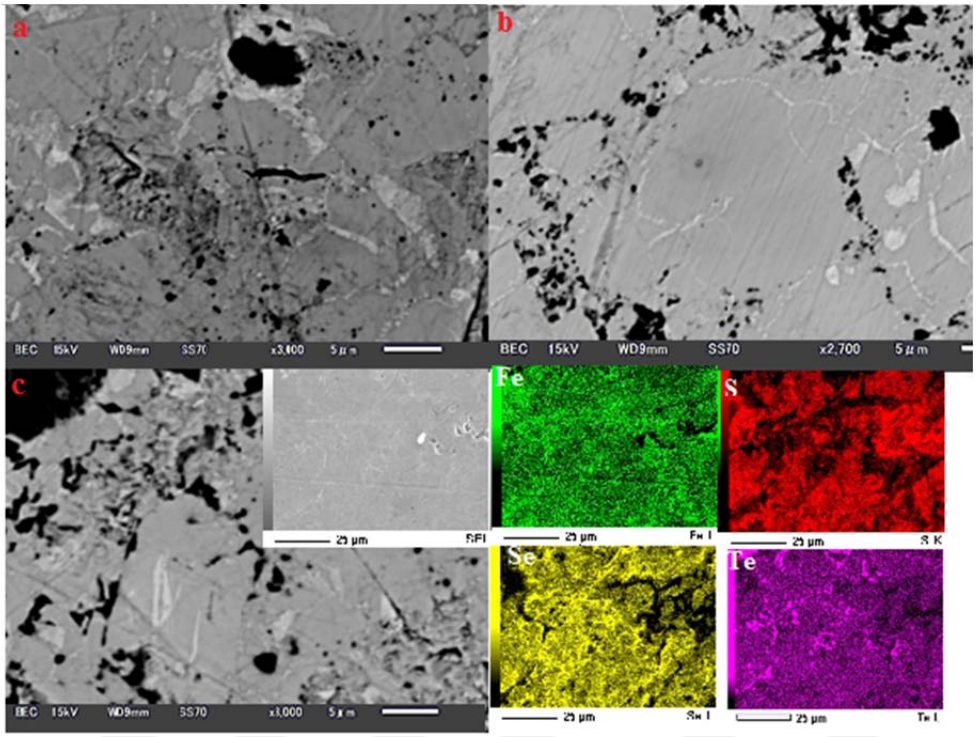

Figure 4.11. SEM images for **(a)** d = 0 %; **(b)** d = 5 %; **(c)** d = 10 % the S-annealed $Fe_{1+d}Te_{0.6}Se_{0.4}$ samples, respectively. And, EDX map images for the d= 10 % sample.

Figure 4.12 displays the temperature dependence of the magnetization, **M**(*T*), at 10 Oe and the FC-ZFC process. We found that the S-annealled samples show a definitive trace of superconductivity, whereas the as-grown d = 5 and 10 % samples do not show bulk superconductivity as in the as-grown. The diamagnetic signal is remarkably enhanced and superconducting transition temperature reach up to 14 K, and clear evidence of bulk superconductivity, accompained by superconducting volume fraction in all the samples. These results are consistent with the values reported for single crystal and polycrystals (Sales et al., 2009; Li et al., 2009; Fang et al., 2010). Transition temperature and superconducting volume fraction of the as-grown and the S-annealled $Fe_{1+d}Se_{0.4}Te_{0.6}$ (d = 0, 5, 10 %) are given in Table 4.3.

Table 4.3. Transition temperature and superconducting volume fraction of the as-grown and the S-annealed $Fe_{1+d}Se_{0.4}Te_{0.6}$ (d = 0, 5, 10 %).

	d (%)	T_c (K)	S.V.F (%)
As-grown	0	13.02	96
	5	6.19	0.8
	10	—	—
S-Annealing	0	14.34	45
	5	14.39	60
	10	14.56	62

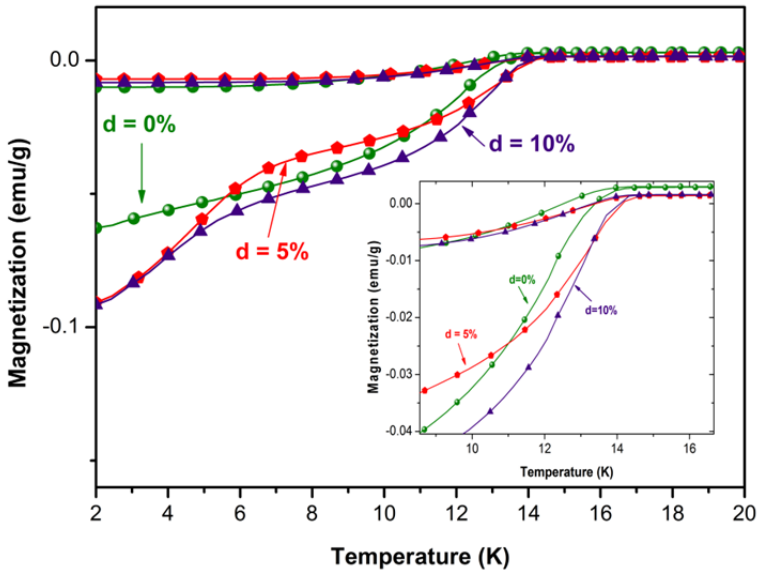

Figure 4.12. FC-ZFC magnetization versus temperature at 10 Oe for the S-annealed $Fe_{1+d}Te_{0.6}Se_{0.4}$ samples d = 0% (green), d = 5% (red) and d = 10% (purple).

4.3. Results of the Ag Doped $FeSe_{0.94}$ Polycrystals

Figure 4.13a displays the XRD pattern for the as-grown and the annealed Ag doped $FeSe_{0.94}$ polycrystal. According to the XRD, the reflection peaks are well indexed tetragonal stucture with space group *P4/nmm*, but additional peaks are

appeared at 2θ = 31° and these peak is belonged to hexagonal Fe_7Se_8, which is shown with asterisk for both samples. Morever, as can be seen from figure 4.13a, there is a peak at about 2θ ≈ 38° which belong to the Ag. This confirms that the Ag is not reacted with Se, indicating that the Ag is incorporated in the unit cell. By using the standard pattern matching method of the Fullprof, the lattice parameters of the as-grown and the annealed Ag doped $FeSe_{0.94}$ polycrystal were calculated as a = 3.7683 Å; c = 5.5139 Å and a = 3.7673 Å; c = 5.5166 Å, respectively, indicating that the lattice a is slightly shrinked and the lattice c slightly expanded following the annealing process. We have shown the (001) peak of both samples in figure 4.13b. It confirms that the intensity of (001) peak slightly increase due to enhances of texturing as well as the displacement of peak after the annealing.

SEM images and EDX map images for the annealed sample displays in Figure 4.14. According to SEM image, the sample has granular morphology. EDX map analysis and point spectra of the sample confirms Ag agglomerate in irregular amounts and distribution of Fe and Se are almost homogeneous, as given in Table 4.1.

Figure 4.15 displays the temperature dependence of the magnetization, **M**(*T*), at 100 Oe and the FC-ZFC process. The superconducting transition is observed approximately 8 K for both samples, in agreement with the literature (Galluzzi et al., 2016; Nazarova et al., 2015). However, the bulk superconductivity is not obtained for the as-grown sample. The presence of positive value above and below T_c attributed to considerable positive signals due to the existence of some magnetic impurities such as iron and the hexagonal Fe_7Se_8 (Williams et al., 2009; Mendoza et al., 2010). In fact, according to the theoretical results, the tetragonal FeSe is not exhibit any magnetic behave, however in the experimental results confirms that it exhibit magnetism which attribute to the existence of second phase like hexagonal phase or iron clusters (Wu et al., 2008; Błachowski et al., 2010).

It is worth underlining that the Ag doped and annealing increase good superconducting intergrain connections. Morever, the annealing procedure can

impove the superconductivity due to increased homogeneity (Panel et al., 2009; Yeh et al., 2009; Ge et al., 2010).

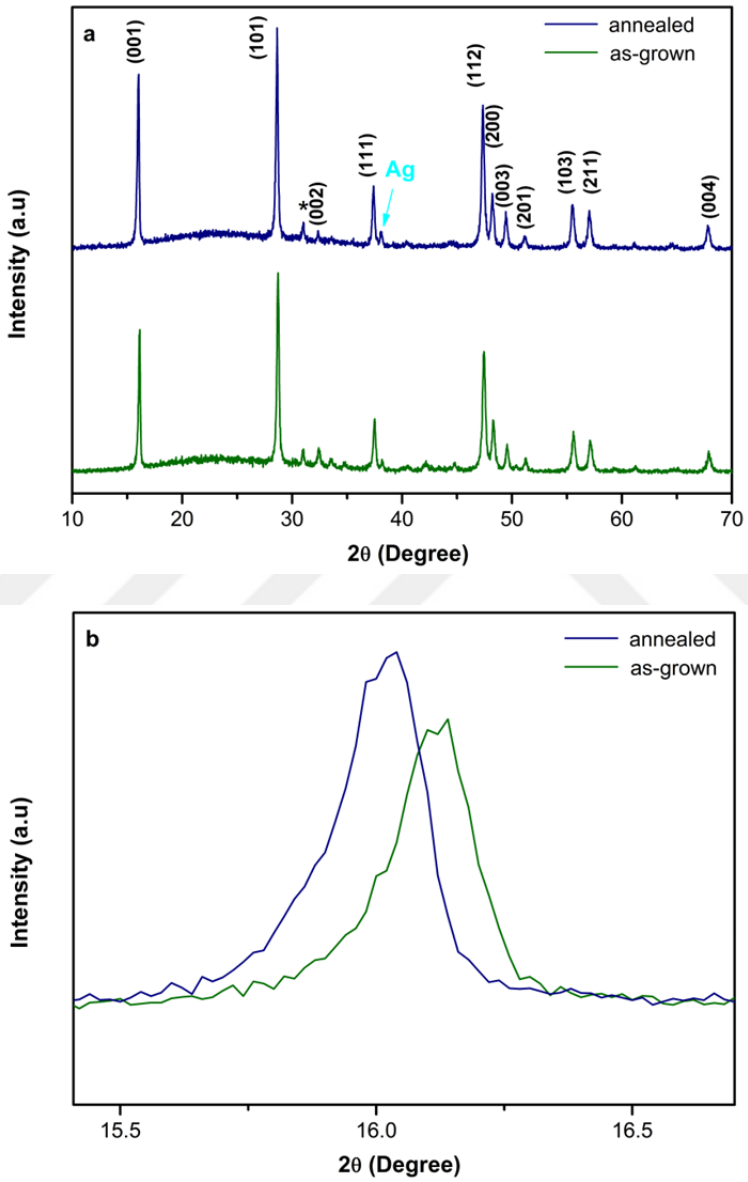

Figure 4.13. **(a)** XRD pattern for the as-grown and the annealed Ag doped $FeSe_{0.94}$; **(b)** the shifting of (001) peak for the as-grown and the annealed samples, respectively.

Table 4.4. Results from Electron dispersive X-ray (EDX) analysis in 3 different points for the annealed Ag doped $FeSe_{0.94}$.

Element	**Norm. wt %**			
Fe	29.82	47.19	49.13	39.88
Se	35.27	44.10	50.87	44.19
Ag	34.91	8.71	-	15.94

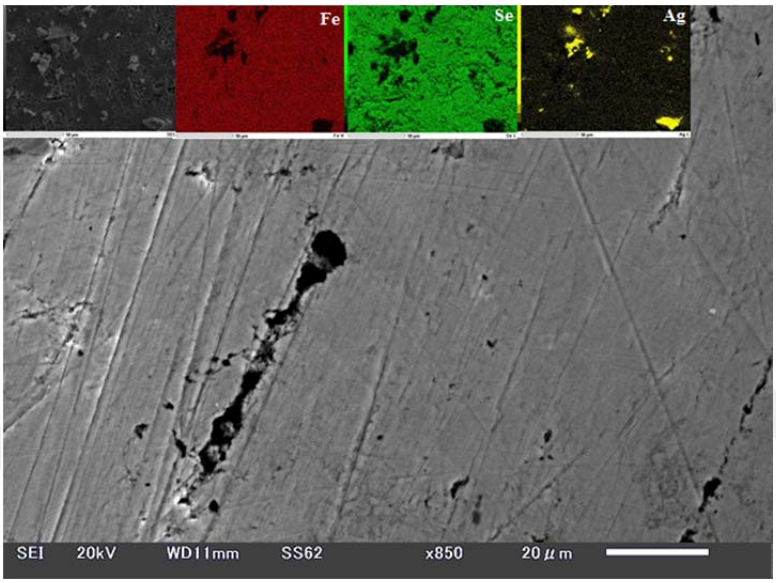

Figure 4.14. SEM image and EDX map images of SEM micrograph for the annealed Ag-doped $FeSe_{0.94}$.

In figure 4.16 shows resistivity versus temperature for the annealed sample from 140 down to 4 K at H = 0. Superconductivity occurs at temperatures below ~ 9 K. The critical temperature, T_c^{onset}, T_c^{mid} and T_c^{offset}, of the annealing Ag-doped $FeSe_{0.94}$ sample is shifted to 9.2, 8.4 and 8.03 K, respectively (see the inset of figure 4.16). The superconducting transition width is below 1 K, which may be attributed to a good quality of the sample. Morever, the sample shows a metallic behavior in the normal state.

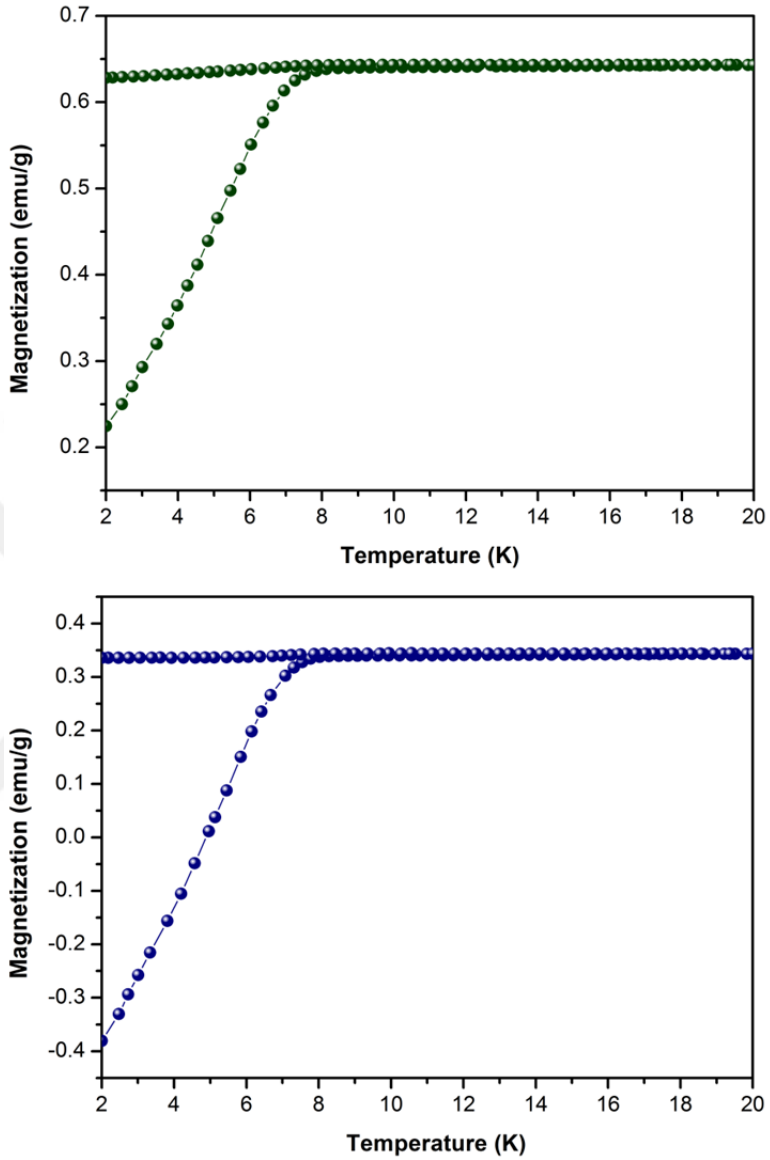

Figure 4.15. FC-ZFC magnetization versus temperature at 100 Oe for the as-grown (green) sample and the annealed sample (blue).

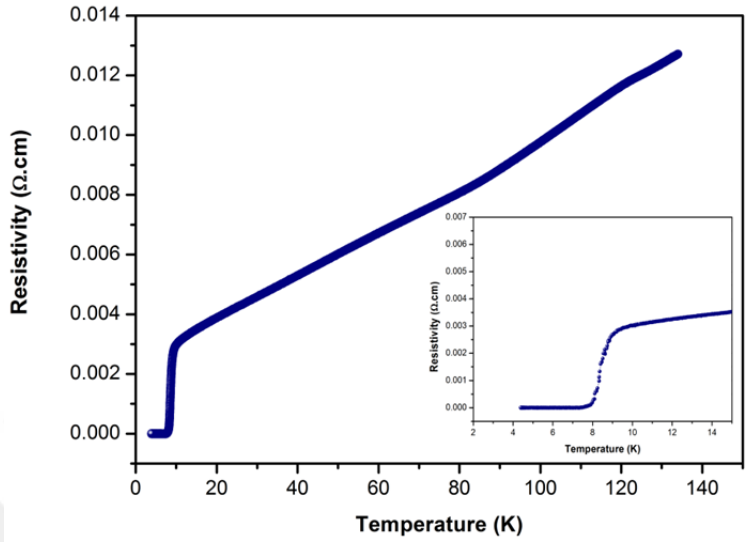

Figure 4.16. The temperature dependences of electrical resistivity for the annealed Ag doped $FeSe_{0.94}$. Inset shows an enlarged scale near the superconducting transition.

4.4. Results of the Fe(Te,Se) Wire

The obtained Fe(Se,Te) wires were annealed different conditions (Table 3.1), then each wire's physical properties were investigated.

4.4.1. Fe(Se,Te) Wire 1

Figure 4.17 displays XRD pattern for Fe(Se,Te) wire. As seen from the fig., Rietveld analysis confirms that the main phase is tetragonal $FeSe_xTe_{1-x}$ (*P4/nmm*) with lattice parameter a,b = 3.7931 Å and c = 6.0181 Å (Xu et al., 2018) and the secondary phase is hexagonal FeTe ($P6_3/mmc$) with lattice parameter a,b = 3.8818 Å and c = 5.5762 Å.

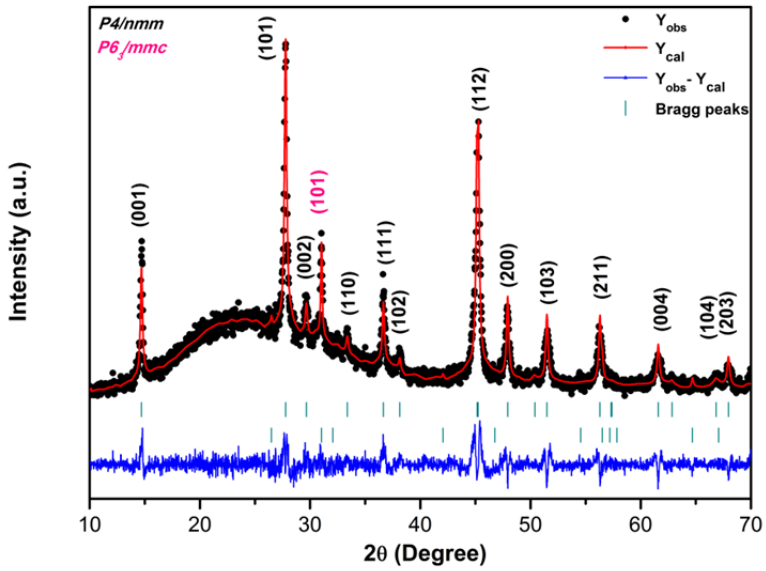

Figure 4.17. XRD pattern (black), Rietveld fit (red) and the differences between observed and calculated (blue) of Fe(Se,Te) wire 1. The rows of ticks displays the Bragg-peak positions for the main phase (*P4/nmm*) and an impurity phase (*$P6_3/mmc$*).

SEM image and EDX map images for the cross-section of the Fe(Se,Te) wire 1 confirms that the sheath supplied iron and almost homogeneously to the reacted layer of wire (in figure 4.18). The dispersal of the Se and the Te in the reacted layer is not homogeneous, whereas the element of Te and Se were mixed in a Te : Se = 1 : 1 atomic ratio. The EDX analysis confirms that the main phase is Fe(Se,Te) with composition $Fe_{0.81}Se_{0.6}Te_{0.4}$ on whole cross-section region of Fe(Se,Te) wire.

Figure 4.19 displays the resistivity versus temperature at 0 T for the Fe(Se,Te) wire 1. The ρ-T figure shows that a gradual drop in resistivity is observed the onset critical temperature at about 6.1 K, however zero resistivity is not observed. Because superconducting phase ratio is much low due to the low packing density of the raw materials. Fang et al. (2008) studied the SCs in the optimally doped Te in the FeSe compound $Fe_{1+y}(Se_xTe_{1-x})_{0.82}$ samples with different

quantities of the Fe atoms. They found that the $Fe_{1+y}(Se_xTe_{1-x})_{0.82}$ compound in the region $0 \leq y \leq 0.3$ and $0.2 \leq x \leq 0.6$ exhibit bulk superconductivity with optimally doped the Se and Te (Dong et al., 2013).

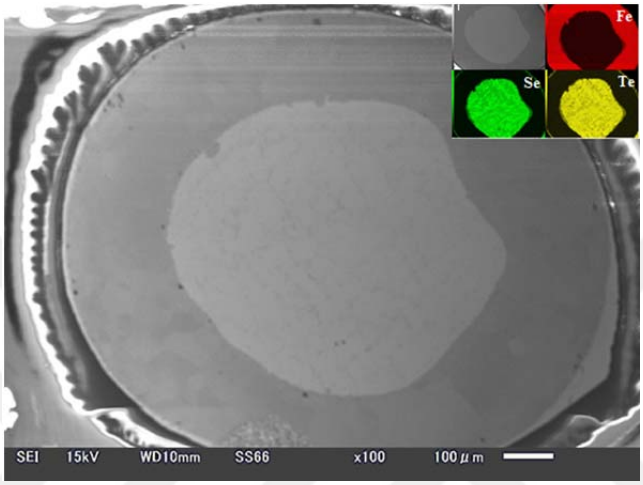

Figure 4.18. SEM image and inset; EDX map images for the cross-section of Fe(Se,Te) wire 1.

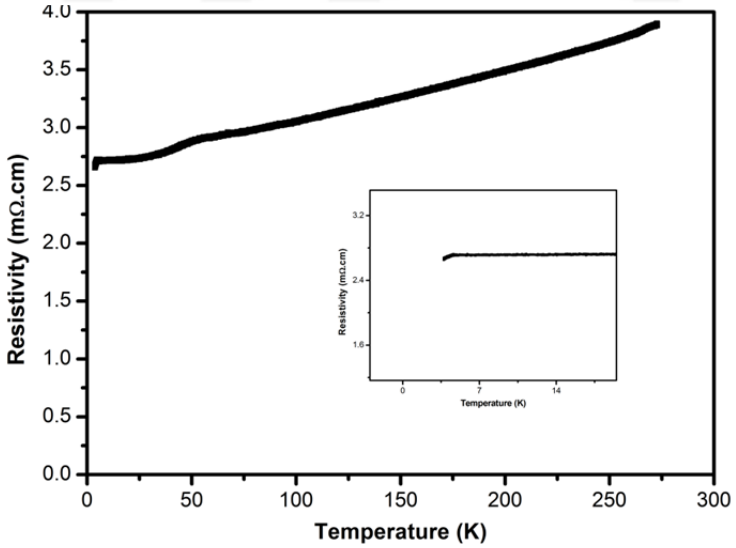

Figure 4.19. Resistivity versus temperature up to 300 K for Fe(Se,Te) wire 1.

4.4.2. Fe(Se,Te) wire 2

SEM image and EDX map images for the cross-section of the Fe(Se,Te) wire 2 shows that the reacted layer decompose two main layers: the first layer is Fe- and Te-rich with composition $Fe_{1.16}Se_{0.3}Te_{0.7}$ from EDX analysis, while the second one is Fe-rich with composition as $Fe_{1.5}Se_{0.4}Te_{0.6}$ and the distribution of the second layer is close to the center of the sheath (in Figure 4.20). Furthermore, a hole is observed in the center of cross-section because of the evaporation of the chalcogen. Results shows that the average composition of Se, Te and Fe differ from the initial composition and/or the expected composition due to diffusion of the species throughout the iron sheath, and the excess iron can come from the sheath itself (Palombo et al., 2015; Ozaki et al., 2011).

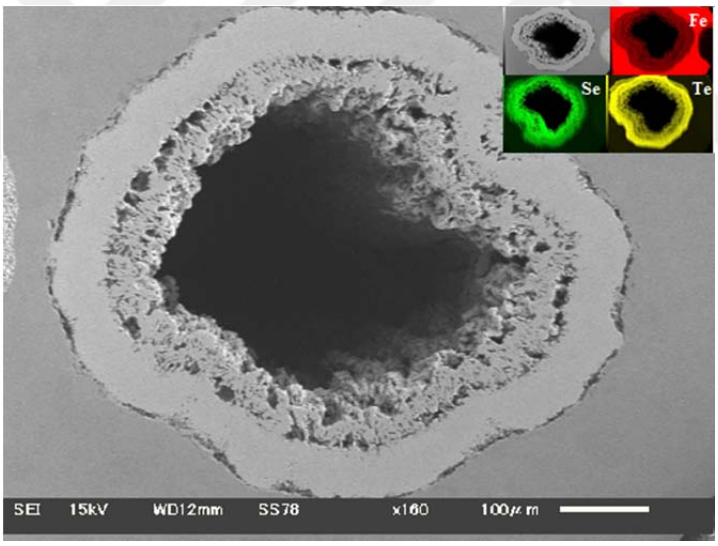

Figure 4.20. SEM image and EDX map images for the cross-section of Fe(Se,Te) wire 2

Figure 4.21. displays the resistivity versus temperature for the Fe(Se,Te) wire 2. In this figure, a steep drop in resistivity is observed the onset superconducting temperature at ~16.5 and ~4.5 K, respectively. The first

superconducting transition temperature is close to the bulk polycrystal $FeTe_{0.5}Se_{0.5}$ (Li et al., 2013), however the second one is below the $FeSe_{0.82}$ (Pomjakushina et al., 2009). In the Fe(Se,Te) wire 2, zero resistivity is not observed due to the excess Fe. As confirmed by EDX map and point analysis Fe sheath introduces much excess iron and accompany by evaporation of chalcogenides in the Fe(Se,Te) phase, which degrade the superconductivity.

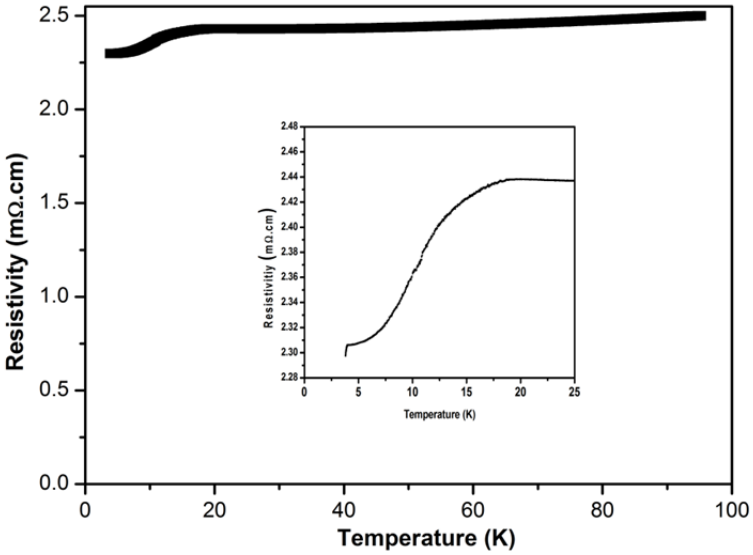

Figure 4.21. Resistivity versus temperature for Fe(Se,Te) wire 2 up to 100 K at zero-field

4.5. Results of the $Fe(Se_{0.7}Te_{0.3})_{1.5}$ Wire

The obtained $Fe(Se_{0.7}Te_{0.3})_{1.5}$ wires were annealed at different conditions (in Table 3.2), and then each wire's physical properties were investigated.

4.5.1. $Fe(Se_{0.7}Te_{0.3})_{1.5}$ wire 1

The results from the Rietveld refinement of the $Fe(Se_{0.7}Te_{0.3})_{1.5}$ wire 1 is plotted in figure 4.22. It shows that the $Fe(Se_{0.7}Te_{0.3})_{1.5}$ decomposes to two phases: Se-rich phase and Te-rich phase. Se-rich phase crystallizes in the tetragonal

structure (*P4/nmm*), and the composition is calculated as $Fe_{0.97}Se_{0.91}Te_{0.09}$ from refined composition phase. The lattice parameters are a,b = 3.7742 Å and c = 5.6061 Å. Te-rich phase is the tetragonal structure (*P4/nmm*) with composition $Fe_{1.05}Se_{0.05}Te_{0.95}$ and lattice parameters are a,b = 3.7887 Å and c = 5.9362 Å.

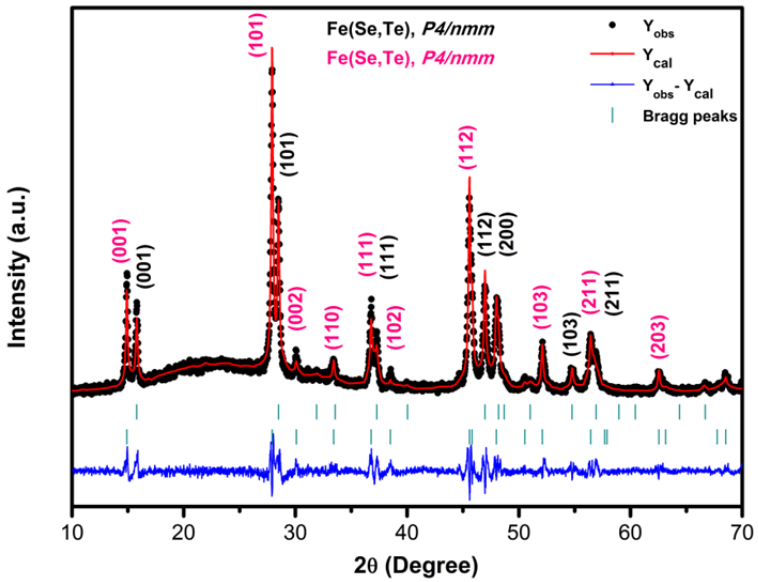

Figure 4.22. XRD pattern (black), Rietveld fit (red) and the differences between observed and calculated (blue) of $Fe(Se_{0.7}Te_{0.3})_{1.5}$ wire 1. The rows of ticks exhibit the Bragg-peak positions for Se-rich phase (black) and the Te-rich phase (pink).

Table 4.5. Atomic position of Se-rich phase $Fe_{0.97}Se_{0.91}Te_{0.09}$ (*P4/nmm*) and Te-rich phase $Fe_{1.05}Se_{0.05}Te_{0.95}$ (*P4/nmm*) (R_{exp}: 7.40, R_{wp}: 9.1; R_{exp}: 8.57 R_{wp}: 10.7).

Atom	Site	x	y	z	Occupation
Se-rich phase *P4/nmm* (41 %)					
Fe(1)	2a	¾	¼	0	0.80205
Fe(2)	2c	¼	¼	0.72591	0.02297
Se	2c	¼	¼	0.24578	0.77517
Te	2c	¼	¼	0.28681	0.07584
Te-rich phase *P4/nmm* (59 %)					
Fe(1)	2a	¾	¼	0	0.62871
Se	2c	¼	¼	0.24049	0.02748
Te	2c	¼	¼	0.26718	0.56613

SEM-BSE image and EDX map images for the cross-section of the $Fe(Se_xTe_{1-x})_{1.5}$ wire 1 displays in fig. 4.23. It shows that the distribution of Fe is almost uniformly throughout to the reacted layer the expection for little round Fe-spots. The Se-rich and the Te-rich region is distributed dark and the white phases, respectively. However, the dark phase and the white phase are difficult to separated due to its inter-granular arrangement; morever, due to the light coalescence, it can be mistaken with Fe-spots. So, the EDX analysis reveals stochiometry of $Fe(Se_xTe_{1-x})_{1.5}$ wire 1 as approximately $FeSe_{0.7}Te_{0.3}$. The SEM-EDX and XRD results confirm that there is no excess iron although the seath supplied the iron in the reacted layer.

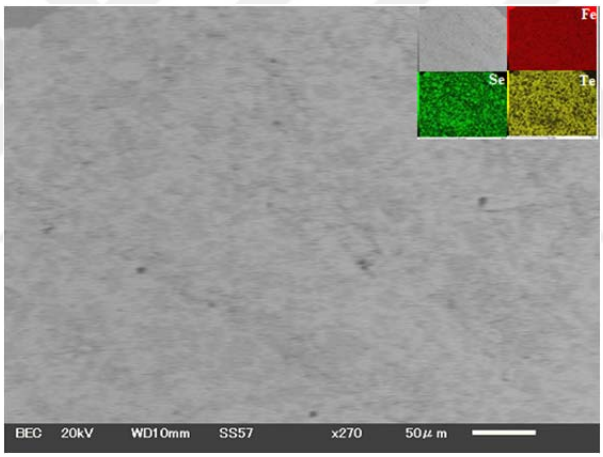

Figure 4.23. SEM image and EDX map images for the cross-section of the $Fe(Se_{0.7}Te_{0.3})_{1.5}$ wire 1

Figure 4.24 displays resistivity versus temperature under magnetic fields up to 3 T range of 2–15 K, inset; ρ–T curve from 300 K down to 2 K at 0 T for the $Fe(Se_{0.7}Te_{0.3})_{1.5}$ wire 1. The superconducting transition temperatures are defined as: the onset superconducting transition temperature T_c^{onset}, which is obtained from 90% of the normal state resistivity ρ_n (**H**, T), the mid-point temperature T_c^{mid}, which is found from 50% of ρ_n (**H**, T), and the zero-resistivity temperature T_c^{offset}, which is

obtained from 10% of ρ_n (**H**, T) from ρ–T curve. The critical temperature is found to be T_c^{onset} = 7.9, T_c^{mid} = 7 and T_c^{offset} = 6.5 K. The character of the ρ–T curve exhibits a metallic behavior until superconductivity appears. Resistivity versus temperature range of 2–15 K under magnetic fields of 0, 0.1, 0.5, 1 and 3 T show that the T_c decreases with increasing magnetic fields up to 3 T. The transition width ΔT defined by the T_c^{onset} and T_c^{offset} points on $\rho(T)$ is lower than 2 K (see Table 4.6). In the literature, there are lots of papers are geared towards investigating the FeTe compound which has the tetragonal crystal structure the same as FeSe compound, but it does not show the superconductivity because FeTe exhibits antiferromagnetic ordering around 70 K. Superconductivity appears when tellerium is substituted for selenium in an $FeSe_{1-x}Te_x$ compound ($0.2 \leq x \leq 0.9$) (Fang et al., 2008; Yeh et al., 2008; Mizuguchi et al., 2010). Thus, we can say the superconductivity came from the Se-rich phase, in which a little Te-substituted FeSe layer in the $Fe_{0.97}Se_{0.91}Te_{0.09}$. So, its transition temperature is very close to the polycrstal FeSe.

Table 4.6. Transition temperatures of the $Fe(Se_{0.7}Te_{0.3})_{1.5}$ wire 1.

	T_c^{onset} (K)	T_c^{mid} (K)	T_c^{offset} (K)	ΔT_c (K)
0 T	7.9	7.0	6.5	1.4
0.1 T	7.8	6.5	6.3	1.5
0.5 T	7.4	6.5	6.0	1.4
1 T	7.2	5.9	5.6	1.6
3 T	6.2	4.7	4.1	2.1

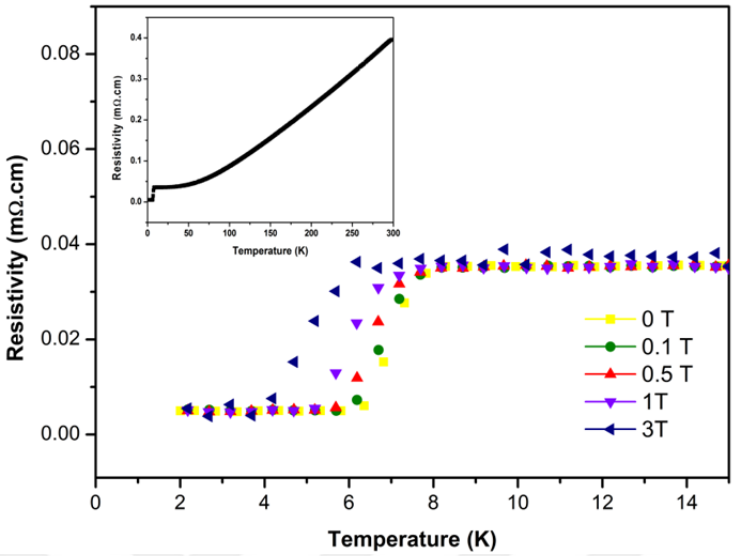

Figure 4.24. Zero field and in-field temperature dependences of electrical resistivity for $Fe(Se_{0.7}Te_{0.3})_{1.5}$ wire 1. Inset shows zero field resistivity curve, ρ(T), up to room temperatures for the $Fe(Se_{0.7}Te_{0.3})_{1.5}$ wire 1.

For magnetic field–temperature phase diagram, the irreversibility temperature T_i value is obtained from $d\rho/dT$ curve (in Figure 4.25), as shown in Figure 4.26. Using the criterion of 90% resistivity, we obtained the upper critical field $\mu_0 H_{c2}$ for the $Fe(Se_{0.7}Te_{0.3})_{1.5}$ wire 1. The phase diagram of the $\mu_0 H_{irr}$ and $\mu_0 H_{c2}$ are given in Figure 4.26. From the linear extrapolations of the $\mu_0 H_{irr}$ and $\mu_0 H_{c2}$, we estimated the value of the $\mu_0 H_{c2}$ (0 K) and the $\mu_0 H_{irr}$ (0 K) as 14.1 and 7.9 T, respectively. The $\mu_0 H_{c2}$ and the $\mu_0 H_{irr}$ can be estimated by the Werthamer–Helfand–Hohenberg (WHH) relation (Werthamer et al, 1966):

$$\mu_0 H_{c2}(T) = -0.693(dH_{c2}/dT_c)T_c \qquad (4.2)$$

where the slope $dH_{c2}/dT_c = -1.72$ T K^{-1} for $\mu_0 H_{c2}$ and $dH_{c2}/dT_C = -1.28$ T K^{-1} for $\mu_0 H_{irr}$. For T_c = 7.8 K, $\mu_0 H_{c2}$ was found to be 9.3 T, and for T_c= 6.5 K, $\mu_0 H_{irr}$ was calculated as 5.8 T. On the other hand, the $\mu_0 H_{irr}$ and $\mu_0 H_{c2}$ curves exhibit an

upturn curvature near 0 T. Such curvature was also observed in $Fe_{1+d}Se_xTe_{1-x}$ crystals and ascribed to include excess iron which might beget disorder into the system, bring about Te/Se vacancies in crystal structure. This kind of vacancies may give rise to an inhomogeneity in the compound (Ge et al., 2010). Morever, Pauli limiting field was calculated by using $\boldsymbol{\mu_0 H_p}(T) = 1.86T_c$ formula. Its value calculated as 14.5 T.

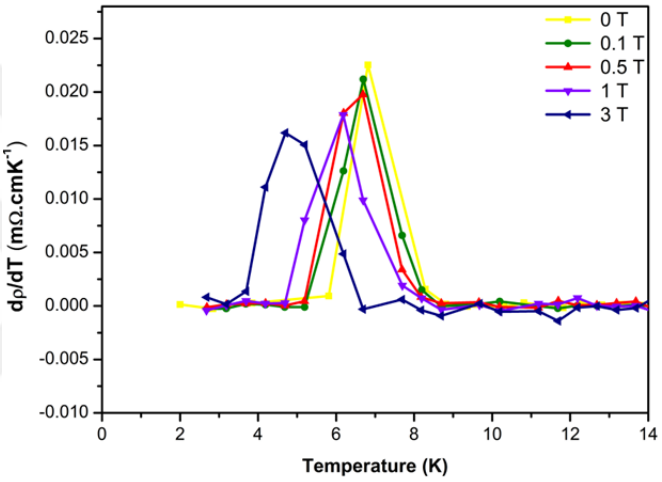

Figure 4.25. *dρ/dT* versus temperature for $Fe(Se_{0.7}Te_{0.3})_{1.5}$ wire 1.

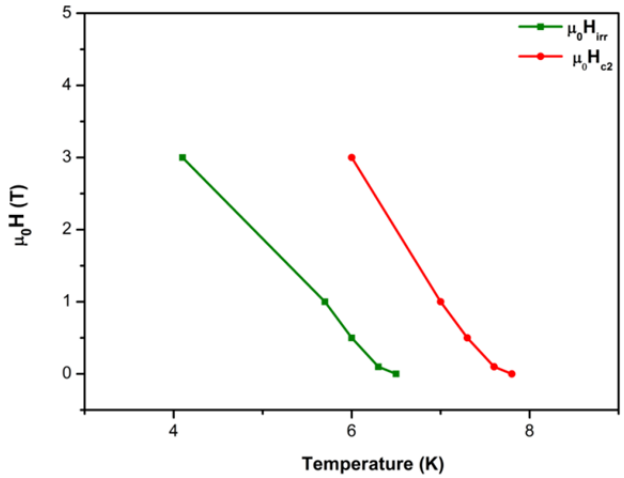

Figure 4.26. Magnetic field temperature phase diagram for the $Fe(Se_{0.7}Te_{0.3})_{1.5}$ wire 1.

The resistive superconducting transition in $Fe(Se_{0.7}Te_{0.3})_{1.5}$ wire 1 is strongly influenced by its flux dynamic. As shown in fig. 4.25, the T_c width increases and shifts to lower temperature with increasing applied magnetic field by reason of the thermally activated flux flow (TAFF) behaviour where the vortex bundles hop between neighboring pinning centers. As stated by the TAFF theory, the thermally activated resistivity in this region can be defined with the Arrhenius equation (Lei et al., 2012);

$$\rho(T, \mathbf{H}) = \rho_0 \exp\left[-\frac{U_0(T,\mathbf{H})}{k_B T}\right] \quad (4.3)$$

where ρ_0 is a prefactor, U_0 (T, **H**) is the activation energy of the flux flow of the vortex motion which depends on the temperature and the applied magnetic fields, and k_B is the Boltzmann constant. The activation energy at different magnetic fields can be calculated from slopes of the straight lines, as shown in fig. 4.27 (upper). From figure of U_0/k_B, the vortices may be firmly pinned and each vortex is independent at low applied magnetic fields (up to 0.5 T), whereas the vortices move collectedly, thus the value U_0(T, **H**) dissipate at high magnetic field, up to 3 T.

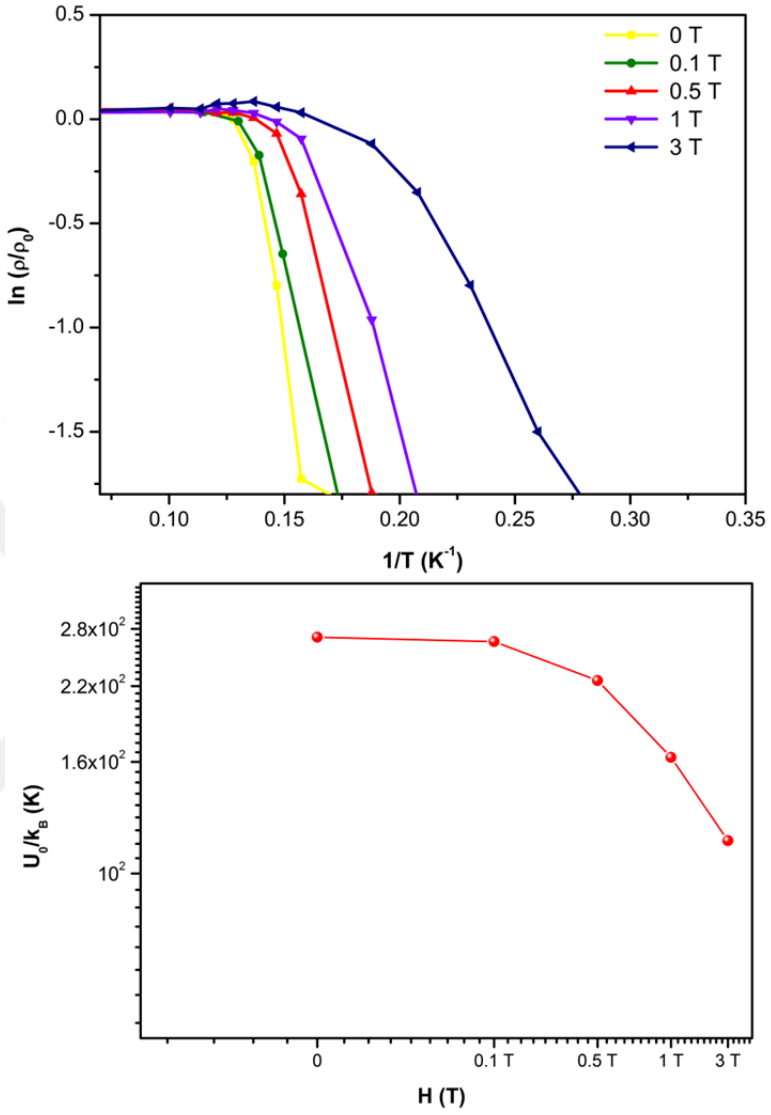

Figure 4.27. Upper**:** In (ρ/ρ_0) versus 1/T; bottom: U_0/k_B versus magnetic field.

4.5.2. $Fe(Se_{0.7}Te_{0.3})_{1.5}$ Wire 2

The results from the Rietveld refinement of the $Fe(Se_{0.7}Te_{0.3})_{1.5}$ wire 2 is plotted in Fig. 4.28. It shows that the $Fe(Se_{0.7}Se_{0.3})_{1.5}$ decomposes into two main phase; tetragonal FeSe (PbO structure, *P4/nmm*) and lattice parameters a,b = 3.7755 Å, c = 5.5794 Å and tetragonal FeTe (*P4/nmm*) and lattice paramaters a,b =

3.7883 Å c = 5.9501 Å with a small impurity peak identified as hexagonal FeTe (*P6₃/nmm*). The lattice paramaters of the FeSe phase are nearly the same as the bulk one (McQueen et al., 2009), while the lattice parameters of the FeTe are smaller than the bulk one (Sales et al., 2009; Fang et al.,2008), it might be the composition of Fe/Te lower than 1.

SEM-BSE image and EDX map images for the cross-section of the $Fe(Se_{1-x}Te_x)_{1.5}$ wire 2 displays in fig. 4.29. SEM images demonstrate the decomposition of $Fe(Se_{0.7}Te_{0.3})_{1.5}$ into FeSe and FeTe phases. EDX map analysis and point spectra show that dark parts belong to Se-rich, while the bright part belongs to Te-rich phases. The Fe is distributed almost homogeneously in the reacted layer. Also, the SEM-BSE image demonstrates that there are some cracks and voids in the whole scanning region. The SEM-EDX and XRD results confirm that there is no excess iron in the reaction layer due to the formation of the hexagonal FeTe in the reacted layer.

Figure 4.30 displays resistance versus temperature from 300 down to 2 K at 0 T (upper) and under magnetic fields up to 9 T ranging 2-15 K (bottom) for the $Fe(Se_{0.7}Te_{0.3})_{1.5}$ wire 2, respectively. The resistance started to decrease at 8 K and the zero-resistance observed at 7 K at 0 T. Meanwhile, the character of the *R–T* curve of the $Fe(Se_{0.7}Te_{0.3})_{1.5}$ wire 2 demonstrates a metallic behavior until the superconducting transition is arrived at. According to the temperature dependences of magnetoresistance (MR), the transition shifts to lower temperatures accompanied by a increase in the transition width with increasing magnetic field. The negative magnetoresistance term strengthens the superconducting phase.

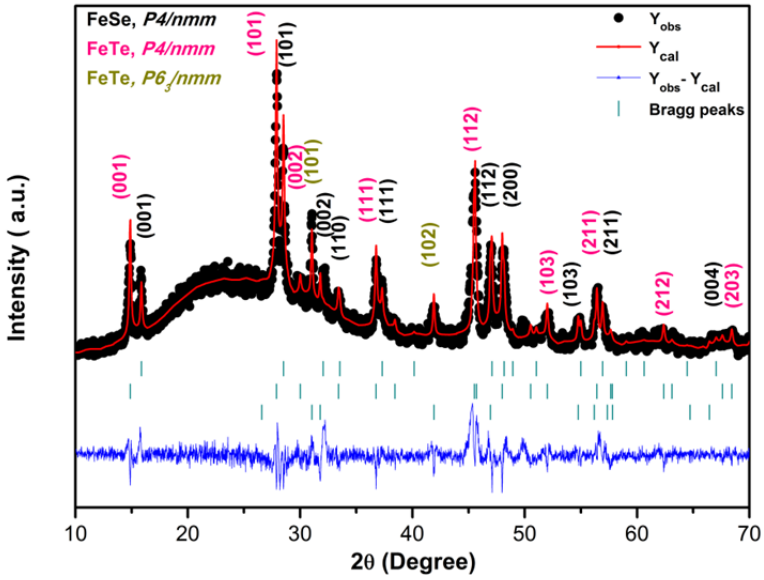

Figure 4.28. XRD pattern (black), Rietveld fit (red) and the differences between observed and calculated (blue) of $Fe(Se_{0.7}Te_{0.3})_{1.5}$ wire 2. The rows of ticks show the Bragg peak positions for the first phase (*P4/nmm*), the second phase (*P4/nmm*) and the third phase ($P6_3/nmm$).

For magnetic field–temperature phase diagram, the irreversibility temperature T_i value is obtained from $d\rho/dT$ curve (in Figure 4.30), as shown in fig. 4.32. For the upper critical field, $\mu_0 H_{c2}$, determined from the criterion of 90% resistive transition curve. The phase diagram of the $\mu_0 H_{irr}$ and $\mu_0 H_{c2}$ are shown in fig. 4.32. We estimated that the $\mu_0 H_{c2}$ (0 K) and the $\mu_0 H_{irr}$ (0 K) are 17.4 and 11.3 T from the linear extrapolations. By using the Werthamer–Helfand–Hohenberg (WHH) theory, the value of $\mu_0 H_{c2}$ and $\mu_0 H_{irr}$ at T = 0 K are 12.3 and 9.3 T, respectively. The $\mu_0 H_{c2}(T)$ and $\mu_0 H_{irr}(T)$ curves display an upturn curvature near 0 T due to the multi phase. Above 0.5 T, both $\mu_0 H_{c2}(T)$ and $\mu_0 H_{irr}(T)$ lines show a linear curve. On the other hand, the value $\mu_0 H_P(T)$ is 14.3 T.

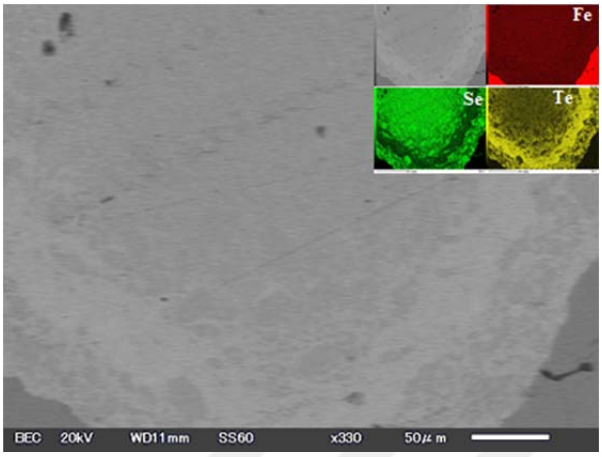

Figure 4.29. SEM image and EDX map images for the cross-section of the $Fe(Se_{0.7}Te_{0.3})_{1.5}$ wire 2.

Table 4.7. Transition temperature of the $Fe(Se_{0.7}Te_{0.3})_{1.5}$ wire of 2

	T_c^{onset} (K)	T_c^{mid} (K)	T_c^{offset} (K)	ΔT_c (K)
0 T	8	7.2	6.8	1.2
0.1 T	7.9	7.07	6.7	1.2
0.5 T	7.6	6.7	6.2	1.4
1 T	7.1	6.1	5.6	1.5
3 T	6.5	5.01	4.6	1.9
5 T	5.5	5.4	4.01	1.4
7 T	4.7	3.8	3.1	1.6
9 T	4.04	3.1	2.3	2.1

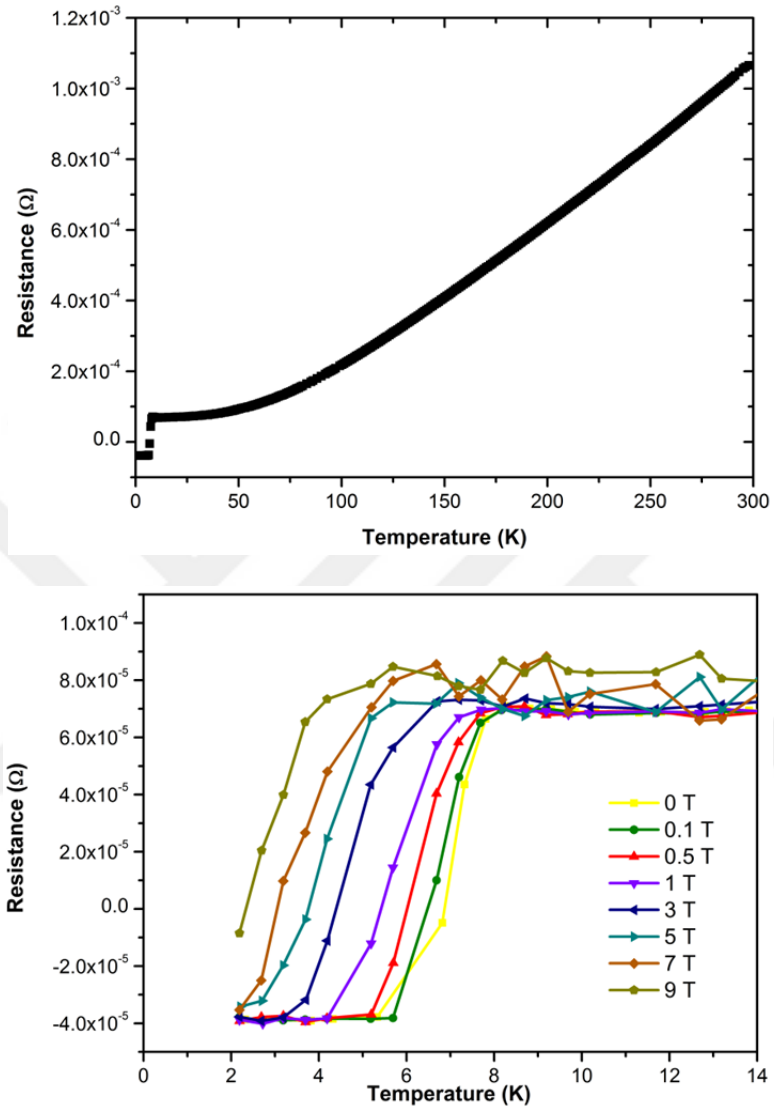

Figure 4.30. Upper: Resistance versus temperature for $Fe(Se_{0.7}Te_{0.3})_{1.5}$ wire 2 up to room temperature; bottom: Resistance versus temperature ranging between 2-15 K under different magnetic fields.

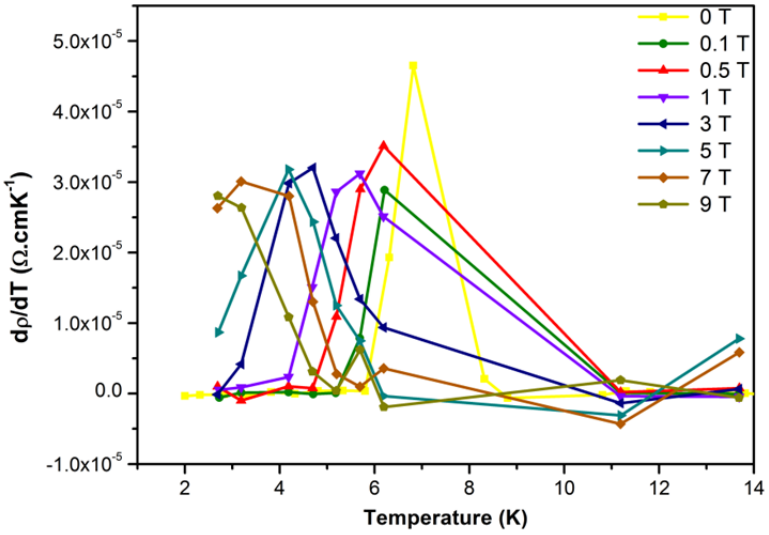

Figure 4.31. *dρ/dT* versus temperature for the $Fe(Se_{0.7}Te_{0.3})_{1.5}$ wire of 2.

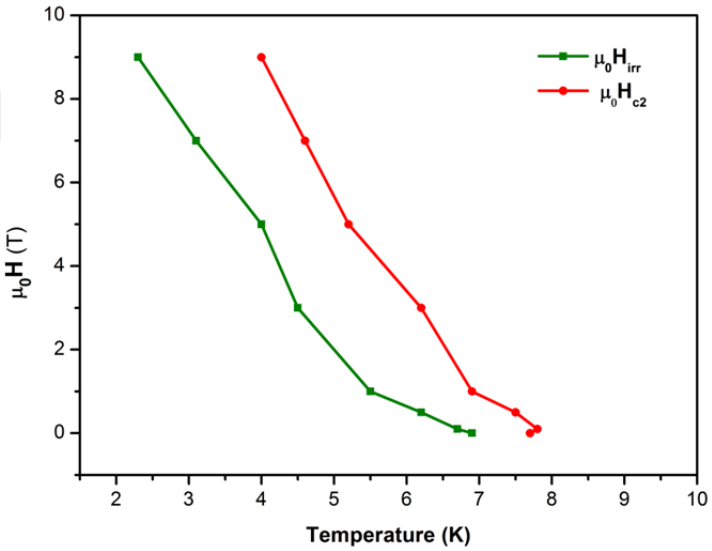

Figure 4.32. Magnetic field–temperature phase diagram for the $Fe(Se_{0.7}Te_{0.3})_{1.5}$ wire 2.

With increasing magnetic fields, the superconducting transition temperatures decrease and are accompained by broadening gradually, it might be weaker inter granular coupling or vortices motion, as shown in fig. 4.31. To investigate flux dynamic of $Fe(Se_{0.7}Te_{0.3})_{1.5}$ wire 2, the equation 4.2 was used and

$\ln(\rho/\rho_0)$ versus $1/T$ graph obtained for calculating of U_0/k_B (in Figure 4.33). Unexpectedly, despite the relatively low T_c, the U_0/k_B reaches approximately 10^3 K at low magnetic field, indicating that the strong pinning dominates up to 3 T, morever, U_0 shows weakly dependence of field at low magnetic field, agreement with literature (Lei et al., 2010; Ge et al., 2010). However, in high magnetic field up to 9 T, the U_0/k_B becomes mightily dependent on field, in which the vortices move collectedly.

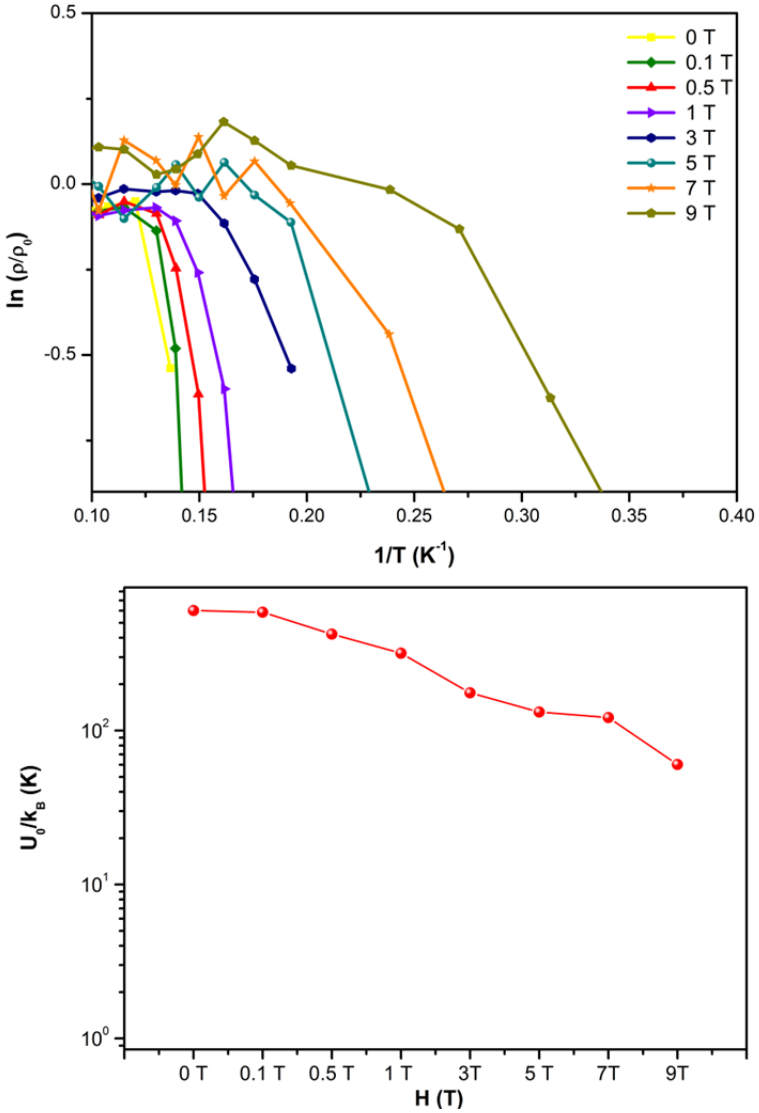

Figure 4.33. Upper: In(ρ/ρ_0) versus 1/T; bottom: U_0/k_B versus magnetic field.

4.6. Results of the Ag Doped $FeSe_{0.94}$ Wire

The obtained the Ag doped $FeSe_{0.94}$ wires were annealed at different conditions (in Table 3.3), and then each wire's physical properties were investigated.

4.6.1. Ag doped $FeSe_{0.94}$ Wire 1

The fitting result of the Ag doped $FeSe_{0.94}$ wire 1 is shown in figure 4.34. The XRD pattern of the wire indicates that it is mainly composed of the tetragonal $FeSe_{0.94}$ (*P4/nmm*) phase with the lattice parameters a = 3.7660 Å, c = 5.5103 Å and the hexagonal Fe_7Se_8 ($P3_1$) as a secondary phase with the lattice parameters a = 7.1585 Å, c = 17.2429 Å. The obtained lattice parameters of main phase are nearly same as the pure $FeSe_{0.94}$, suggesting that Ag may be not incorporated in the unit cell (Nazarova et al., 2015). In the literature, there are a few studies to investigate of Ag doped $FeSe_{1-x}$ and $FeSe_xTe_{1-x}$ crystals. The Ag addition $FeSe_{1-x}$ crystal was studied by Nazarova et al. (2015), who found the quantity of Ag_2Se (about 1%) and traces of Ag, according to the addition amount of Ag for FeSe crystal. In the case of $FeSe_{1-x}Te_x$ crystal, the Ag was found to occupy into the unit cell of $FeSe_xTe_{1-x}$ (Migita et al., 2013).

SEM image and EDX map images for the cross-section of the Ag doped $FeSe_{0.94}$ wire 1 is displayed in fig 4.35. It indicates that the distribution of Fe and Se are almost uniform throughout the reacted layer except for little round Fe-spots. The Ag is distributed inhomogeneously. From EDX mapping and point analysis, we found that the Ag content ranging from 0 wt % up to 90 wt. This confirms that the Ag is not reacted with Se which has the high reactive element as well is not incorporated into the unit cell.

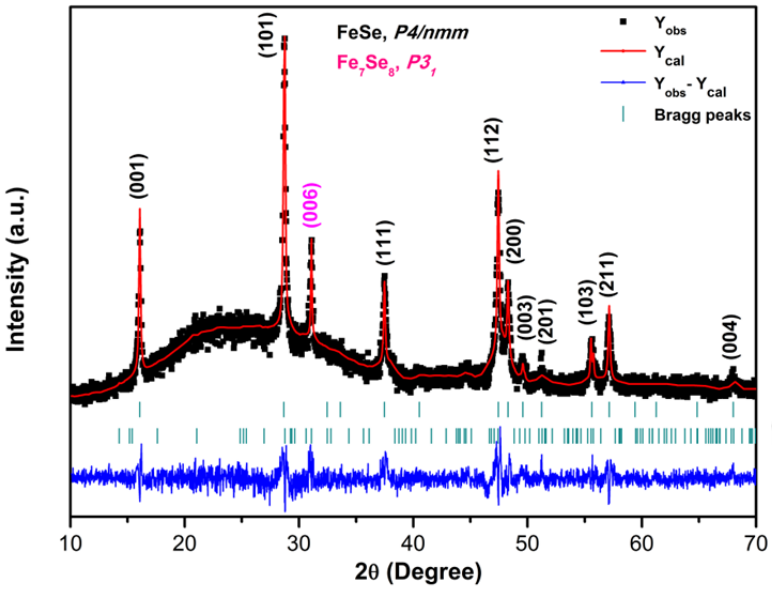

Figure 4.34. XRD pattern (black), Rietveld fit (red) and the differences between observed and calculated (blue) of Ag doping $FeSe_{0.94}$ wire 1. The rows of ticks display the Bragg-peak positions for the main phase (*P4/nmm*), the secondary phase ($P3_1$).

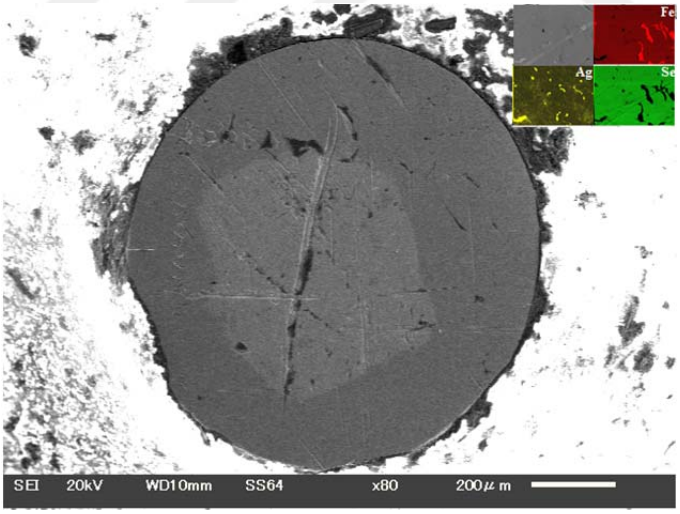

Figure 4.35. SEM image and EDX map images for the cross-section of the Ag doped $FeSe_{0.94}$ wire 1.

Figure 4.36 displays resistivity versus temperature from 300 down to 4 K under at 0 T. The character of the ρ-T curve of the Ag doped $FeSe_{0.94}$ wire 1 demonstrates a metallic behavior until the superconducting transition is arrived at. The curvature of $\rho(T)$ occurs below 100 K due to structural and magnetic transitions. This kind of abnormality in the resistivity curve obtained in the literature for Si, Sb and Ag doping in FeSe polycrystal, FeSe poly- and FeSe single crystal (Zhang et al., 2009; Lei et al., 2011; Sudesh et al., 2013; Nazarova et al., 2015). When the temperature was reached at about 9 K, the resistivity of the wire 1 has an sudden drop due to the appearance of superconductivity. The T_c^{onset} and T_c^{offset} are found to be 8.87 and 8.01 K, respectively. The width of superconducting transition (ΔT) is found as 0.86 K indicates good quality of the wire we obtained. This is a remarkable result, since it is the first time Ag doped $FeSe_{0.94}$ superconducting wire has been fabricated in the family of 11 wire.

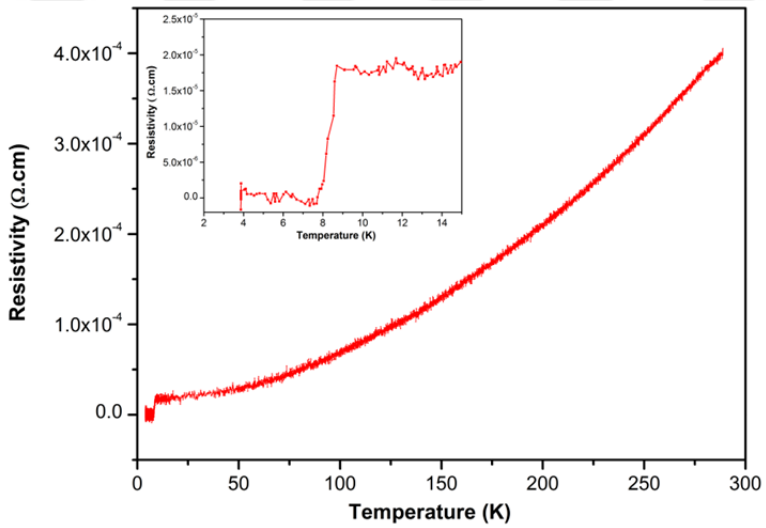

Figure 4.36. The temperature dependences of electrical resistivity for the Ag doped $FeSe_{0.94}$ wire 1. Inset shows an enlarged scale near the superconducting transition.

4.6.2. Ag Doped $FeSe_{0.94}$ Wire 2

The fitting result of the Ag doped $FeSe_{0.94}$ wire 2 is displayed in figure 4.37. XRD results show that the main phase is FeSe (*P4/nmm*) with lattice parameters a = 3.7685 Å and c = 5.5143 Å and the secondary phase is Fe_7Se_8 ($P3_1$) with lattice parameter a = 7.1682 Å and c = 17.2876 Å. The lattice parameters of the main phase sightly expand followed by rapid quenching.

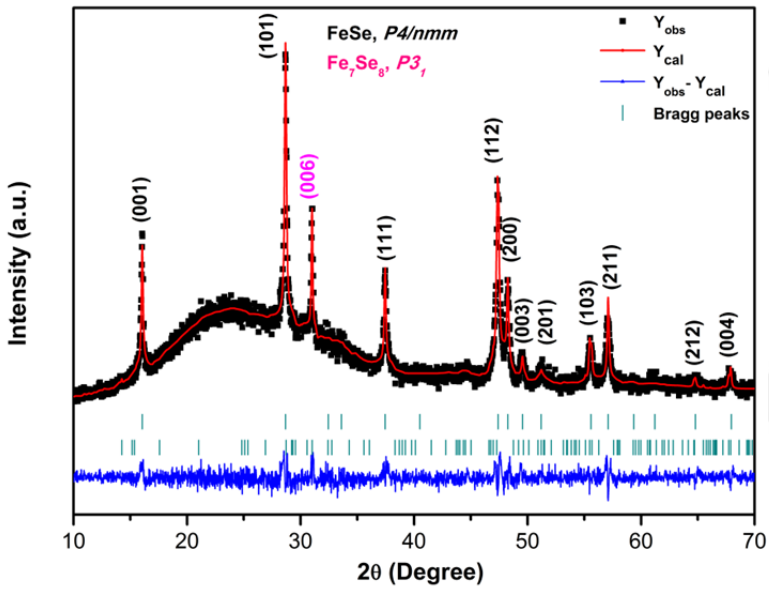

Figure 4.37. XRD pattern (black), Rietveld fit (red) and the differences between observed and calculated (blue) of Ag doping $FeSe_{0.94}$ wire 2. The rows of ticks show the Bragg-peak positions for the main phase (*P4/nmm*), the secondary phase ($P3_1$).

SEM image and EDX map images for the cross-section of the Ag doped $FeSe_{0.94}$ wire 2 shows in fig. 4.38. EDX map analysis and point spectra indicate that Fe and Se are distributed almost homogeneously with a few Fe-spots, but white parts belong to Ag-rich in the reacted layer.

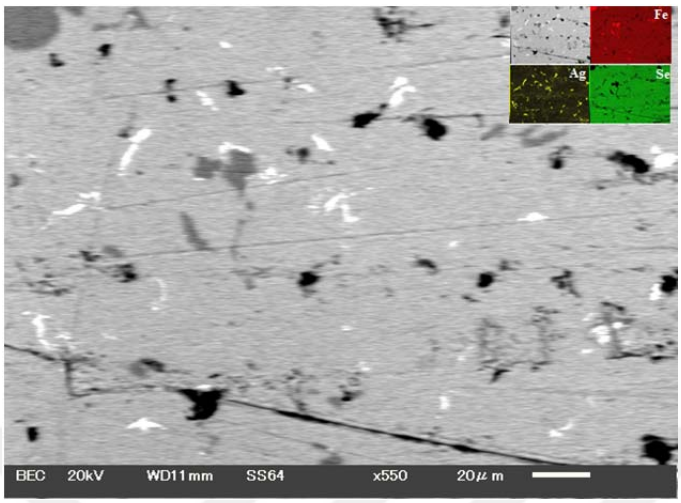

Figure 4.38. SEM image and EDX map images for the cross-section of the Ag doped $FeSe_{0.94}$ wire 2.

Figure 4.39 displays resistivity versus temperature from 300 down to 4 K under a zero magnetic field. The T_c^{onset} and T_c^{offset} are found to be 8 and 5.7 K, respectively.

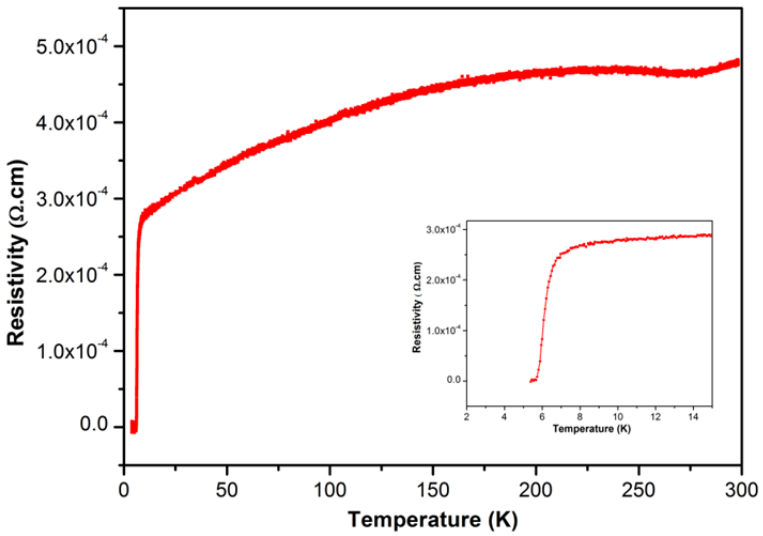

Figure 4.39. Resistivity versus temperature ranging between 4–300K for the Ag doped $FeSe_{0.94}$ wire 2. Inset shows an enlarged scale near the superconducting transition.

5. CONCLUSIONS AND FUTURE WORK

5.1. Conclusions

The purpose of this thesis is to try to improve iron chalcogen materials, which are expected to have applications in future technology. We prepared Fe(Se,Te) crystal and wire by using different processes in order to enable and/or improve the superconducting properties.

Synthesis and characterization of $FeSe_{0.5}Te_{0.5}$ single crystals prepared by self-flux technique with two different cooling rates of 1.45°C/h and 5.83°C/h have been investigated. According to XRD results, the both samples have tetragonal structure and the different cooling rate does not change the crystal stucture. The SEM results display that the both samples demonstrate a terrace-like formation. ZFC magnetization measurements show a very sharp transition which suggest the crystals are homogeneous. The superconducting transition temperatures of samples obtained from magnetization measurement are estimated to be 14.62 K for the rapid and 14.38 K for the slow cooling samples. Although the superconducting transition was almost the same temperature for both samples, the superconducting properties were rather different. The lower critical magnetic fields at 5 K, $\mathbf{H_{c1}}$, of rapid and slow cooling samples are estimated as 287 and 209 Oe, respectively. The value of J_c calculated from **M-H** curves for the rapid cooling sample is enhanced about 3 times compared to the slow cooling sample. The normalized pinning force f ($\mathbf{F_p/F_{pmax}}$) at h ($\mathbf{H/H_{irr}}$) curves are scaled using the Dew-Hughes model given by $f(h) = Ah^p(1-h)^q$ with A = 2.73, p = 0.81 and q = 0.69, the ratio $[p / p+q] \approx 0.54$ for cooling rate of 5.83°C/h sample. The obtained flux pinning results have presented that a strong δT_c–pinning plays a major role in the flux pinning mechanism.

$Fe_{1+d}Se_{0.4}Te_{0.6}$ (d = 0, 5, 10 %) polycrystals have been synthesized by using solid state metod, in order to investigate the effect of sulfur annealed in the various amount of excess iron. The XRD pattern of the as-grown samples show that it is mainly composed of the tetragonal PbO type (*P4/nmm*) phase with a minor

hexagonal NiAs type (*P31*) secondary phase. The as-grown crystals begin to decrease superconducting transition temperature and are accompained by superconducting volume fraction by increasing the amount of iron. After sulfur annealed, the XRD results show that the S-annealed samples have PbO-type phase, with hexagonal structure of FeS. After the S-annealed, samples remarkably increase of the superconducting transition temperature. The diamagnetic signal is strongly enhanced and superconducting transition temperature reach up to 14.5 K for incerasing the amount of iron and superconducting volume fraction is estimated as large as 45, 60 and 62 % in $Fe_{1+d}Se_{0.4}Te_{0.6}$ d = 0, 5, 10 %, respectively. The improvement in superconductivity has been attributed to the removal of excess Fe, which is inevitably incorporated in the as-grown crystals, by the annealing.

Synthesis and characterization of Ag doped $FeSe_{0.94}$ polycrystals prepared by melting have been investigated for the as-grown and the annealed. We obtained nearly single phase from the X-ray diffraction for both samples. Superconductivity occurs at temperatures below ~ 8 and 9.2 K for the as-grown and the annealed polycrystal, respectively. It confirms that the Ag doped and annealing increase good superconducting intergrain connections.

Fe(Te,Se) superconducting wires were produced by using *in-situ* and *ex-situ* PIT process. The Fe(Te,Se) wires using *in-situ* PIT process that the average composition of Se and/or Te different from the initial composition due to diffusion of them throughout the iron sheath, and the excess of iron can come from the sheath itself, in which it is strongly magnetic that interact with the adjacent Fe layers, acting as a pair breaker, thus degrade the superconductivity (Zhang et al., 2009; Liu et al., 2009). The improvement in superconductivity has been attributed to the removal of excess Fe, which is inevitably incorporated in the using an Fe tube, because the tube employed is made of Fe, it serves as both sheath and raw material for the fabrication of Fe(Se,Te) superconductor wire. To prevent the phase unbalancing characterized by the Se/Te deficient or the excess Fe, our starting precursor composition was Fe : Se,Te = 1 : 1.5. We have successfully fabricated

$Fe(Se_{0.7}Te_{0.3})_{1.5}$ superconducting wires using *ex-situ* PIT process. Then, wires were subjected to annealing at two different temperatures and time. XRD shows that the $Fe(Se_{0.7}Te_{0.3})_{1.5}$ wires decompose into two main phase; Se-rich phase and Te-rich phase. The Se-rich phase crystallizes in the tetragonal structure with space group *P4/nmm* and the Te-rich phase is the tetragonal structure with space group *P4/nmm* for wire 1, and for wire 2; tetragonal FeSe (*P4/nmm*) and tetragonal FeTe (*P4/nmm*) obtained with an small impurity peaks are identified as hexagonal FeTe ($P6_3/nmm$). The superconducting transition is appeared at about 8 K under self-field for both wires. We estimated the value of the $\mu_0 H_{c2}$ (0 K) and the $\mu_0 H_{irr}$ (0 K) as 14.1 and 7.9 T for the $Fe(Se_{0.7}Te_{0.3})_{1.5}$ wire 1, the $\mu_0 H_{c2}$ (0 K) and the $\mu_0 H_{irr}$ (0 K) are 17.4 and 11.3 T for the $Fe(Se_{0.7}Te_{0.3})_{1.5}$ wire 2, respectively.

The Ag-doped $FeSe_{0.94}$ superconducting wires were fabricated by using the ex-situ PIT method. The Ag is used as a chemical additive to improve the grain connection of the superconducting wires. From the X-ray diffraction, the reflection peaks have a well-indexed tetragonal structure with space group of *P4/nmm* with a very small amount of Ag impurity is also observed. The superconducting transition temperature is observed at about 8.87 K and resistivity completely disappeared at about 8.01 K for wire 1; 8 and 5.7 K for wire 2, respectively. This is a remarkable result, since it is the first time that the effect of Ag doping on the 11 family superconducting wire has been investigated.

5.2. Future work

A variety of techniques and approaches has been developed in this study and demonstrated to improve the superconducting properties of Fe(Se,Te), including the annealing, silver addition, different starting composition (for produce wire) *etc*. These attempts have increased to varying degrees the success rate of the growth of Fe(Se,Te) compounds, and at the same time have yielded enhanced superconducting properties. It is therefore necessary to consider the integrated impact of these different approaches on the Fe(Se,Te) system given that the

optimization of each may differ and be influenced by any other (for example, the amount of the optimal silver addition may change).

For future work, to investigate the role of the Ag doped on the crystal and/or wire is still not clear, because there is a few studies in the litareture. And also, we can focus on using different element for annealing such as Se, Te and O and the effect of doping in the 11 family such as Sn, Pb, Si for fabrication of crystal and wire.

BIBLIOGRAPHY

Alexandrov, A.S., 2003. Theory of Superconductivity From Weak to Strong Coupling. Institute of Physics Publishing, Bristol and Philadelphia, 314.

Asomba, G.C., Abah, O., Ogbuu, O. A., and Okoye, C. M., 2015. Analysis of the superconductivity in perovskite oxides using three-square-well BCS formalism. Pramana – J. Phys., 85: 1233–1244.

Błachowski, A., Ruebenbauer, K., Zukrowski, J., Przewoznik, J., Wojciechowski, K., Stadnikd, Z.M., 2010. Mössbauer spectroscopy evidence for the lack of iron magnetic moment in superconducting FeSe. Journal of Alloys and Compounds, 494 : 1–4.

Bray, J. W., 2009. Superconductors in Applications; Some Practical Aspects. EEE Transactions on Applied Superconductivity, 19(3) : 2533-2539.

Canfield, P. C., Finnemore, D. K., Bud'ko, S. L., Ostenson, J. E., Lapertot, G., Cunningham, C. E., and Petrovic, C., 2001. Superconductivity in Dense MgB2 Wires. PhysRevLett., 86 : 2423.

Chaddah, P., 2003. Critical current densities in superconducting materials. Sadhana, 28 : 273-282.

Chang, C.C., Chen, T.K., Lee, W.C., Lin, P.H., Wang, M.J., Wen, Y.C., Wue, P.M., Wu, M.K., 2014. Superconductivity in Fe-chalcogenides. Physica C, 514 : 423-434.

Chen, G. F., Li, Z., Wu, D., Li,G., Hu, W. Z., Dong, J., Zheng, P., Luo, J. L., and Wang, N. L., 2008. Superconductivity at 41 K and Its Competition with Spin-Density-Wave Instability in Layered CeO1-xFxFeAs. Phys Rev Lett, 100: 247002.

Choudhary, O. P., and Priyanka, 2017. Scanning Electron Microscope: Advantages and Disadvantages in Imaging Components. International Journal of Current Microbiology and Applied Sciences, 6(5):1877-1882.

Collett, B. M., 1970. Scanning Electron Microscopy: A Review and report of Research in Wood Science. J. Inst. Wood Sci., 2:113-133.

Cyrot, M., 1973. Ginzburg-Landau theory for superconductors. Rep. Prog. Phys. 36 103-158.

Dew-Hughes, D., 1974. Flux pinning mechanisms in type II superconductors. Phil. Mag., 30 : 293–305.

Dew-Hughes, D., 1975. Superconducting A-15 compounds: A review. Cryogenics, 15 : 435.

Dew-Hughes, D., 2001. The critical current of superconductors: an historical review. Low Temp. Phys., 27: 99-10.

Ding, Q. P., Mohan, S., Tsuchiya, Y., Taen, T., Nakajima, Y., and Tamegai, T., 2012. Magneto-optical imaging and transport properties of FeSe superconducting tapes prepared by the diffusion method. Supercond. Sci. Technol., 25 : 025003.

Dong, C. H., Wang, H. D., and Fang M. H., 2013. Exploration of iron-chalcogenide superconductors. Chin. Phys. B., 22 : 087401.

Echlin, P., Fiori, C.E., Goldstein, J., Joy, D.C., Newbury, D.E., 2013. Advanced scanning electron microscopy and X-ray microanalysis. Springer Science & Business Media, Berlin, Germany.

Editorial, 2015. Superconducting materials classes: Introduction and overview. Physica C, 514 : 1–8.

Epp, J., 2016. X-ray diffraction (XRD) techniques for materials characterization, Materials Characterization Using Nondestructive Evaluation (NDE) Methods.

Fang, M., Yang, J., Balakirev, F. F., Kohama, Y., Singleton, J., Qian, B., Mao, Z. Q., Wang, H., and Yuan1, H. Q., 2010. Weak anisotropy of the superconducting upper critical field in Fe1.11Te0.6Se0.4 single crystals. Phys. Rev. B, 81 : 020509(R).

Fujioka, M., Denholme, S. J., Ozaki, T., Okazaki, H., Deguchi, K., Demura, S., Hara, H., Watanabe, T., Takeya, H., Yamaguchi, T., Kumakura, H., and Takano, Y., 2013. Phase diagram and superconductivity at 58.1 K in α-FeAs-free SmFeAsO1-xFx. Supercond. Sci. Technol., 26 : 085023.

Galluzzi, A., Polichetti, M., Buchkov, K., Nazarova, E., Mancusi, D., and Pace, S., 2016. Critical current and flux dynamics in Ag doped FeSe superconductor. Supercond. Sci. Technol., 30 : 025013.

Gao, Z., Qi, Y., Wang, L., Wang, D., Zhang, X., Yao C., and Ma Y., 2011. Superconducting properties of FeSe wires and tapes prepared by a gas diffusion technique. Supercond. Sci. Technol., 24 : 065022.

Ge, J., Cao, S., Yuan, S., Kang, B., and Zhang, J., 2010. Three-dimensional superconductivity in nominal composition Fe1.03Se with Tc zero up to 10.9 K induced by internal strain. Journal of Applied Physics, 108 : 053903.

Guo, J., Jin, S., Wang, G., Wang, S., Zhu, K., Zhou, T., He, M., and Chen, X., 2010. Superconductivity in the iron selenide KxFe2Se2 ($0 \leq x \leq 1.0$). Physical Review B, 82: 180520.

Hosono, H., Tanabe, K., Muromachi, E. T., Kageyama, H., Yamanaka, S., Kumakura, H., Nohara, M.,, Hiramatsu, H., and Fujitsu, S., 2015. Exploration of new superconductors and functional materials, and fabrication of superconducting tapes and wires of iron pnictides. Sci. Technol. Adv. Mater., 16 : 033503.

Hosono, H., Yamamoto, A., Hiramatsu, H., Ma, Y., 2018. Recent advances in iron-based superconductors toward applications. Materials Today, 21 : 3.

Hsu, F.C., Luo, J. Y., Yeh, K. W., Chen, T.K., Huang, T.W., Wu, P.M., Lee, Y.C., Huang, Y. L., Chu, Y.C., Yan, D.C., Wu, M.K., 2008. Superconductivity in the PbO-type structure α–FeSe. PNAS, 15 : 14262–14264.

Ivanovskii, A. L., 2008. New high-temperature superconductors based on rare-earth and transition metal oxyarsenides and related phases : synthesis, properties, and simulations. Physics - Uspekhi, 51(12) : 1229-1260.

Izawa, H., Mizuguchi, Y., Takano, Y., Miura, O., 2014. Fabrication of FeTe0.4Se0.6 superconducting tapes by a chemical-transformation PIT process. Physica C, 504 : 77–80.

Johnston, D. C., 2010, The puzzle of high temperature superconductivity in layered iron pnictides and chalcogenides, Advances in Physics, 59 : 803–1061.

Kamihara, Y., Hiramatsu, Y., Hirano, M., Kawamura, R., Yanagi, H., Kamiya T., and Hosono, H., 2006. Iron-based layered superconductors: LaOFeP. J. AM. Chem. Soc., 126:10012-10013.

Kamihara, Y., Watanabe, T., Hirano M., and Hosono H., 2008. Iron-Based Layered Superconductor La[O1-xFx]FeAs (x= 0.05−0.12) with Tc= 26 K. Journal of the American Chemical Society, 130(11) : 3296-3297.

Kramer, E. J., 1973, Scaling laws for flux pinning in hard superconductors, J. Appl. Phys., 44 : 1360.

Kwok, W.K., Welp, U., Glatz, A., Koshelev, A.E., Kihlstrom, K.J., and Crabtree, G.W, 2016. Vortices in high-performance high-temperature superconductors. Rep. Prog. Phys., 79 : 116501.

Koshika, Y., Usui, T., Adachi, S., Watanabe, T., Sakano, K., Simayi, S., and Yoshizawa, M., 2013. Effects of Annealing under Tellurium Vapor for Fe1:03Te0:8Se0:2 Single Crystals. Journal of the Physical Society of Japan, 82 : 023703.

Lei, H., Hu, R., and Petrovic, C., 2011. Critical fields, thermally activated transport, and critical current density of β-FeSe single crystals. Phys. Rev. B., 84 : 014520.

Lei, H., Wang, K., Hu, R., Ryu, H., Abeykoon, M., Bozin, E. S., and Petrovic, C., 2012. Iron chalcogenide superconductors at high magnetic fields. Sci. Technol. Adv. Mater., 13 : 054305.

Lei, H., Hu, R., Choi, E. S., and Petrovic, C., 2010. Thermally activated energy and flux-flow Hall effect of Fe1+y(Te1+xSx)z. Phys. Rev. B., 82 : 134525.

Li, X., Gao, Z., Liu, Y., Mab, Z., Yu, L., Li, H., Yang, H., 2013. The microstructures and superconducting properties of FeSe0.5Te0.5 bulks with original milled powders. Cryogenics,57 : 50–54.

Li, S., Cruz, C., Huang, Q., Chen, Y., Lynn, J. W., Hu, J., Huang, Y. L., Hsu, F. C., Yeh, K. W., Wu, M. K., and Dai, P., 2009. First-order magnetic and structural phase transitions in Fe1+ySexTe1−x. Phys. Rev. B., 79 : 054503.

Liu, R. H., Wu, G., Wu, T., Fang, D. F., Chen, H., Li, S. Y., Liu, K., Xie, Y. L., Wang, X. F., Yang, R. L., Ding, L., He, C., Feng, D. L., and Chen, X. H., 2008. Anomalous Transport Properties and Phase Diagram of the FeAs-Based SmFeAsO1-xFx Superconductors. Phys Rev Lett 101: 087001.

Liu, T. J., Ke, X., Qian, B., Hu, J., Fobes, D., Vehstedt, E. K., Pham, H., Yang, J.H., Fang, M. H., Spinu, L., Schiffer, P., Liu, Y., and Mao, Z. Q., 2009. Charge-carrier localization induced by excess Fe in the superconductor Fe1+yTe1−xSex. Phys. Rev. B., 80 : 174509.

Ma, Y., 2012. Progress in wire fabrication of iron-based superconductors. Supercond. Sci. Technol., 25 : 113001.

Ma, Y., Gao, Z., Qi, Y., Zhang, X., Wang, L., Zhang, Z., Wang D., 2009. Fabrication and characterization of iron pnictide wires and bulk materials through the powder-in-tube method. Physica C, 469 : 651–656.

Marouchkine, A., 2002. High-Temperature Superconductivity in Cuprates-The Nonlinear Mechanism and Tunneling Measurements. Kluwer Academic Publishers, New York, Boston, Dordrecht, London, Moscow, 336.

Marouchkine, A., 2004. Room-Temperature Superconductivity. Cambridge International Science Publishing, United Kingdom, 310.

McQueen, T. M., Huang, Q., Ksenofontov, V., Felser, C., Xu, Q., Zandbergen, H., S. Hor, Y., Allred, J., Williams, J. A., Qu, D., Checkelsky, J., Ong, N. P., and Cava, R. J., 2009. Extreme sensitivity of superconductivity to stoichiometry in Fe1+δSe. Phys. Rev. B., 79 : 014522.

Medvedev, S., McQueen, T. M., Troyan, I. A., Palasyuk, T., Eremets, M. I., Cava, R. J., Naghavi, S., Casper, F., Ksenofontov, V., Wortmann, G., and Felser, C., 2009. Electronic and magnetic phase diagram of β-Fe1.01Se with superconductivity at 36.7 K under pressure. Nature Materials, 8 : 630-633.

Meissner W., and Franz, H., 1930. Messungen mit Hilfe von flüssigen Helium. VIII. Supraleitfähigkeit von Niobium. Physikalisch-Technische Reichsanstalt, Mitteilung: 558-559.

Mendoza, D., Benitez, J. L., Morales, F., Escudero R., 2010. Magnetic anomaly in superconducting FeSe. Solid State Communications, 150 : 1124-1127.

Migita, M., Takikawa, Y., Sugai, K., Takeda, M., Uehara, M., Kuramoto, T., Takano, Y., Mizuguchi, Y., Kimishima, Y., 2013. Substitution effects of Ag into FeSe0.5Te0.5 superconductor. Physica C, 484 : 66–68.

Mitchell, E. J., Hillesheim, D. A., Bridges, A. C., Paranthaman, M. P., Gofryk, K., Rindfleisch, M., Tomsic, M., and Sefat, S. A., 2014. Optimization of a non-arsenic iron-based superconductor for wire fabrication. Supercond. Sci. Technol., 28 : 045018.

Mizuguchi, Y., Deguchi, K., Tsuda, S., Yamaguchi, T., Takeya, H., Kumakura, H., and Takano Y., 2009. Fabrication of the Iron-Based Superconducting Wire Using Fe(Se,Te). Applied Physics Express, 2: 083004–083006.

Mizuguchi, Y.,, Izawa, H.,, Ozaki, T., Takano, Y., and Miura O., 2011. Transport properties of single- and three-core FeSe wires fabricated by a novel chemical-transformation PIT process. Supercond. Sci. Technol., 24 : 125003.

Mizuguchi Y., and Takano, Y., 2010. Review of Fe Chalcogenides as the Simplest Fe-Based Superconductor. Journal of the Physical Society of Japan, 79 : 102001.

Nagamatsu, J., Nakagawa, N., Muranaka, T., Zenitani, Y., and Akimitsu, J., 2001. Superconductivity at 39 K in magnesium diboride. Nature, 410 : 63-64.

Nazarova, E., Balchev, N., Nenkov, K., Buchkov, K., Kovacheva, D., Zahariev, A., and Fuchs, G., 2015. Improvement of the superconducting properties of polycrystalline FeSe by silver addition. Supercond. Sci. Technol., 28 : 125013.

Nazarova, E., Buchkov, K., Terzieva, S., Nenkov, K., Zahariev, A., Kovacheva, D., Balchev, N., Fuchs, G., 2015. The Effect of Ag Addition on the Superconducting Properties of FeSe0.94. J Supercond Nov Magn, 28 : 1135–1138.

Ohno, M., Kawamata, T., Noji, T., Naruse, K., Matsuoka, Y., Adachi, T., Nishizaki, T., Sasaki, T., and Koike, Y., 2014. Thermal Conductivity and Annealing Effects in the Iron-Based Superconductor FeSe0.3Te0.7. Journal of the Physical Society of Japan, 83 : 044704.

Omar, M. A., 1993. Elementary Solid State Physics. Addison-Wesley Publishing Company, United States of Amirica, 669.

Ozaki, T., Deguchi, K., Mizuguchi,Y., Kumakura, H., and Takanon Y., 2011. Transport Properties of Iron-Based FeTe0.5Se0.5 Superconducting Wire. IEEE Trans. Appl. Supercond., 21 : 2858.

Ozaki, T., Deguchi, K., Mizuguchi, Y., Kawasaki, Y., Tanaka, T.,, Yamaguchi, T., Tsuda, S.,, Kumakura, H., and Takano, Y., 2011. Transport properties and microstructure of mono- and seven-core wires of FeSe1−xTex superconductor produced by the Fe-diffusion powder-in-tube method. Supercond. Sci. Technol., 24: 105002.

Ozaki, T., Deguchi, K., Mizuguchi, Y., Kawasaki, Y., Tanaka, T., Yamaguchi, T., Kumakura, H., and Takano, Y., 2012. Fabrication of binary FeSe superconducting wires by diffusion process. Journal of Applied Physics, 111 : 112620.

Palombo, M., Malagoli, A., Pani, M., Bernini, C., Manfrinetti, P., Palenzona, A., and Putti, M., 2015. Exploring the feasibility of Fe(Se,Te) conductors by ex-situ powder-in-tube method. Journal of Applied Physics, 117 : 213903.

Patel, U., Hua, J., Yu, H. S., Avci, S., Xiao, Z. L., Claus, H., Schlueter, J., Vlasko-Vlasov, V. V., Welp, U., and Kwok, W. K., 2009. Growth and superconductivity of FeSex crystals. Applied Physics Letters, 94 : 082508.

Physical Property Measurement System® DynaCoolTM User's Manual Part Number 1307-110, A0.

Physical Property Measurement System Thermal Transport Option User's Manual Part Number 1684-100B.

Pomjakushina, E., Conder, K., Pomjakushin, V., Bendele, M., and Khasanov, R., 2009. Synthesis, crystal structure, and chemical stability of the superconductor FeSe1−x. Phys. Rev. B., 80 : 024517.

Ren, Z.-A., Che, G. C., Dong, X. L., Yang, J., Lu, W., Yi, W., Shen, X. L., Li, Z. C., Sun, L. L., Zhou, F., Zhao, Z. X., 2008. Superconductivity and phase diagram in ironbased arsenic-oxides ReFeAsO1−δ (Re = rareearth metal) without fluorine doping. A Letters Journal Exploring the Frontier of Physics, 83 : 17002.

Roberts, B. W., 1976. Survey of superconductive materials and critical evaluation of selected properties. J. Phys. Chem. Ref. Data, 5: 581-821.

Rotter, M., Tegel, M., and Johrendt, D., 2008. Superconductivity at 38 K in the iron arsenide (Ba1-xKx)Fe2As2. Phys Rev Lett, 101:107006.

Sales, B. C., Sefat, A. S., McGuire, M. A., Jin, R. Y., and Mandrus, D., 2009. Bulk superconductivity at 14 K in single crystals of Fe1+yTexSe1−x. Phys. Rev. B., 79 : 094521.

Seidel, P., 2015. Applied Superconductivity Handbook on Devices and Applications. Sales, B. C., Sefat, A. S., McGuire, M. A., Jin, R. Y., and Mandrus, D., 2009. Bulk superconductivity at 14 K in single crystals of Fe1+yTexSe1−x. Phys. Rev. B., 79 : 094521.

Sexana, A., K., 2009. High Temperature Superconductors. Springer Series in Material Science, New York, 226.

Solyom, J., 2007. Fundamentals of the Physics of Solids Volume 1- Structure and Dynamics. Springer, Berlin Heidelberg, 695.

Stewart, G.R., 2015. Superconductivity in the A15 structure. Physica C, 514 : 28–35.

Sudesh, S. R., Varma, G.D., 2013. Effect of Sb and Si doping on the superconducting properties of FeSe0.9. Physica C, 485 : 137–144.

Sun, Y., Tsuchiya, Y., Yamada, T., Taen, T., Pyon, S., Shi, Z. X., Tamegai, T., 2014. Chalcogen (O2, S, Se, Te) atmosphere annealing induced bulk superconductivity in Fe1+yTe1-xSex single crystal. Physica C, 504 : 12–15.

Taen, T., Tsuchiya, Y., Nakajima, Y., and Tamegai, T., 2009. Superconductivity at Tc14 K in single-crystalline FeTe0.61Se0.39. Phys. Rev. B, 80 : 092502.

Takahashi, H., Igawa, K., Arii, K., Kamihara, Y., Hirano, M., Hosono, H., 2008. Superconductivity at 43 K in iron-nased layered compound LaO1-xFxFeAs. Nature Letters, 453 : 06972.

Tinkham, M., 1996. Introduction to Superconductivity. McGraw-Hill International Editions, Singapore, 454.

Tozman, P., 2016. Search for magnets with properties intermediate between Nd-Fe-Band Ferrite. Departement of Physics,University of Dublin, Ph-D thesis, 184.

Wang, C., Li, L., Chi, S., Zhu, Z., Ren, Z., Li, Y., Wang, Y., Lin, X., Luo, Y., Jiang, S., Xu, X., Cao, G., and Xu, Z., 2008. Thorium-doping–induced superconductivity up to 56 K in Gd1−xThxFeAsO. A Letters Journal Exploring the Frontier of Physics, 83: 67006.

Wang, X.C., Liu, Q. Q., Lv, Y.X., Gao, W. B., Yang, L.X., Yu, R.C., Li, F.Y., Jin, C. Q., 2008. The superconductivity at 18 K in LiFeAs system. Solid State Communications, 148 : 538-540.

Watanabe, T., Yanagi, H., Kamiya, T., Kamihara, Y., Hiramatsu, H., Hirano, M., and Hosono, H., 2007. Nickel-Based Oxyphosphide Superconductors with a Layered Crystal Structure, LaniOP. Inorganic Chemistry Comunication, 46: 7719-7721.

Werthamer, N. R., Helfand, K., and Hohenberg, P. C., 1966. Temperature and Purity Dependence of the Superconducting Critical Field, H_{c2}, III. Electron Spin and Spin-Orbit Effects. Phys. Rev., 147 : 295.

Williams, A.J., McQueen, T.M., Cava, R.J., 2009. The stoichiometry of FeSe. Solid State Communications, 149 : 1507-1509.

Wu, Z. F., Wang, Z. H., Tao, J., Qiu, L., Yang, S. G., and Wen, H. H., 2016. Flux pinning and relaxation in FeSe0.5Te0.5 single crystals. Supercond. Sci. Technol., 29 : 035006.

Wu, X. J., Zhang, Z. Z., Zhang, J. Y., Li, B. H., Ju, Z. G., Lu, Y. M., Li, B. S., and Shen, D. Z., 2008. Two-carrier transport and ferromagnetism in FeSe thin films. Journal of Applied Physics, 103 : 113501.

Xu, Z., Schneeloch, J. A., Yi, M., Zhao, Y., Matsuda, M., Pajerowski, D. M., Chi, S., Birgeneau, R. J., Gu, G., Tranquada, J. M., and Xu, G., 2018. Coexistence of superconductivity and short-range double-stripe spin correlations in Te-vapor annealed FeTe1−xSex (x =0.2). Phys. Rev. B., 97 : 214511.

Yadav, C. S., and Paulose, P. L., 2009. Upper critical field, lower critical field and critical current density of FeTe0.60Se0.40 single crystals. New Journal of Physics, 11 : 103046.

Yeh, K. W., Huang, T. W., Huang, Y. L., Chen, T. K., Hsu, F. C., Wu, P. M., Lee, Y. C., Chu, Y. Y., Chen, C. L., Luo, J. Y., Yan, D. C., and Wu, M. K., 2008. Tellurium substitution effect on superconductivity of the α-phase iron selenide. A Letters Journal Exploring the Frontier of Physics, 84: 37002.

Yeh, K. W., Ke, C. T., Huang, T. W., Chen, T. K., Huang, Y. L., Wu, P. M., and Wu, M. K., 2009. Superconducting FeSe1-xTex Single Crystals Grown by Optical Zone-Melting Technique. Crystal Grown Design, 9 : 4847-4851.

Zargar, R. A., Pal, A., Hafiz, A.K., Awana, V.P.S., 2014. Structural, Electrical and Magnetic Behaviour of FeTe0.5Se0.5 Superconductor. J Supercond. Nov. Magn., 27 : 897–901.

Zhang, S. B., Zhu, X. D., Lei1, H. C., Li, G., Wang, B. S., Li, L. J., Zhu, X. B., Yang, Z. R., Song, W. H., Dai, J. M., and Sun, Y. P, 2009. Superconductivity of FeSe0.89 crystal with hexagonal and tetragonal structures. Supercond. Sci. Technol., 22 : 075016.

www.commons.wikimedia.org 12.12.2018

www.es.slideshare.net 25.12.2018

http://ceeielche.emprenemjunts.es 07.12.2018

www.nptel.ac.in 27.11.2018

www.slideshare.net 05.12.2018

www.rigaku.com 01.01.2019

www.zmb.uzh.ch 05.01.2019

www.qd-latam.com 29.12.2018

CURRICULUM VITAE

Derya FARİSOĞULLARI graduated from B.S. in the Department of Physics from the Dicle University. After that, she started to MSc in the Department of Physics from the Dicle University. Following her MSc graduation, she started to PhD in the Department of Physics from Cukurova University. She joined Nano Frontier Superconducting Materials Group in the National Institute for Materials Science (NIMS) between 2017 and 2018 in Japan. Her research interests are investigation of microstructure, crystal, wire and physical properties of iron-based superconductors, superconducting and magnetic thin film, magnetic and microstructure characterization.